Synthesis and Characterization at the Atomic Scale of 2D Materials for Future Heterostructure Integration

---

A Thesis

Presented to the faculty of the
School of Engineering and Applied Science
University of Virginia

In partial fulfillment
of the requirements for the degree of

Master of Science

by

Anna Costine
December, 2020

Approval Sheet

The thesis is submitted in partial fulfillment of the requirements for the degree of

Master of Science

Anna Costine

Author

The thesis is submitted to be read and approved by the examining committee:

Petra Reinke

Advisor

Stephen McDonnell

Prasanna Venkata Balachandran

Contents

Abstract

Two-dimensional (2D) materials are of interest for a wide variety of electrical and optical applications, due to their intriguing optical, electronic, and mechanical properties. In particular, the stacking of single layer materials into a designer multilayer heterostructure is quite promising for electronic and optical devices. Device integration requires a fundamental understanding of the synthesis mechanisms, defect structure and stability of 2D materials. The work presented in this thesis investigates a diverse set of 2D materials which are of eminent technological relevance: Transition Metal Dichalcogenides (TMDs), silicene, and graphene. The investigations focused on gaining insight into synthesis mechanisms, electronically and geometrically characterizing surface reconstructions and defects, and thermal stability measurements.

The thermal stability of 2D WS_2 on a Au/Ti substrate was studied with XPS, which offers unique insight into the surface reactions of a technologically relevant materials system at different annealing temperatures. These results were obtained by annealing under ultrahigh vacuum in small temperature steps and determining the chemical nature of the surface after each step. The WS_2 itself is relatively stable until annealing temperatures (~600 ^{0}C) are reached, with no change other than doping due to sulfur loss. Ti, however, diffuses upwards to the surface causing a number of side reactions. This result suggests that Ti is too reactive to be used as the sticking agent for Au, in this materials system.

The synthesis studies of 2D MoS_2 have been explored at length, and yet, there has been much difficulty in repeatability of these synthesis techniques. This data-driven study explores the parameter space in which monolayer MoS_2 is synthesized, based on literature results from a wide

variety of research groups. The synthesis mechanism for 2D MoS_2 is studied by collecting literature data on synthesis conditions for monolayer and bilayer/ multilayer MoS_2 and analyzing the data with Machine Learning techniques. The synthesis parameters with the highest impact are the Mo precursor annealing temperature and the pressure of the reaction chamber.

Silicene, the 2D analogue of graphene, has been theoretically predicted to have intriguing electronic properties, but it is difficult to test these properties experimentally, due to difficulties synthesizing silicene that is electronically decoupled from the substrate. Here, silicene is synthesized via e-beam deposition of Mo onto Si, followed by annealing, and the characterized with STM/STS. A range of silicene-related reconstructions are observed at cryostatic temperatures with characteristic geometries, electronic properties and defect structures. The most notable being ribbon-silicene which has a similar lattice constant to silicene (~0.36 nm) and Dirac-type band edges. Structural models are suggested for future work in DFT calculations.

Acknowledgements

I have many people to thank at UVa and beyond, without whom this thesis would not have been possible. First, Prof. Petra Reinke, my advisor and mentor, who taught me and supported me very much during time at UVa. I would also like to thank my current and previous group members, Will Blades, Cameron Volders, and Nathaniel Kabat, for scientific assistance and discussions. I would also like to thank Prof. Stephen McDonnell and his group members, Peter Litwin and Gabby Abad, for their contributions to the silicene work presented in this thesis. Prof. Prasanna Venkata Balachandran also contributed to part of the work here with his expertise on statistical/ machine learning techniques.

I am also grateful for the assistance of Dr. Gai and her lab group members (past and present), Mingming Fu and George Ge, for their assistance in LTHB-STM measurements at ORNL and many silicene discussions. Additionally, I would like to thank our collaborators at NRL, Dr. Cory Cress and his group members Jose J. Fonseca and Jeremy T. Robinson, who provided us with WS_2 samples. All of these people were instrumental in furthering my research education and my actual research, which is presented here.

I would also like to acknowledge funding from the NSF, University of Virginia's Research Innovation Award, and the UVa-ORNL Travel Fund, without which this work would not have been possible.

List of Figures

List of Tables

Chapter 1: Introduction

Over 15 years ago, the isolation of graphene proved that 2D materials could be synthesized.[1–4] The unique electronic properties of graphene were found to be quite distinct from its 3D counterpart, inspiring a range of studies into other single or few-layer materials.[1–3] Many of the most promising materials are similar to graphene structurally (silicene, germanene, h-BN) or have a similar layered structure to graphite (TMDs).[5–7] The layered materials are especially interesting, as they show potential for 2D heterostructure devices (Figure 1.1).[8] The weak van der Waals interlayer bonding coupled with strong covalent intralayer bonding of layered materials has allowed researchers to separate and reassemble them into multilayer designer heterostructures.[6,8] Figure 1.1 demonstrates this concept by comparing it to the stacking of Legos. Heterostructures composed of stacked 2D materials have shown great potential for highly tunable 2D electronic and optical devices which benefit a range of fields of interest including: water splitting,[9] Hydrogen Evolution Reaction (HER),[10] p-n junctions,[11] enhanced degradation of organic pollutants,[12] chemical sensing,[13] and phototransisters.[14]

The potential for 2D heterostructure devices is limited by their stability, quality of interface, and defect structure.[8] The highly tunable 2D materials in question are also highly susceptible to inconsistent electronic behavior due to defects or residue left behind by the synthesis method. 2D materials are known to be more reactive than their 3D counterparts. Despite these issues, heterostructures of 2 or 3 different 2D materials are fairly frequently synthesized and studied by researchers.[10–12,14] However, more complex heterostuctures and scaling up these materials for potential applications still requires a greater understanding of the thermal stability, chemical stability, defect structure, synthesis processes, and quality of the interface. The fundamental properties of a variety of 2D materials are explored with surface sensitive methods such as X-ray Photoelectron Spectroscopy (XPS), Scanning Tunneling Microscopy/ Spectroscopy (STM/STS), and Machine Learning (ML).

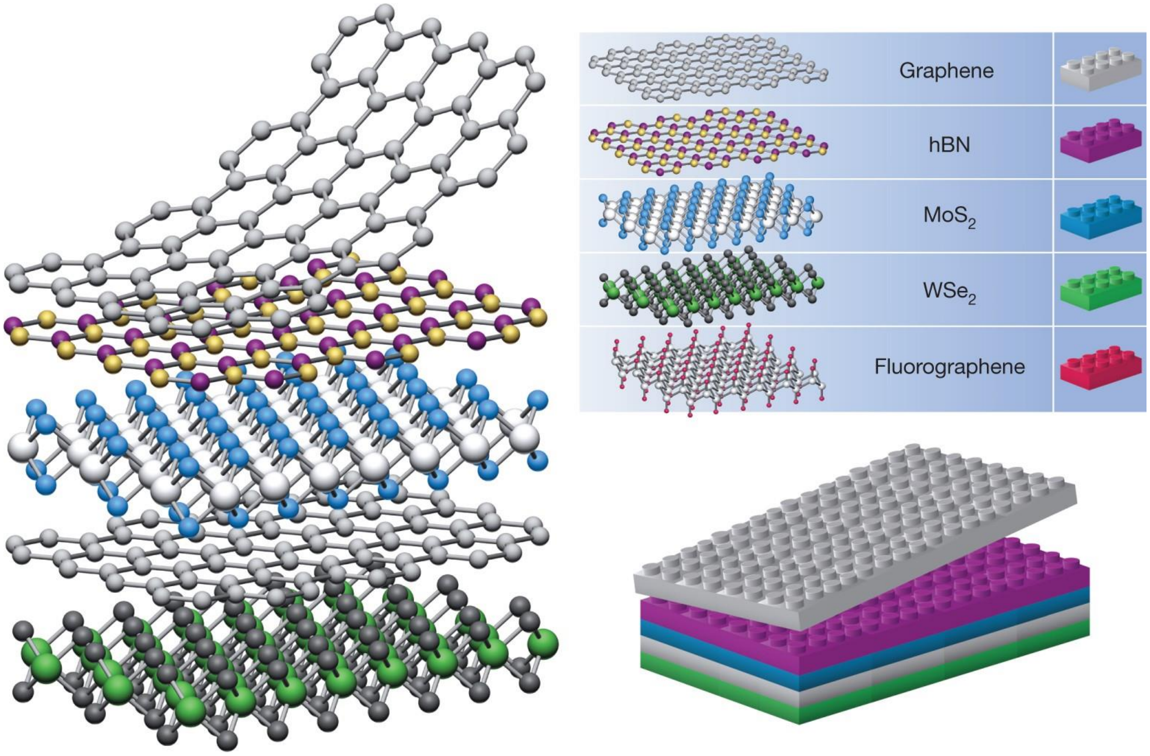

Figure 1.1: A designer multilayer heterostructures composed of single layer materials stacked together, reminiscent of the stacking of legos.[8]

In the work presented here, the synthesis of monolayer MoS_2 is explored through the creation of a dataset composed of MoS_2 synthesis studies from literature. Data-driven methods (provided by the Balachandran Group) employ this dataset to determine the parameter space for monolayer MoS_2 synthesis. MoS_2 is explored because of the high number of synthesis publications available, and there is widespread interest in MoS_2 for a range of optical electronic applications, because of its direct bandgap on the visible light spectrum,[15,16] as well as various catalytic applications.[10,15]. A detailed understanding of synthesis conditions and mechanisms are necessary if 2D materials are to be synthesized on top of each other, as the reactivity of the system becomes much more complex for heterostructure growth. Heterostructure device integration of MoS_2 and other 2D materials benefits from knowledge of the exact parameter space in which they can be synthesized. Machine learning methods have been instrumental in solving materials science problems for a range of material systems.[17,18] This data-driven approach seeks to find common ground among synthesis methods, and shed light on potential synthesis mechanisms.

Another 2D material studied in this thesis is silicene. Silicene has been theoretically predicted to have a range of intriguing properties including: Dirac nature, strong spin-orbit interaction, quantum phases and a geometric and electronic structure that is tunable by the application of an electronic field.[5,19,20] Silicene is also expected to be more compatible with existing silicon technology than most other 2D materials. Synthesis of silicene is difficult, especially on technologically relevant substrates that preserve silicene's intriguing properties, which has limited experimental studies. Greater understanding and control of silicene synthesis would aid its incorporation into devices, including multilayer heterostructure devices. Here, the synthesis of silicene is explored on a semiconducting silicide (h-$MoSi_2$) to limit hybridization between the silicene and substrate, which is common in silicene/metal systems. h-$MoSi_2$ also has close lattice matching with silicene, which promotes the formation of low-buckled silicene. The low-buckled geometry is more technologically relevant as it retains a more Dirac-type electronic structure, and is electronically and geometrically similar to graphene, but offers a small band gap and larger spin-orbit coupling which extends its use to quantum materials.[21,22] The synthesis of silicene in this thesis is accomplished via e-beam deposition of Mo onto a Si substrate, followed by annealing and formation of silicide, which serves as a silicene template. A range of Mo deposition amounts and annealing temperatures are investigated, and the resultant structures are electronically and geometrically characterized with STM/STS. The most intriguing of the structures is a ribbon-like honeycomb pattern with Dirac-type band edges.

Knowledge of the thermal stability of 2D materials will aid heterostructure synthesis by giving researchers a range of compatible temperatures for synthesizing a given 2D layer. WS_2 shows potential for incorporation into heterostructure devices due to its bandgap on the visible light spectrum, high catalytic activity, and gas sensing abilities.[23–25] In the work presented here, the thermal stability of WS_2 on a Au/Ti substrate is characterized by stepwise annealing with the chemical information captured via XPS after each step. This method allows us to determine the reactions that occur and the onset temperatures of these reactions which will help define the parameter space for their incorporation into heterostructure devices.

Additional studies were pursued in the last few years, but are not included in the present thesis. These include geometric and electronic characterization of 2D WSe_2/graphite and a Graphene/2D GaN/SiC at the atomic scale. The defect structure of 2D WSe_2 is explored because its intriguing properties (high optical quality, high performance as a FET, and high ambipolar device behavior)[26–29] make it a promising material for incorporation into heterostructure devices. A complete understanding of the defect structure of the 2D material building blocks will aid the synthesis of heterostructures. 2D WSe_2 (synthesized via Molecular Beam Epitaxy (MBE) in the McDonnell Group) was investigated at cryostatic temperatures with STM/STS, resulting in the electronic and geometric characterization of numerous types of p-type and n-type point defects. Analysis of these results is ongoing.

The Gr/2D GaN/SiC study investigated the nucleation mechanism for Ga intercalation between graphene and SiC for a more controlled synthesis. The heterostructure in question allowed for the first experimental realization of 2D GaN which shows potential as a large bandgap semiconductor similar to h-BN.[30] Gr/GaN/SiC is formed by intercalating Ga under the graphene layer and then treating it with ammonia gas to form 2D GaN, which is otherwise unstable as a 2D material.[30] The Gr/GaN/SiC samples were synthesized by the Redwing Group at Penn State, and they hypothesized that the Ga intercalation was facilitated by defects in the graphene layer induced by plasma treatment. The nucleation mechanism is explored in this work by characterization of the defects on Graphene with STM/STS before and after deposition of Ga. The results show that a number of vacancies and divacancies are present before Ga deposition, and these defects appear to be passivated after Ga deposition. However, the amount of Ga on the surface was quite significant, making it difficult to identify which defect sites were favored. Further studies will explore the graphene surface with less Ga deposited to determine a more precise nucleation and intercalation mechanisms.

Chapter 2: Materials

2.1 Two-Dimensional Transition Metal Dichalcogenides (2D TMDs)

Two-dimensional transition metal dichalcogenides (TMDs) are defined as being MX_2 semiconductors where M is a transition metal (Mo, W, Zr etc..) and X is a chalcogenide (S, Se, or Te).[31] They are layered materials with weak interlayer van der Waals bonds, and strong intralayer covalent bonds, and can therefore be exfoliated from bulk crystals.[6,31] The intralayer geometry consists of a layer of transition metal sandwiched between two layers of chalcogenide. For the materials discussed here, these layers are hexagonal, as shown in Figure 2.1.[31] Other phases with the same MX_2 stoichiometry are possible, but these phases have very different electronic properties.[6,31]

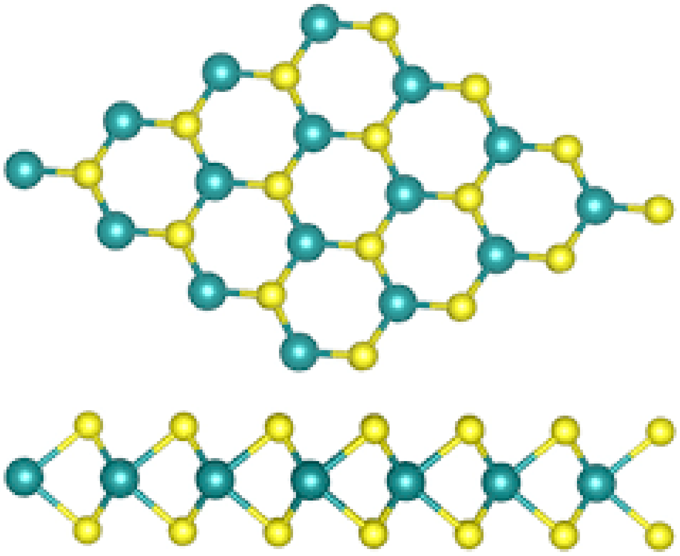

Figure 2.1: Geomtric structure of 2D MX_2 semiconductors, the top view (above) and side view (below) are shown.[31]

The TMD family of materials has been the subject of research for a range of potential applications due to their intriguing properties and relative ease of synthesis. The optical and electronic properties of 2D TMDs are promising because many of them have bandgaps within the visual light range (1.6-2.7 eV), as shown in Figure 2.2.[16,32] The bandgaps can even be tuned by altering the number of layers of TMD. MoS_2, the first discovered and most frequently studied TMD, has also been shown to retain favorable electronic properties when mechanically stretched.[16,33] MoS_2, WS_2, and WS_2 have direct bandgaps on the visible light spectrum, as shown in Figure 2.2, making them particularly interesting for optical applications.

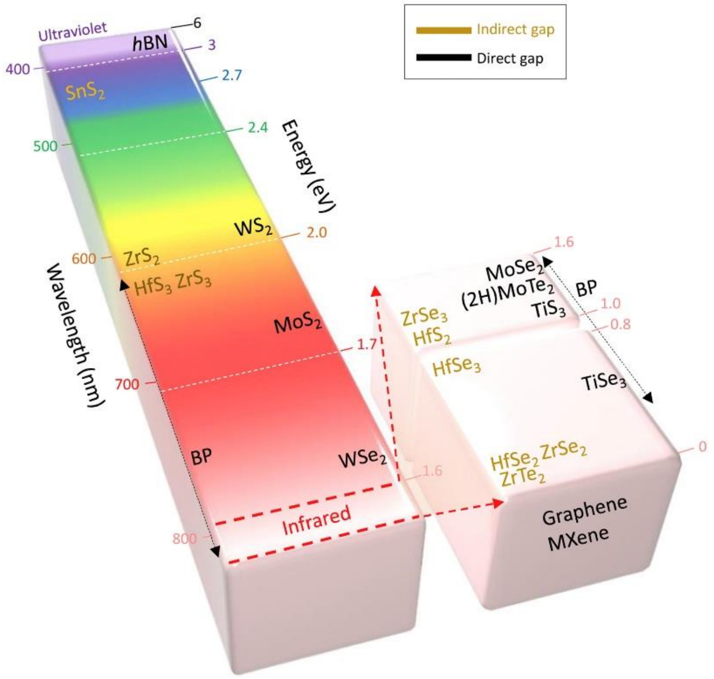

Figure 2.2: The range of 2D TMDs in terms of type of bandgap (direct/indirect) and size of bandgap. The wavelength of light emitted for each material's bandgap is shown visually and numerically.[32]

The favorable electronic and optical properties of 2D TMDs can be altered by the density and type of defects and on the interaction between the TMD and the substrate.[14,34] Therefore, much research has been dedicated to TMD synthesis on different substrates and the characterization of defects. The work presented in this thesis explores the stability of TMDs and characterization of their defects on different substrates.

2.1.1 Monolayer Tungsten Disulfide/ Gold-Titanium (WS_2/Au-Ti)

Tungsten disulfide is one of the more commonly studied TMDs due to its direct bandgap in the visible light spectrum.[32] Monolayer WS_2 can be mechanically exfoliated from the bulk using the scotch tape method, allowing for ease of synthesis on a variety of substrates. The resultant structure has hexagonal geometry, as illustrated in Figure 2.1. There are two primary applications of interest for WS_2/ Au. The first is water-splitting, as the Hydrogen Evolution Reaction (HER) has been shown to occur at much higher rates for WS_2 and MoS_2 on Au substrates.[35] Au is also commonly used as an electrode in WS_2 based transistors.[24,36] In both cases, Ti is frequently used as a sticking agent to adhere a thin layer of flat Au to a cheaper substrate (thereby reducing costs).

In the present work, the sample studied is a WS_2 monolayer mechanically exfoliated onto a 30 nm thick layer of Au adhered to a SiO_2/Si substrate with a 5 nm thick Ti sticking layer. The synthesis was performed by the Cress group at the Naval Research Lab (NRL).

2.1.2 Two-Dimensional Tungsten Diselenide/ Highly Oriented Pyrolytic Graphite (2D WSe_2/HOPG)

Tungsten Diselenide (WSe_2) is a 2D TMD with the hexagonal geometry described in Figure 2.1. This material is particularly interesting not just because of its direct bandgap on the visible light spectrum, but also because of its large spin-orbit coupling, ambipolar electrostatic behavior, and high optical quality.[26–28] The WSe_2 sample characterized in this work was synthesized with Molecular Beam Epitaxy (MBE). The synthesis was performed at UVa by the

McDonnell group. The WSe_2 layer is composed of triangular sheets that almost all monolayer and bilayer, with very few trilayer regions. The regions are in registry with the underlying HOPG substrate. The HOPG substrate was mechanically cleaved in air to reveal an atomically flat surface structure.[37] This material was chosen as the substrate because of the van der Waals epitaxy at the WSe_2 and HOPG interface and because HOPG is conductive enough to be STM compatible.

2.2 Silicene and Graphene

The synthesis of 2D freestanding graphene in 2004 sparked interest in a wide variety of 2D materials with intriguing electronic properties.[1,2] Graphene has a zero bandgap due to the Dirac nature of its band structure, resulting in massless electrons.[38] These distinct charge carriers give it high mobility.[22,38] It is especially promising for heterostucture devices due to its van der Waals interplane bonding which promote ease of incorporation.[39] The structure of graphene is honeycomb and atomically flat, as shown in Figure 2.3.[22]

Another promising 2D material is the silicon analog to graphene: silicene. This material is structurally and electronically similar to graphene, but with a few key differences due to atomic scale buckling in the z-direction, as shown in Figure 2.3.[22,40] This buckling ranges in degree and has a massive effect on the electronic properties of the silicene. Low-buckling is of particular interest as this is the conformation that retains the Dirac-nature of graphene.[5,40] Tunable buckling is also of interest as this would allow for bandgap tuning, which has been shown theoretically to occur with the application of an electric field.[5] Silicene has also been shown theoretically to have several quantum phases and larger spin-orbit coupling than graphene.[41]

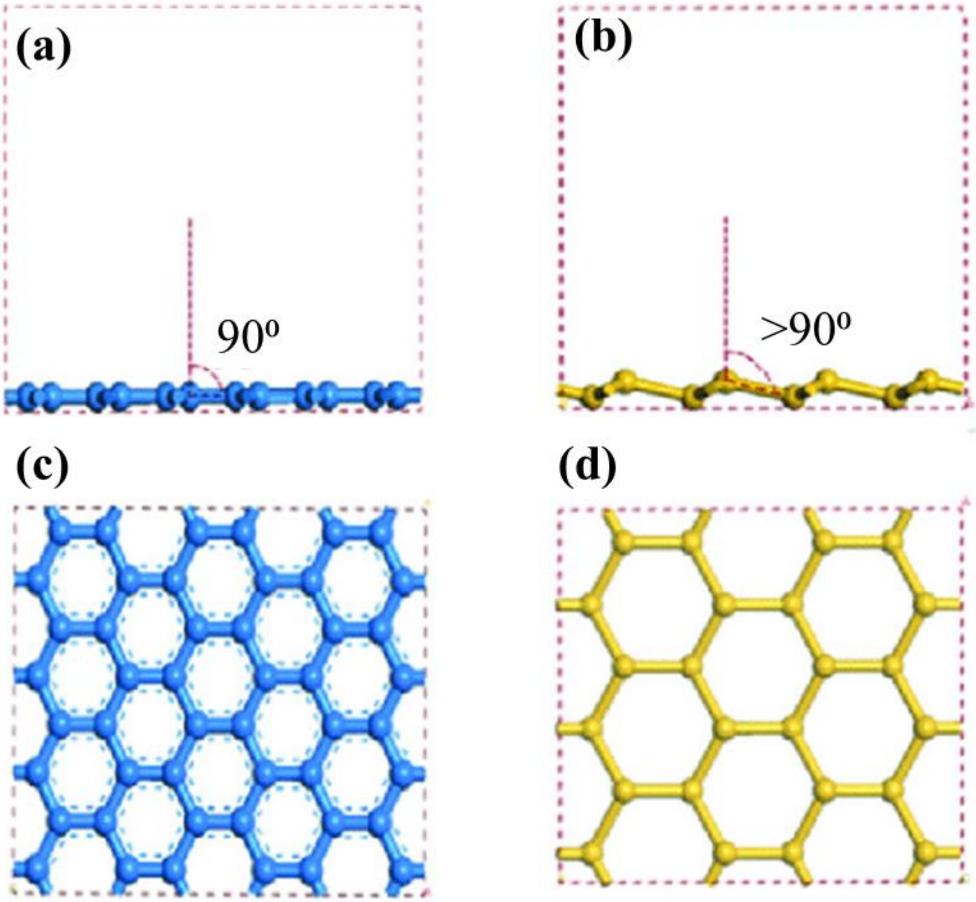

Figure 2.3: The geometric arrangements of the side-views of (a) graphene and (b) and the top-views of (c) graphene and (d) silicene.[42]

Unfortunately, most of the work to date on silicene has been theoretical due to experimental difficulties synthesizing silicene. These difficulties are particularly notable with technologically relevant substrates. The substrate in question has a strong effect on the buckling and electronic properties of silicene because silicene requires substrate support (cannot be free-standing). The intriguing properties promised by theoreticians could be unlocked with a greater understanding of how different substrates effect the electronic properties of silicene.

2.2.1 Si(100) and (111), and MoSi$_2$

One candidate for silicene growth in the low-buckled conformation, which retains Dirac-type nature, is the family of semiconducting silicides. In particular, semiconducting silicides in the hexagonal phase that would have a small amount of lattice strain with silicene. The materials meeting these requirements for lattice matching are chromium disilicide and molybdenum disilicide.[43] This work focuses on the silicene phases found on hexagonal molybdenum disilicide (h-MoSi$_2$).

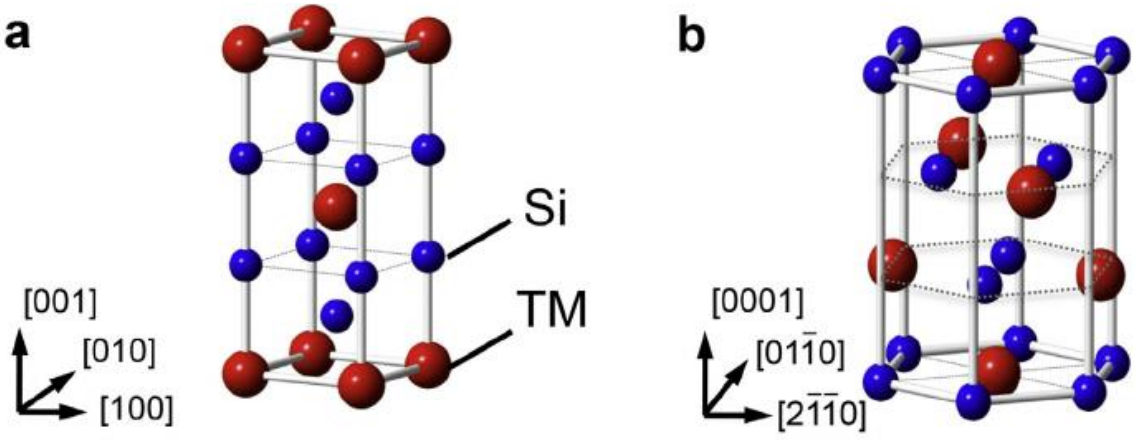

Figure 2.4: Atomic arrangements for the (a) tetragonal phase and the (b) hexagonal phase for a transition metal (TM) silicide.[44]

MoSi$_2$ can form the hexagonal phase which is metastable or in the thermodynamically stable tetragonal phase. The tetragonal and hexagonal phases have the atomic arrangements described in Figure 2.4a and 2.4b, respectively. The tetragonal phase is metallic and the hexagonal phase is semiconducting with a small bandgap of ~0.07 eV.[45] Only hexagonal phase is geometrically compatible as a substrate for silicene, and, therefore, growth conditions must be set to favor this phase.

Another benefit of semiconducting silicides as a silicene support is their compatibility with existing silicon technology. h-MoSi$_2$ can be synthesized on either Si(100) or Si(111) substrates. The Si substrates must be flash annealed to ~1200 ^{o}C, and imaged with the STM to check that the the 2x1 or 7x7 surface reconstructions are obtained for Si(100) and Si(111).[46] This method ensures there is no significant surface contamination. This cleaning process is the first step to synthesize silicene on h-MoSi$_2$.

2.2.2 Molybdenum (Mo) Thin Film Deposition

The second step silicene synthesis can be achieved by depositing a thin film of Molybdenum (Mo) onto atomically clean Si(100) or Si(111) substrates. This is a physical vapor deposition (PVD) method accomplished with e-beam deposition. The deposition is performed with the sample held at room temperature which results in nanocrystalline thin film of Mo. After deposition of Mo, the sample is annealed to 700-1000 ^{o}C for ~10-15 min which recovers nanoscale

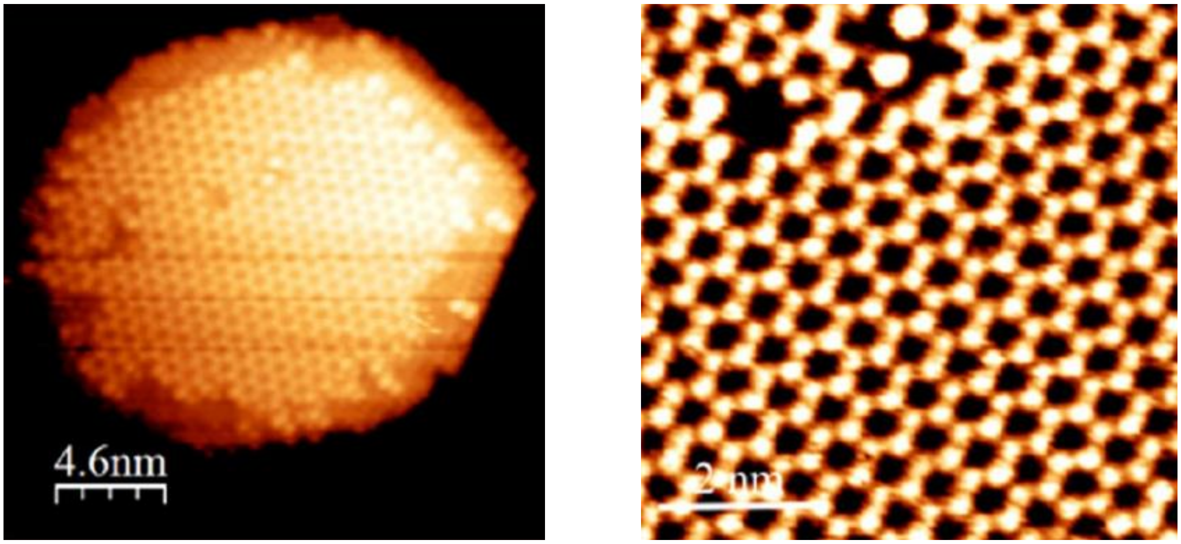

Figure 2.5: STM topography of (a) single silicene crystallite and (b) the apparent atomic structure. Imaging conditions: V_B = -1.7 V, I_t = 0.1 nA.[47]

crystallites of h-$MoSi_2$, many of which have a silicene or silicene-ribbon layer at the surface. Prior silicene results from the Reinke group are shown in Figure 2.5.[47] The ribbon-silicene synthesis is shown in Chapter 6 and was performed at Oak Ridge National Lab (ORNL) in a variable temperature STM chamber overseen by Dr. Gai.

2.2.3 Graphene/ Two-Dimensional Gallium Nitride/ Silicon Carbide (Gr/ 2D GaN/ SiC)

2D wide bandgap semiconductors are key to the advancement of 2D devices, which explains the popularity of 2D hexagonal-boron nitrite (h-BN).[7] Other group III nitrides have seen difficulty in synthesis due to challenges in cleaving, and stabilizing bulk tetragonal crystals in single or double layer form. Recently, a graphene encapsulation method was developed which allows for the synthesis of 2D GaN.[30] This heterostructure is formed by first synthesizing epitaxial graphene at a SiC surface via Si sublimation and converting it to quasi-freestanding graphene via hydrogenation. Then, trimethylgallium is used as the precursor to intercalate Ga under the graphene layers which is converted to GaN through a reaction with ammonia. The reactions take place in the graphene-SiC interstitial space. The samples were prepared by the Redwing group at Penn State University, and studied in our laboratory using STM and STS. Our work focuses on the STM characterization of samples to understand the mechanisms which control how Ga is intercalated under the graphene. Understanding which defects promote Ga intercalation will provide greater synthesis control for future work.

Chapter 3: Methods

3.1 Instrumentation and Techniques

The work described here was conducted under Ultra-High Vacuum (UHV) defined as 10^{-11} – 10^{-8} mbar). The UHV systems used for this work include a Scientia Omicron Variable Temperature (VT) STM, XPS, and Low Temperature High Magnetic Field (LTHB) STM, all of which will be described in detail in the following sections. All of these systems have the same general chamber structure as the VT-STM, involving an analysis chamber, preparation chamber and a loadlock, shown in Figure 3.1. The loadlock chamber has a small volume for rapid pumping and allows for samples to be transferred in and out of the UHV system. The low pressure ensures that the mean free path of O_2 and H_2O molecules is greater than the chamber diameter, severely limiting the interactions with the material to be characterized and its environment.

These chambers have various attachments that achieve deposition, deposition rate monitoring and annealing which will be described here. All of these components are sealed by flanges with a knife-edge around a Cu gasket. The base pressure is reached by a series of pumps combined with a bake-out procedure. These pumps include: a roughing pump (atmospheric pressure to 10^{-4} mbar), a turbomolecular pump (10^{-4} to 10^{-7} mbar), an ion pump (10^{-7} to 10^{-11} mbar), and a TSP (Titanium Sublimation Pump, used to reach 10^{-10} mbar more quickly after bakeout and when recovering vacuum quality during an experiment). For bakeout, the entire UHV system is heated to ~140 °C (above the desorption temperature of water from stainless steel) for 2 to 3 days. In conjunction, pumping and bakeout achieve the base pressure required for the characterization techniques that made this work possible.

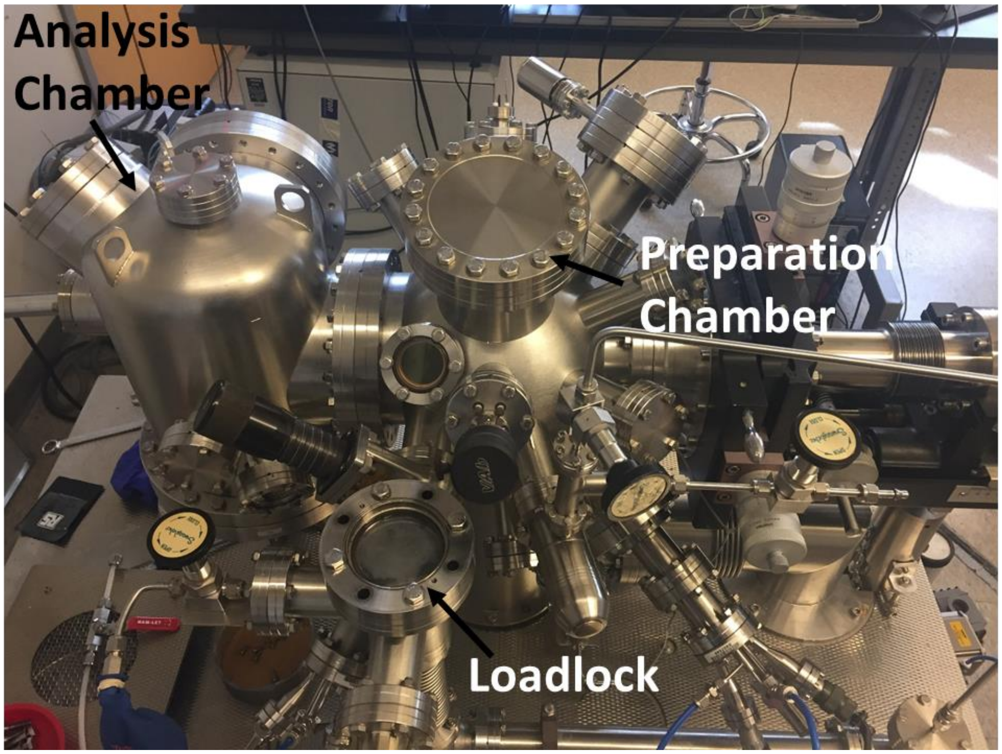

Figure 3.1: The Variable Temperature STM at UVa, showing a simple UHV setup with an analysis chamber, preparation chamber and loadlock.

The minimum base pressure required for STM and XPS UHV systems is slightly different. To achieve atomic resolution and avoid sample degradation in the STM the base pressure was kept $<3\times10^{-10}$. For XPS, a base pressure of $<8\times10^{-10}$ was sufficient for the electron mean free path to extend from the analyzer to the sample. The different characterization methods also differ in chamber structure, transfer components, deposition components, and annealing mechanisms. The XPS includes a preparation chamber in addition to the analysis and loadlock chamber. Transfer between chambers was made possible by the use of 4 different manipulators, and sample can be annealed in both the preparation chamber and analysis chamber.

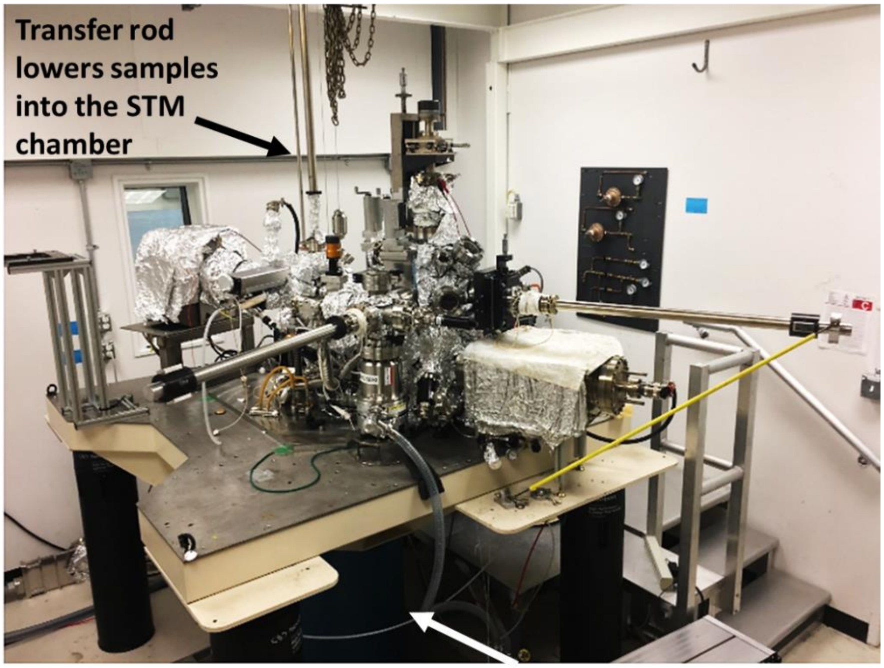

Transfer rod lowers samples into the STM chamber

STM chamber is suspended by a magnet

Figure 3.2: LTHB-STM system at Oak Ridge National Lab (ORNL). Shows the chamber geometry that utilizes a powerful magnet to mechanically isolate the analysis chamber.

The VT-STM at UVa has an analysis and preparation chamber that share vacuum and a loadlock, separated by valve. This STM is can operate while annealing the sample in situ, giving it the Variable Temperature prefix. The VT-STM is well suited for materials synthesis, with several e-beam sources for Physical Vapor Deposition (PVD) and a Crystal Quartz Monitor (QCM) to measure deposition rates. For sample transfer, the VT-STM is also equipped with a wobble stick and two manipulators (one of which is capable of heating the sample via e-beam or direct current annealing). Direct current annealing is necessary to recover the Si reconstruction, which is described further in Section 2.2.1.

The LTHB-STM at Oak Ridge National lab (ORNL) is shown in Figure 3.2. The “Low Temperature” prefix is used because this system is capable of cooling the sample and the tip to 77

K (liquid nitrogen) or 4 K liquid helium. This system is capable of the same annealing methods as VT-STM (e-beam and direct current annealing), but has fewer deposition capabilities and a more complex chamber structure. In addition to an analysis chamber and loadlock, the LTHB-STM has a preparation chamber and a transfer chamber, due to the geometry necessary for submersion in liquid Nitrogen or Helium (as shown in Figure 3.2). This transfer is achieved with the help of 6 different manipulators. The LTHB-STM also has two e-beam sources, which allow for PVD of metals.

3.2 Scanning Tunneling Microscopy (STM)

A portion of the work was carried out with a Scanning Tunneling Microscope (STM). This method analyzes the first (and occasionally second) layer of atoms on a surface. The signal we receive from the STM is proportional to the local electronic density of states (LDOS), and frequently, but not always, corresponds to the geometric arrangement of atoms.[48] STM is an excellent method for analyzing the geometric and electronic states of a surface at a small scale <500 nm. Therefore, it is a useful tool to study nanostructures and surface defects.

The STM obtains this information about the surface by bringing an atomically sharp tip very close to the surface of a sample and reading the tunneling current between the surface and the tip. The nanoscale motion used to approach and scan the surface is made possible through the use of a piezo-electric ceramics whose motion is controlled by a feedback loop, as illustrated in Figure 3.3. The tunneling current completes the circuit and is held constant by the feedback loop, which allows the tip to move across the surface without crashing or losing electrical contact. The STM's quantum mechanical tunneling current obeys the following proportionality:

$$I_t \propto V \rho_s(E_F) exp\left[\frac{-2z\sqrt{2m\phi}}{\hbar}\right]$$

Where V is the applied voltage, $\rho_s(E_F)$ is the density of states at the Fermi level, m is the mass of an electron, z is the distance between the tip and the sample, ħ is the reduced Planck's constant and ϕ is the barrier height for tunneling.[48] The tunneling current is a function of the local density of states and the tip-sample distance. This equation explains how the STM signal gives a combination of electronic and geometric information, which is always present in the measurement and can be difficult to untangle.

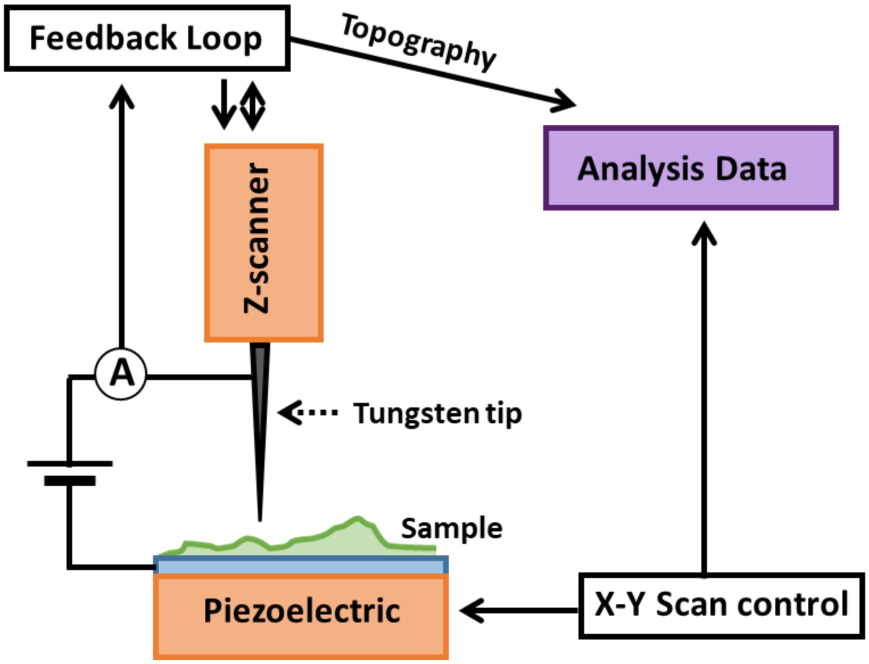

Figure 3.3: A schematic of the basic geometric and electronic signal configurations for an STM.

The tunneling current in STM can also be understood via band diagrams, as illustrated in Figure 3.4. This diagram emphasizes the importance of the bias voltage which controls the Fermi energies of the tip and the sample relative to each other, therefore determining which states contribute to the tunneling current. The example shown in Figure 3.4 is at a negative bias voltage and results in electrons tunneling from the tip to the sample thus probing the empty states in the sample. The bias voltage also dictates which states will be probed. For instance, when imaging a semiconductor, it is necessary to choose a bias voltage outside of the material's bandgap. The band diagram illustrates how the tunneling of electrons occurs from the valence band of the tip to the conduction band of the sample. In the experiments outlined here, the STM is always in constant current mode, in which the tunneling current is held constant and the tip-sample position is used to control the feedback loop.

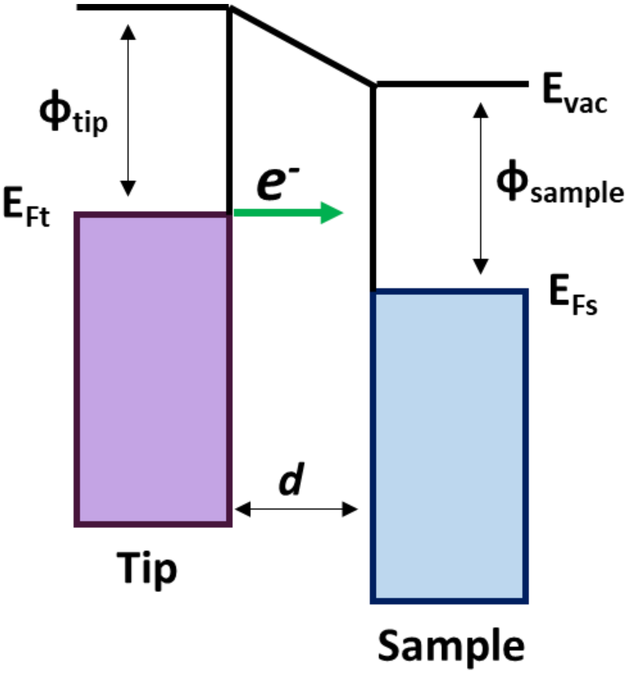

Figure 3.4: Illustration of energy as a function of distance in the z-direction. The bias voltage is negative for this example.

All of the operating principles described thus far can only achieve the desired image resolution, if the tip is sharp enough. Generally, an atomically sharp tip is desired, as this will enable atomically sharp image collection. For the work presented here, atomically sharp tips were achieved by electrochemically etching W wires in NaOH.[49] The tips are thermally cleaned during the bakeout process. This tip making process can create an atomically sharp tip but is not always successful. Therefore, all tips are tested on a graphite surface before being used to image a new sample. Graphite is a good test material as its surface has been well characterized with STM, and it is highly stable under UHV conditions.

The STM images in this work are analyzed using Gwyddion[50] and WSxM[51], which allow us to examine all the information collected. Methods like flattening and line averaging can reveal surface features that were hidden. Other common scanning probe techniques utilized in this analysis include: line scans, Fast Fourier Transforms, distance measurements and angle measurements. These methods give us quantitative results for a more precise understanding of the surface.

3.2.1 Cryogenic Scanning Tunneling Microscopy

STM can be limited by the mobility of atoms on the surface, which lowers the imaging resolution and leads to a higher signal-to-noise ratio Scanning Tunneling Spectroscopy (STS) and STM images. These problems can be solved by drastically reducing the temperature of the sample to either liquid nitrogen temperatures (77 K) or liquid helium temperatures (4 K). This process is especially useful when imaging metastable or highly defective surface structures and/ or high quality STS is desired. Some of the STM work presented here was measured with a LTHB-STM capable of cooling both the tip and the sample to 77 K.

3.3 Scanning Tunneling Spectroscopy (STS)

Similar to STM, Scanning Tunneling Spectroscopy (STS) measures the quantum tunneling of electrons through an atomically sharp tip to study the near-surface material properties. However, STS measures the surface with the feedback loop turned off, and the tip sample distance remains constant throughout the measurement.[48] Instead, the bias voltage is varied while the tunneling current is measured. This measurement can be taken at only one point, or the tip can be moved across the surface with a predetermined location and step size to obtain spectroscopy data along a line or on a grid. These measurements are best done on atomically flat surfaces because the tip-surface distance is constant during these measurements (feedback loop turned off). This process generates local I-V measurements. The I-V spectra allow us to determine the bandgap and local density of states (LDOS) at various points across the surface. The LDOS is proportional to the derivative of the current with respect to bias voltage, as illustrated in Figure 3.5. STS gives us an electronic characterization of the surface imaged and can frequently be used to help understand STM results.

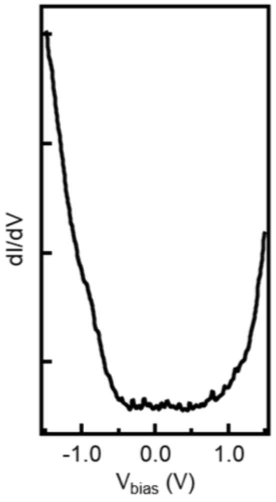

Figure 3.5: Differential conductance as a function of bias voltage for a Mo-Si sample.

3.3.1 Lock-in Technique

An alternate, and more precise, technique called “lock-in” is used to obtain spectroscopy measurements in the LTHB-STM system. This technique uses a lock-in detection amplifier which extracts the relevant frequencies from a noisy signal.[52] This technique also allows the differential conductance (dI/dV) to be measured directly from the surface.[53] Unfortunately, lock-in is only feasible under cryogenic conditions because it takes much longer to perform the measurement than at room temperature. For instance, the same grid spectra that takes 1 hour to complete using the I-V method may take 12 hours using the lock-in technique, due to thermal drift. However, the lock-in technique offers a much higher yield of good quality spectra and is more reliable. These spectra were analyzed with the software SPIP and Mountain SPIP.[54]

3.4 X-ray Photoelectron Spectroscopy (XPS)

Chapter 4 of this thesis utilizes XPS as the primary analysis method. XPS provides a surface sensitive measurement of the chemical nature of a conducting or semi-conducting material. This measurement is performed by irradiating the material with monochromatic Al Kα x-rays excites electrons to the detector, following the photoelectric effect.[55] These emitted electrons retain the chemical information of their original state. The kinetic energy of the emitted electron is related to the binding energy of the electron in its original state by the following equation:

$$E_{kin} = \hbar\omega - E_{bin} - \Phi$$

where E_{kin} = kinetic energy, $\hbar\omega$ = photon energy, E_{bin} = binding energy, Φ = work function of the material. This relationship can also be understood visually (Figure 3.6) through the three step model of electron transport to the surface. First, the electron is photoexcited by absorption of the photon. Then, the electron is transported to the surface, and, lastly, it must penetrate through the surface. These steps explain why electrons at different energy levels will be detected at different energies by the analyzer. The number of electrons emitted at a given energy determines how intense the peak will be.

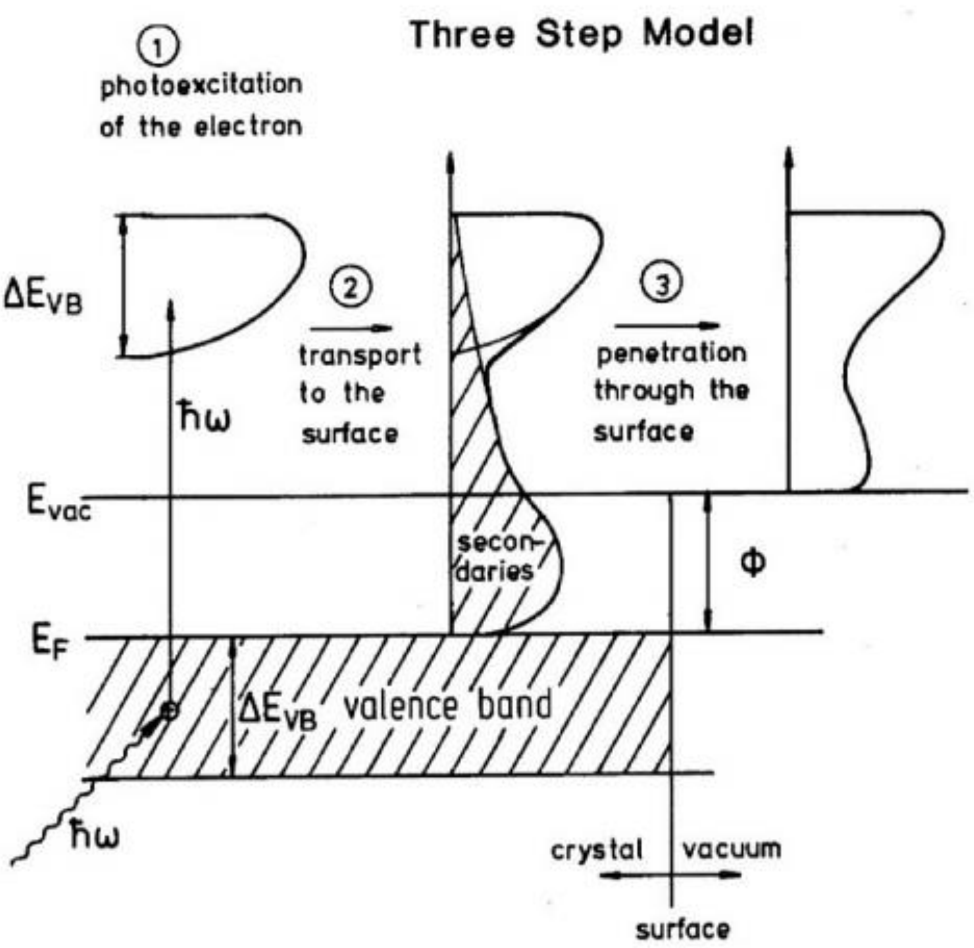

Figure 3.6: Schematic illustration of the photoemission three step model.[56]

The resultant XPS spectra is depicted as Intensity as a function of Binding Energy, as shown in the example spectrum Figure 3.7 which was observed for the Au4f peak in Chapter 4.

Each photoelectric peak corresponds to an element specific core level, with spin-orbit peak splitting occurring for the p, f, and d orbitals. Information can be gathered from the photoelectric peak integral, position, and shape. There are some peaks, however, that are the result of electrons emitted via alternate de-excitation processes, such as Auger peaks.[57] The energy of Auger electrons only depends on the element emitting the electron, making them independent of the x-ray source used. Auger emission involves a two electron process, making it difficult to relate the peaks to any chemical state. Analysis of Auger processes can be informative but will not be discussed at length as they are not the focus of this work. The excited electrons can also experience inelastic collisions during their journey to the surface. These secondary electrons result in an increasing background intensity with increasing binding energy, peak asymmetry in metals and plasmon loss peaks (energy lost to conduction electrons in a well-defined quanta). All of these factors will be considered as a part of the peak-fitting process.

The peaks given by XPS can be fit to a numerical function by minimizing the residuals. The peaks are fit by fitting the background noise with a Shirley Background function which accounts for the "stepped" nature. The step occurs because a portion of the photoexcited electrons undergo collisions and lose energy in the process, causing a higher background on the low kinetic or high binding energy side of each peak. The photoelectric peaks in this work are normally fit with a combination of a Gaussian and Lorenzian peak-fit called a Voigt function. However, if the peak has significant asymmetry, and Doniach-Sunic function is utilized which includes an asymmetry parameter.[58] All fitting in this work is done using KolXPD peak-fitting software.[59]

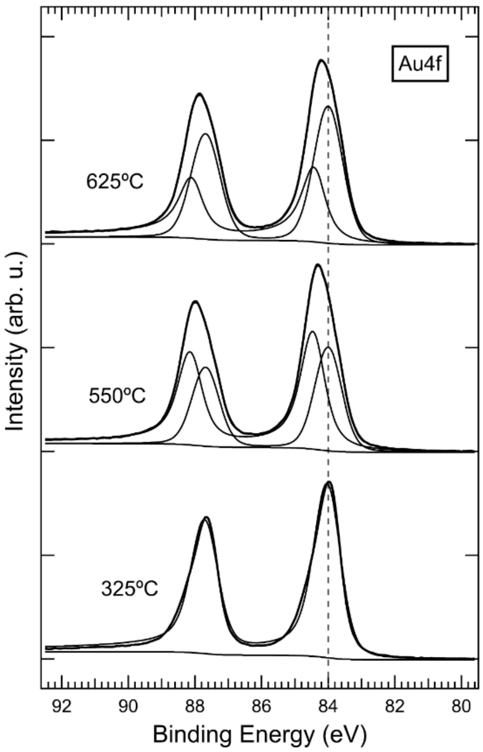

Figure 3.7: XPS spectra for the Au4f core level, in which pure Au is alloyed with Ti at high annealing temperatures, further described in Chapter 4.

Peak-fitting allows for the determination of the peak position, integral, and shape. The peak positions allow for elemental and bonding identification. In general, the larger the difference in electronegativity between to bonded atoms is, the greater the chemical shift to higher binding energies. The peak integral is related to the relative concentration of different chemical species and a number of other element properties. All effects beside the relative concentration can be eliminated by determining the ratio of peak integrals of different species after correcting for cross-section to obtain the species ratio:

$$\Theta = \frac{N_1}{N_2} = \frac{I_1/\sigma_1}{I_2/\sigma_2}$$

where $N_{1,2}$ = atomic concentration, $I_{1,2}$ = Intensity, $\sigma_{1,2}$ = photoemission cross section for the specified element and core level. The peak shape gives us information on range of oxidation states of the element, as it will be narrower when an element is present in one bonding state and broader when an element is present in a wider range. This effect is illustrated by the Au4f core level in Figure 3.7. The peak broadens as the Au reacts with Ti, forming a mix of solid Au and Au-Ti alloys.

The reason XPS is a surface sensitive technique is because the closer to the surface the excitation occurs, the more likely the electron is to be transported to the surface and emitted. Typically the depth probed is ~5-10 nm, depending on the material being analyzed. The depth probed varies between materials because different materials have different electron mean free paths. The Universal Curve, as shown in Figure 3.8, can be used to determine the mean free path for each element as a function of the electron kinetic energy. The photons used for this work are generated from an Al-Kα source which gives them a constant energy of 1486.6 eV. The exact relationship between intensity change and depth probed is given by the Beer-Lambert law:

$$I = I_0 \exp\left(-d/\lambda\right)$$

where I = intensity at a given depth, I_0 = maximum intensity possible, d = depth probed, and λ = electron mean free path. The depth probed can be made more surface sensitive by tilting the sample toward the x-ray beam.

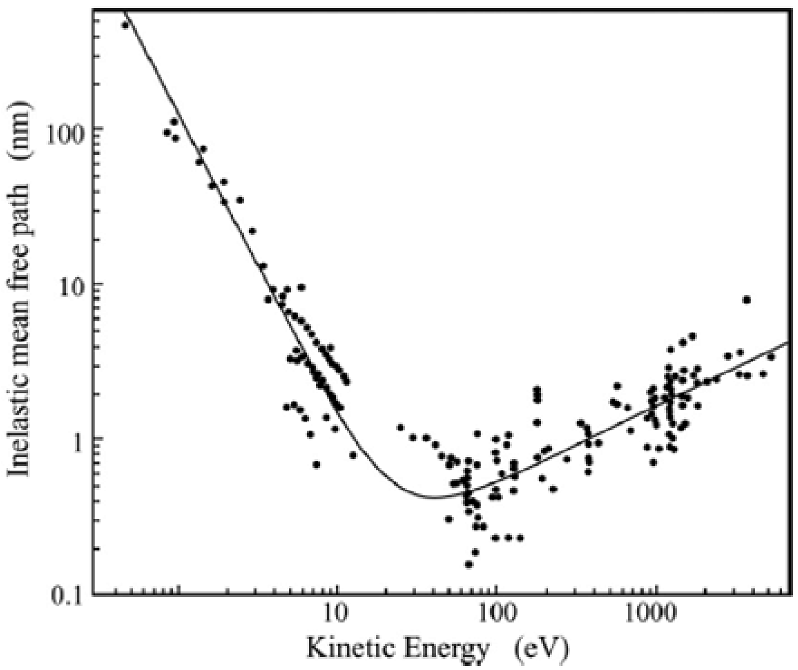

Figure 3.8: The universal curve shows the mean free path of a variety of elements for key electron kinetic energies.[60]

3.5 Materials Synthesis: e-beam Deposition

The metal depositions performed throughout this work are done using a Physical Vapor Deposition (PVD) process known as e-beam deposition. This technique was used to synthesize silicene/h-MoSi_2/Si, as described in Section 2.2.1. This process involves dual heating a W filament and a metal rod of source material at the same time. The metal rod accelerates electrons through the application of a high voltage of 2 k, and the filament heats the source by supplying thermal electrons. The amount of thermal electrons supplied can be tuned by slowly increasing the voltage applied to the filament until the desired filament current is reached. The filament current is proportional to the atomic flux going towards the sample. However, to find the atomic flux that reaches the sample, the source-sample distance must be considered. The precise atomic deposition rate for a given filament current is best determined with a Quartz Crystal Monitor (QCM). Unfortunately, the LTHB-STM was not equipped with a QCM, so the rates were measured at UVa and approximated according to the proportionality

$$r \propto \frac{1}{d^2}$$

where r = atomic deposition rate and d = source-sample distance. These approximations were confirmed by comparing the surface coverage observed with the LTHB-STM and comparing it with that observed with the VT-STM.

3.6 Publication Data Preparation and Analysis

Materials science knowledge coupled with machine learning shed light on a variety of materials science problems, uncovering new information and reinforcing existing claims. Machine Learning (ML) methods can provide the key descriptors for a number of materials science problems.[17,18] In this work, a dataset was manually compiled by examining the results of past publications on a specific synthesis method for monolayer MoS_2. The dataset was trimmed down to only consist of publications that included all quantitative values for the synthesis parameters we deemed necessary. The dataset was then used to map out the parameter space of the synthesis method in question using data-driven methods. Knowledge of the parameter space for a given 2D material aids its future incorporation into heterostructure devices. Despite the small size of the database, inherent in manual compilation due to time constraints, data-driven methods have been shown to be capable of finding meaningful trends within datasets of a similar size.

Chapter 4:

“Thermally Induced Reactions of Monolayer WS_2 with Au-Ti Substrates”

Anna Costine[1], Jose J. Fonseca[2], Jeremy T. Robinson[2], Cory D. Cress[2], Petra Reinke[1]

[1]Department of Materials Science and Engineering, University of Virginia,
Charlottesville, VA 22904

[2]Electronics Science and Technology Division, U.S. Naval Research Laboratory,
Washington, D.C. 20375

My contribution to this work is the characterization of all samples provided by NRL, including the observation of the thermally induced reactions with XPS, data analysis and writing of the manuscript. This manuscript is currently finalized after integration of information on sample preparation by our co-authors. It will be submitted to Applied Surface Science.

4.1 Introduction

Two dimensional transition metal dichalcogenides (2D TMDs) have garnered attention in recent years owing to their unique electronic and optical properties, which hold promise for many device applications.[23,24,27,36,61,62] Bulk TMDs form a layered structure with strong in-plane covalent bonding and Van der Waals bonding between the layers.[63] This structure allows the bulk materials to be exfoliated down to a single layer, which drastically alters the electronic and optical material properties.[63] Decreasing the number of layers in TMDs from a few layers to a single layer increases the bandgap and results in an indirect-to-direct bandgap transition.[64,65] The magnitude of the monolayer TMD’s direct bandgap is in the visible light energy range, making these materials a viable option for optical devices.[23,24] Monolayer TMDs also boast a strong spin-valley coupling and high catalytic activity.[23,66]

However, as with all 2D materials, the interaction between the TMD and the substrate in question has a large influence on the material's performance.[63,67] This interaction is dictated by the inherent interaction between the two materials as well as by the quality of the interface between them. [27,63,68] In the direct growth methods such as CVD (chemical vapor deposition) and MBE (molecular beam epitaxy) the substrates which yield the highest quality material are in general chosen for proper lattice matching, which drastically decreases the number of potential substrates.[63,67] CVD and MBE for growth of van der Waals heterostructures for the integration of 2D materials is still limited by unwanted reactions between precursors and materials degradation at the requisite high synthesis temperatures.[68–70] The assembly of van der Waals heterostructures made of TMDs therefore still relies on layer by layer stacking via mechanical transfer, which is still based on permutations of the scotch tape method [69,63] The downside of this synthesis method is that it often leaves behind a polymer residue that reduces the quality of the interface and is difficult to remove completely.

The removal of this residue, even incompletely, via annealing has been shown to improve the electrical properties of TMDs. However, this annealing can also result in changes to the chemical and electrical structure of the material.[71–73] For instance, Zhao et al. showed that sulfur desorbs from MoS_2 during vacuum annealing, even at relatively low temperatures (~250 C),[74] and results in p-type doping. The degree of doping as a function of temperature can be observed with X-ray Photoelectron Spectroscopy (XPS) by measuring the chemical shift in the Sulfur and

Molybdenum core levels.[74] Zhao et al's work emphasized the potential for XPS to analyze subtle changes in the chemical structure of TMDs.

Thermal degradation of TMD devices due to local heating caused by current or light absorption can be a concern for a number of potential applications including Field-effect transistors (FETs), gas sensors, and optical devices, and often limits the permissible processing conditions for device assembly.[25,27,62,66] For example, gas sensors frequently involve intentional heating of the TMD in order to completely desorb the gas molecules for recovery and increased efficiency.[25] It is therefore important to assess the thermal stability of heterostructures where the TMD layer is in contact with residue from exfoliation, and substrates such as Au or other metals which mimic typical device structures in use. It is therefore of significant interest for the community to understand thermally induced changes in the TMD layers during processing and operation.

This publication explores chemical reactions in the WS_2-Au-Ti multilayer system, which still includes some polymer residue from the TMD transfer, that occur during annealing to temperatures up to 625 ºC in ultrahigh vacuum (UHV). This multilayer system is often used for TMD integration, and a common substrate for exfoliated WS_2 and MoS_2.[24,36,62,63] Au is a popular substrate due to its positive effect on the catalytic properties of TMDs, and its use as an electrode in FETs,[61,75] and Ti is used as a sticking agent to improve adhesion of Au to the Si/SiO_2 substrate in our samples. The complex chemical reactions, which play out in this system during heating are studied with XPS using a temperature resolution of 25ºC. The reactions include interdiffusion and alloying of the Au-Ti substrate, reactions of Ti with remnants of the adhesive used for WS_2 exfoliation, and the degradation of WS_2. We will discuss the competing reaction pathways for residue- WS_2-Au-Ti, and residue-Au-Ti samples to understand the role of WS_2 on the reactions.

4.2 Experimental

The TMD layers are transferred by a micromechanical exfoliation on a stack of SiO_2/Si substrate covered with a Ti/Au layer. The SiO_2/Si substrate is treated with an oxygen plasma to remove surface contamination. Subsequent to the cleaning step a 5 nm thick Ti-layer, which serves as an adhesion layer, is deposited by electron beam evaporation followed by deposition of a 30 nm nanocrystalline Au layer. A bulk WS_2 sample is pressed onto the Au surface and peeled away, leaving behind patches of multilayer WS_2. The material is then exfoliated using scotch tape until monolayer regions are produced. Optical microscopy images of the sample after the last exfoliation step are include in the Section 4.4 Figure 4.9, and the different regions are labeled accordingly. The XPS analysis spot was positioned to maximize the WS_2 signal, and is marked in Figure 4.9 – no SiO_2/Si from the fiducial markers was detected due to their small area, and the low cross section for the Si2p peak.

Two WS_2/Au/Ti samples and one Au/Ti sample were annealed at temperatures from 275-625 °C under ultrahigh vacuum with a base pressure below 10^{-9} mbar. The annealing was achieved with a p-BN resistive heater, and XPS measurements were performed after each annealing step after the samples had cooled down to T<100 °C. The first WS_2 sample, henceforth labelled as *sample C*, was annealed in larger increments of 75-100 °C to identify the critical temperature range in which the majority of reactions occur. The second WS_2 sample, *sample A*, was annealed in the same temperature range but in smaller increments of 12.5 to 25 °C to resolve reaction steps in more detail. The Au/Ti sample, *sample B*, which includes no TMD, was made by pressing scotch tape on the Au surface to isolate the impact of residue left behind during the mechanical exfoliation of

WS_2. Sample B was examined in the temperature range from 375 to 625 °C with increments of 12.5 to 25 °C to allow for direct comparison with sample A. All samples were brought to the annealing temperature as quickly as the chamber pressure allowed (about 20 min), held at the annealing temperature for 10 min, and then cooled down for XPS measurements. The temperature protocol is summarized in the Section 4.4 Figure 4.10. This temperature protocol leads to an overall larger thermal load for the smaller annealing increments compared to the larger temperature increment experiment, as illustrated in Section 4.4 Figure 4.11. The impact of long/short increment scenarios will be compared, and the role of heating load will be discussed.

Photoelectron Spectroscopy in the x-ray regime (XPS) of all core level regions of relevance was performed after each annealing step with a Scientia Omicron Multiprobe MXPS. Monochromatic AlK_α ($h\nu = 1486.6$ eV) photon energy was used to obtain core level spectra (XM1200 monochromator) and the spectra were collected in the same location on the sample for all annealing steps. A constant pass energy of 50 eV was used for the core level spectra and yields a resolution of 0.5 eV. The resultant spectra were aligned to the Fermi level of a clean Au sample (84.0 eV). For two set of spectra measured on *sample C*, the W4f and C1s core level, a slight shift of the core levels due to minimal charging by 0.2-0.3 eV was corrected by alignment of the spectra at the energy of the W metal, the WS_2 core levels, and the TiC core level for C1s. Compositions are calculated using the peak area corrected by the cross sections provided by Scofield et al. for each core level.[76]

All XPS data were analyzed using the KolXPD software.[59] The Doniach-Sunjic function convoluted with a Gaussian function was used to fit the metal core levels and accounts for their asymmetry, while a Voigt function was suitable for all other core levels.[58] A Shirley background was used for all core levels except S2p, whose background is modified due to superposition with a Ti-core level and could be described better using a linear background.[77] The quality of the respective core level fits include here were determined based on the assessment of the residuals.

4.3 Results

The W4f spectra for a selection of temperatures are shown in Figure 4.1, and the complete set of spectra for all core levels, and all temperatures are included in the Section 4.4 Figure 4.12. The W4f core levels contain a several chemical species identified as WO_2, $WS_{2(-x)}$, and metallic W whose relative contributions change significantly with temperature. Unfortunately, the Ti initially bound in the sticking layer, which is outside the information depth of XPS, diffuses into the Au-layer, and initiates the formation of Au-Ti alloys close to the surface, and at the interface with WS_2. The Ti3p peak has a binding energy of 35-40 eV and overlaps with the W4f peaks and negatively impacts the reliability of peak fitting. The Ti3p can be seen as a broad peak on the high binding energy side of the W4f peak at higher annealing temperatures. The Ti3p core level is clearly isolated in sample B, which does not include WS_2, and is shown in more detail in Section 4.4 Figure 4.13. Ti is highly reactive and forms a wide range of compounds, which is reflected in the C1s, S2p, and Au4f core level spectra discussed in detail later.

The complexity of the W4f peak, and its convolution with the Ti3p core level, impedes quantitative assessment of different chemically shifted contributions using a fit procedure. Instead, we used peak subtraction to isolate the effect of temperature on the material system, and a selection of representative spectra is shown in Figure 4.1a. The complete set of spectra for sample A across the entire annealing temperature range is included in the Section 4.4 Figure 4.13a. The subtraction is performed by normalizing all spectra to unit height, and the spectrum measured at the lowest annealing temperature (275 °C) is then subtracted from the respective core level spectrum measured at higher annealing temperature. The most intense peak at 33.0 eV corresponds to the $W4f_{7/2}$ peak for WS_2 which moves by ~0.25 eV to lower binding energy during annealing, as shown in Figure 4.1b. This shift can be attributed to the introduction of S-vacancies and associated p-type doping,[74] and is mirrored in the S2p peak position. The first change in the spectral shape occurs at T=400 and 450 ºC and is seen as a reduction in the intensity of the shoulder on the high binding energy side of the WS_2 peak. This spectral shape change is reflected in the subtraction spectra as the introduction of two minima at binding energies of 33.4 eV ($W4f_{7/2}$) and 35.5 eV ($W4f_{5/2}$). These minima have the expected branching ratio of 3:4 and energy separation of 2.2 eV of the W4f peak and correspond to the literature values of WO_2.[78–80] The oxide doublet is marked by dashed lines in the peak subtraction spectra and labeled (a).

The oxide contribution is significantly reduced at T>450 ºC and nearly disappears above 600 ºC. At this temperature, the W4f core level is composed of only WS_2 contributions. Inspection of the WS_2 peak indicates that it is actually composed of two W4f doublets, which are slightly shifted with respect to each other by ~0.4 eV. The positions of these peaks are marked by dashed lines labeled (b) and (c) in Figure 4.1a. The origin of these two contributions remains speculative and might be related to different defect densities, or the presence of different amounts of residue polymer on the WS_2 flakes leading to slightly shifted WS_2 core levels. Also at higher temperatures (>600 ºC), the difference spectra shows an increase in the Ti concentration which is seen as a local maxima in the high binding energy side of the W4f peak, and through the apparent distortion of the W4f doublet branching ratio in the difference spectra. This observation agrees with the the increase and broadening of the Ti3p peak, shown in section 4.4 Figure 4.11 for sample B. At the highest temperature (625 ºC), an additional peak emerges at binding energies of 31.1 eV and 33.2

eV which corresponds to W metal,[81] and is labeled as (d) in Figure 4.1a. This result is in agreement with the reduction of WS_2 due to sulfur loss throughout the annealing steps.

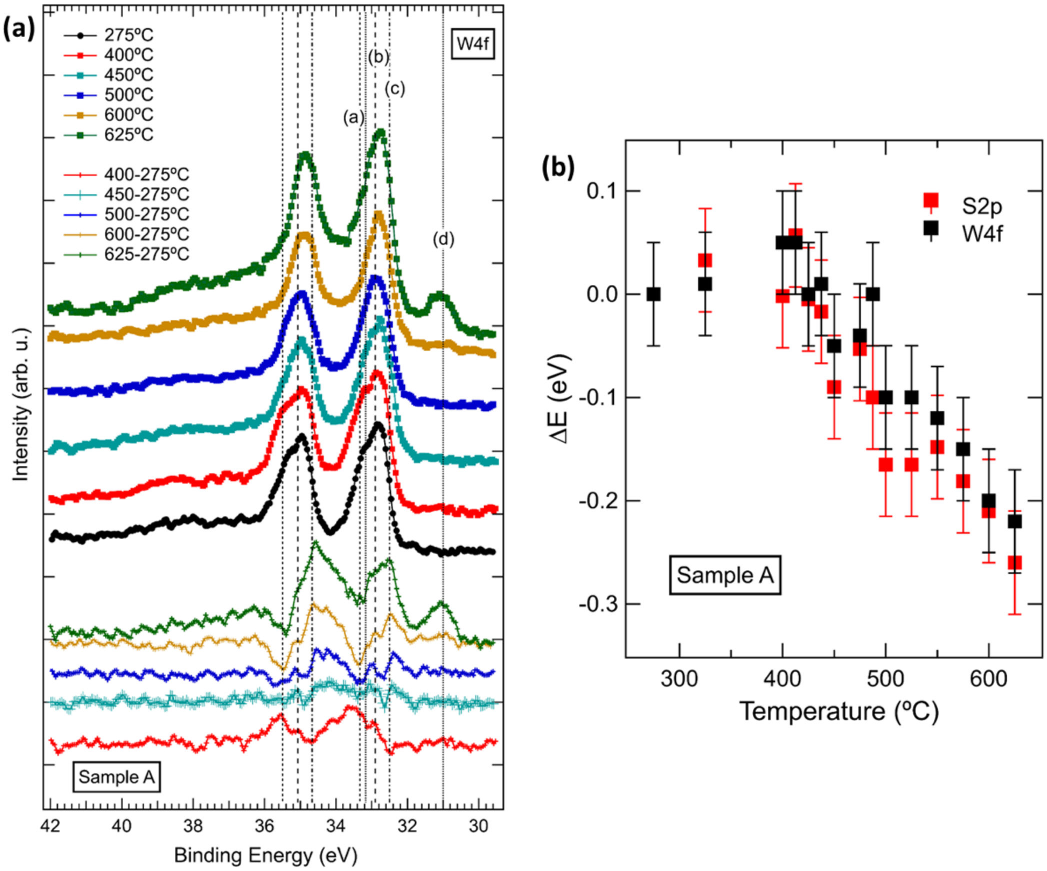

Figure 4.1: (a) Sample A - W4f core level spectra for select annealing temperatures, and difference spectra. The core level spectrum measured at 275 °C was subtracted from the core level spectra measured for the other annealing temperatures. The spectra are vertically offset for illustration. (b) Binding energy shift for the peak maxima in $W4f_{7/2}$ and $S2p_{3/2}$ core levels as a function of annealing temperature.

Figure 4.2 summarizes the S2p core level peak for select temperatures for sample A. Overall, the peak shape remains unchanged up to 500 °C when a small shoulder emerges at about 161.0 eV on the low binding energy side. This position is commensurate with the formation of Ti_2S_3 by a solid state reaction between WS_2 and Ti from the Au-Ti alloy (see next section for details).[82] The major contribution to the S2p peak can be fit with a doublet initially positioned at 162.6 and 163.8 eV, which shifts by 0.3 eV to lower binding energies as summarized in Figure 4.1b, and has an FWHM (full width at half maximum) of 0.52 eV in agreement with the literature.[80] The shift to lower binding energy is in parallel with the binding energy shift in the W4f spectra. As stated previously, the shift is due to the onset of sulfur loss via sublimation and concurrent p-type doping, and consequently shift of the Fermi level in the gap. Evidence for sulfur loss is also seen in the decreasing S/W ratio from 2.0 to 1.4 ± 0.3. The large standard deviation on the S/W ratio is due to the complexity of the W-chemical environment, and the associated challenge to quantify the WS_2 contribution to the W4f peak.

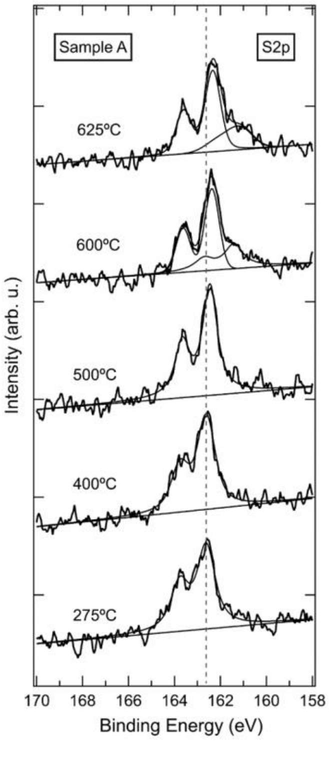

Figure 4.2: S2p core level spectra for select annealing temperatures. The peak maximum at 162.6 eV for 275 ºC is marked by a dashed line as a visual guide.

In sample A, Ti diffuses through the Au layer and is incorporated into the Au lattice prior to its reaction with other materials on the surface.[83] The evidence for alloying is found in the modulation of the Au4f spectra, as shown in Figure 4.3a, and no titanium was detected before annealing in the as-introduced sample. The Au4f doublet shifts to higher binding energies by 0.3 eV, and broadens from an FWHM of 0.57 eV which is identical to the calibration Au sample, to 1.1 eV at 375 ºC followed by a decrease to 0.92 eV at 650 ºC, and a peak shift back to 84.1 eV.[84] The Au4f spectra are best understood by fitting two doublets: one held at 84.0 eV (the Au4f core level position of the initial nanocrystalline Au layer) and another that is allowed to shift in binding energy position (the alloy). The branching ratio and peak splitting is held constant (3.7 eV) for both spin-orbit doublets. The plasmon peak for Au4f is not included in the fit, which leads to a small mismatch between the fit envelope and signal at ~85.0 eV. The fit leads consistently to an excellent description of the Au4f peak shape across the entire temperature range. The chemical shift of Au4f is within the range expected for a Au_2Ti alloy reported in the literature, although small variations in position of this peak can be attributed to variations in composition over the volume probed with XPS.[83,84]

Figure 4.3c shows the variation in peak position for the $Au4f_{7/2}$ maximum, and the contributions of the alloy component to the Au peak. The shift in peak position reflects the increasing alloy contributions clearly seen in the fit, which reaches a maximum at 375 ºC followed by a reduction in the alloy contributions at higher temperature. Rapid Ti diffusion from the sticking layer to the Au-surface and alloying start at relatively low temperatures, and surface alloying is gradually yet incompletely reversed at higher temperatures. In contrast, for sample B, shown in in Figure 4.4b, only a small contribution from the Au-Ti alloy can be identified via a peak shift of the Au4f peak from 84.0 eV at room temperature to ~84.1 eV at 375 ºC, which is also reversed at higher annealing temperature. From these data, it can be inferred that the sample without WS_2 (sample B) shows a much smaller degree of alloying and consequently de-alloying than sample A, although the reaction trends are the same.

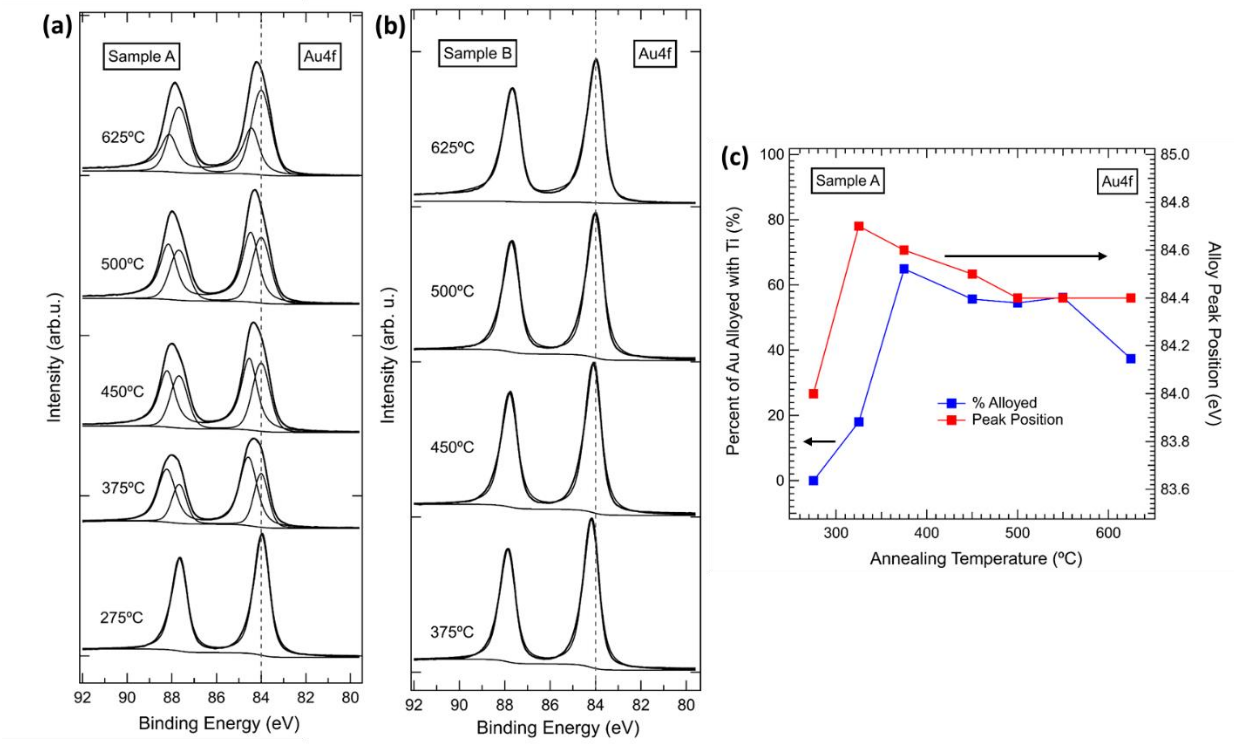

Figure 4.3: Au4f core level spectra for select annealing temperatures. (a) Sample A, and (b) Sample B (no WS_2) - peak maximum at the lowest annealing temperature is marked by a dashed line at 84.0 eV. The fit includes a second component at higher binding energy from the Au-Ti alloy. The spectra are vertically offset for illustration. (c) Percent of Au alloyed with Ti (left axis) and $Au4f_{7/2}$ binding energy shift (right axis) as a function of annealing temperature for Sample A.

Titanium has a strong tendency to react with carbon from adventitious carbon, carbon and oxygen from the surface residue, and even, at higher temperatures, with WS_2. This creates a significant driving force for diffusion, which is rapid due to the high density of grain boundaries in the nanocrystalline Au layer. The dealloying process occurs at higher temperatures, the Ti concentration in the Au-Ti alloy is reduced, and Ti is consumed in the interfacial chemical reactions. The decrease in alloyed Ti is observed for annealing temperatures greater than 450 to 500 ºC, when the more thermodynamically favorable reaction between titanium and oxygen is also kinetically favorable. Therefore, the alloying-dealloying with the Au-substrate occurs as an intermediate step on titanium's journey to react with the surface residue.

Figure 4.4 illustrates the changes in C1s spectra during annealing for samples A and B. The C1s peak position is constant at 284.7 eV from 275-400 °C, and gradually shifts to lower binding energies eventually reaching 284.0 eV at 600 ºC for sample A and 284.4 eV for sample B. The peak shift and modulation of the peak shape are characteristic for the transition from a polymeric structure at lower temperatures to a more graphitic material due to hydrogen loss.[85,86] This transition is nearly complete for sample A at 625 ºC. For sample B, some polymeric contributions can still be identified at the highest temperature. We suggest that the larger thickness of the residue, which is reflected in the higher initial carbon and oxygen concentration in sample B (see Figure 4.6) delays the completion of graphitization in the residue layer. Residue contributions in sample A arise from the lateral diffusion and creep of residue polymer across the sample surface leading to a smaller overall carbon concentration and a thinner carbonaceous layer compared to sample B.

The C1s peak can be fit with a maximum of four components: (i) the polymer contributions at ~285.0 eV, (ii) graphitic contribution at 284.2- 284.4 eV, (iii) a small carbide contribution at ~283.4 eV and an additional carbide peak at 281.9 eV. The polymer component is relatively broad since it represents a wide range of bonding environments including C-H, and C-O bonds, which are located in the higher binding energy tail. The graphitization reaction occurs in parallel with carbide formation, which is more pronounced in sample A. Figure 4.4 shows the carbide peak at a binding energy of ~281.9 eV in the C1s spectra of both samples, which agrees well with the literature values for titanium carbides [87,88] and the shallow peak at 283.4 eV is attributed to a sub-stoichiometric TiC. The carbide is assigned to titanium by process of elimination: no corresponding carbide peaks appear in the W4f spectra. The comparison between samples shows significantly less carbide formation in sample B compared to sample A, where the carbide contribution relative to total carbon increases from 4% to 12% between 500 and 625 ºC.

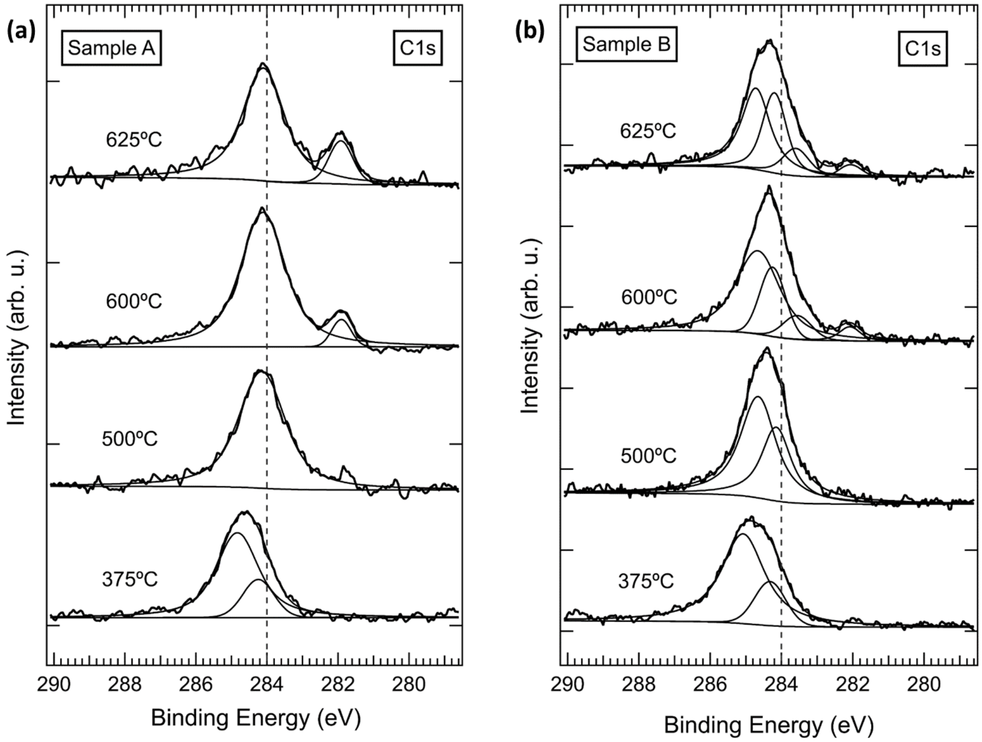

Figure 4.4: C1s core level spectra for select annealing temperatures. (a) Sample A, and (b) Sample B (no WS_2). The peak maxima at 375°C is positioned at 284.0 eV for sample A, and B and marked by a dashed line as a guidance for the eye. The spectra are vertically offset for illustration.

The progression of the reaction between Ti and O can be seen in the Ti2p spectra for Sample B (Figure 4.5). The spectrum initially shows one distinct doublet, which broadens as new chemically shifted components emerge. It is important to note that no titanium was detected before annealing in the as-introduced samples, while titanium is already detected at the lowest annealing temperatures for all samples. At 375 ºC one doublet is positioned at ~459.5 eV (465 eV), which corresponds to the literature values for TiO_2, the most thermodynamically stable titanium oxide.[89] As the temperature is increased several chemically shifted components appear and correspond to a wider range of oxidation state which coexist at the interface. These states correspond to the sub-stoichiometric titanium oxides, TiO_{2-x} located at ~457 eV and TiO located at ~455 eV.[89] The oxides are stabilized due to the limited oxygen supply available for the solid state reaction of Ti. Essentially, as more Ti metal diffuses to the surface, it reduces the TiO_2, and forms sub-stoichiometric oxides which is seen in the evolution of the Ti2p core level with temperature. While it is not possible to analyze the Ti-core level for sample A directly, the O1s spectra summarized in Section 4.4 Figure 4.14 support the presence of TiO_2 as well as sub-stoichiometric, oxygen-deficient material. The oxygen contributions from the polymeric material are diminished, and Ti-oxide contributions increase with temperature.

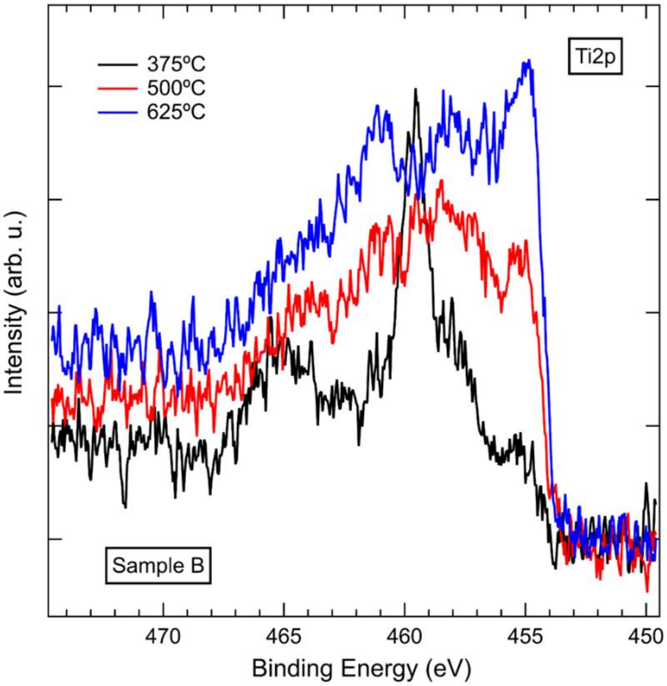

Figure 4.5: Ti2p core level spectra of Sample B at select annealing temperatures. The spectra are vertically aligned for illustration.

Figure 4.6 summarizes the fractional composition of samples A and B of the near-surface region for Ti, Au, C and O. W and S are excluded from this graph to allow for a direct comparison between samples A and B. The general trends are similar between samples A and B, although they differ in magnitude. For both samples, the C/O ratio is constant for T>400 ºC, and the carbon loss at lower temperatures can be attributed to desorption of adventitious carbon, and the compaction of the polymer during the transition to a more graphitic layer. The higher residue load of sample B is a consequence of the sample preparation where the whole sample surface is covered with

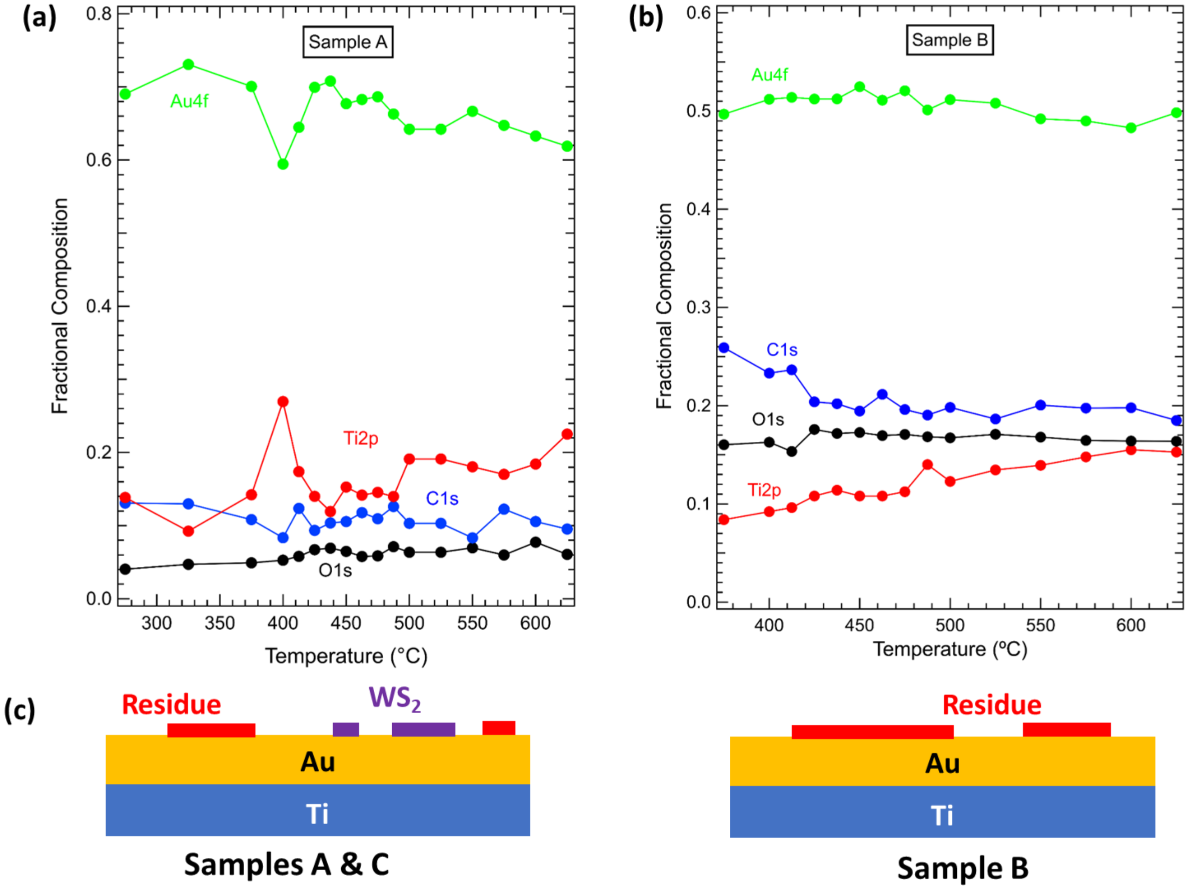

Figure 4.6: Fractional composition of Au, Ti, C, and O for (a) Sample A (small temperature increments), and (b) Sample B (small temperature increments, no WS_2). (c) Schematic showing the geometry of samples A, B, and C before annealing.

residue (see Section 4.4 Figure 4.9). The titanium concentration increases with temperature relative to the other elements and the decrease in the Au contribution is a reflection of alloy formation which reduces the amount of Au within the XPS probe volume. Titanium reacts preferentially with oxygen from the residue and forms less carbide (Figure 4.5) and alloy (Figure 4.4) in sample B compared to A. The fractional composition of oxygen for sample B yields a composition close to TiO, in agreement with the Ti2p core level structure shown in Figure 4.6 with a sizable contribution of sub-stoichiometric oxide. The higher residue load on sample B explains many of the quantitative differences observed in the spectra and the general reaction trends with temperature are independent of sample type, and mostly controlled by the availability of oxygen in the residue to drive the solid state reaction with Ti.

The influence of thermal load was studied by performing an additional experiment - sample C - with a smaller number of annealing steps used to reach the same maximum annealing temperature. This method results in a much smaller cumulative annealing time and thermal load as shown in Section 4.4 Figure 4.11. The overall heating protocol, and isothermal heating time at T_n are the same for all samples (Section 4.4 Figure 4.10). Figure 4.7 shows the W4f, C1s and Au4f core levels for sample C at select annealing temperatures: 325, 375, 550, and 625 ^oC. The differences between the two experiments are seen by comparing the spectra for sample C in Figure 4.7 with those for sample A in Figures 4.3 and 4.4. Differences in thermal load can potentially affect the initiation temperature and progression of different reactions, and the comparison between samples A and C might shed light on this question. It should be noted here that the WS_2 coverage for sample A is about 25% of the probed area, but only about 10% for sample C. There are a few key differences in how the reactions progress, but the general reaction trends still remain the same.

The most notable difference between the large and small thermal loads is the relatively large amount of W-oxides that are present in sample C, which is seen in the prominent peak at higher binding energies around 35.5 eV (Figure 4.7a). The larger oxide contribution might be caused by an overall lower sample quality, oxidation of defects, or reactions at the perimeter of WS_2 flakes during air exposure. The contribution from W-oxides is reduced at 550 ºC commensurate with the observations made for sample A. Unfortunately, the quite significant contributions from the Ti-core level lead to an intense background which allows only for a qualitative comparison.

The changes in Au4f spectra with temperature (Figure 4.7a) show a significantly larger amount of Ti-Au alloy in sample C compared to sample A. The fit of the Au4f peaks, the shift of the core level position, FWHM of the core level peaks, and the decrease in overall Au concentration (Figure 4.8), are signatures of the large contribution from the Au-Ti alloy in the near-surface region, and no de-alloying can be detected. The reaction between carbon and titanium proceeds to a greater extent (Figure 4.7e), and the carbide reaction is initiated already at 550°C for sample C. The carbide peak accounts for 22% of the total surface carbon at 625°C but only 12% of the total carbon at 625°C for sample A (Figure 4.7c). Another key difference is the only partial transition from polymeric to graphitic bonding, which progresses much farther with larger thermal loads (sample A), and is slower for larger volumes (sample B). The significant amount of restructuring required for graphitization explains the sluggish progression of this reaction.

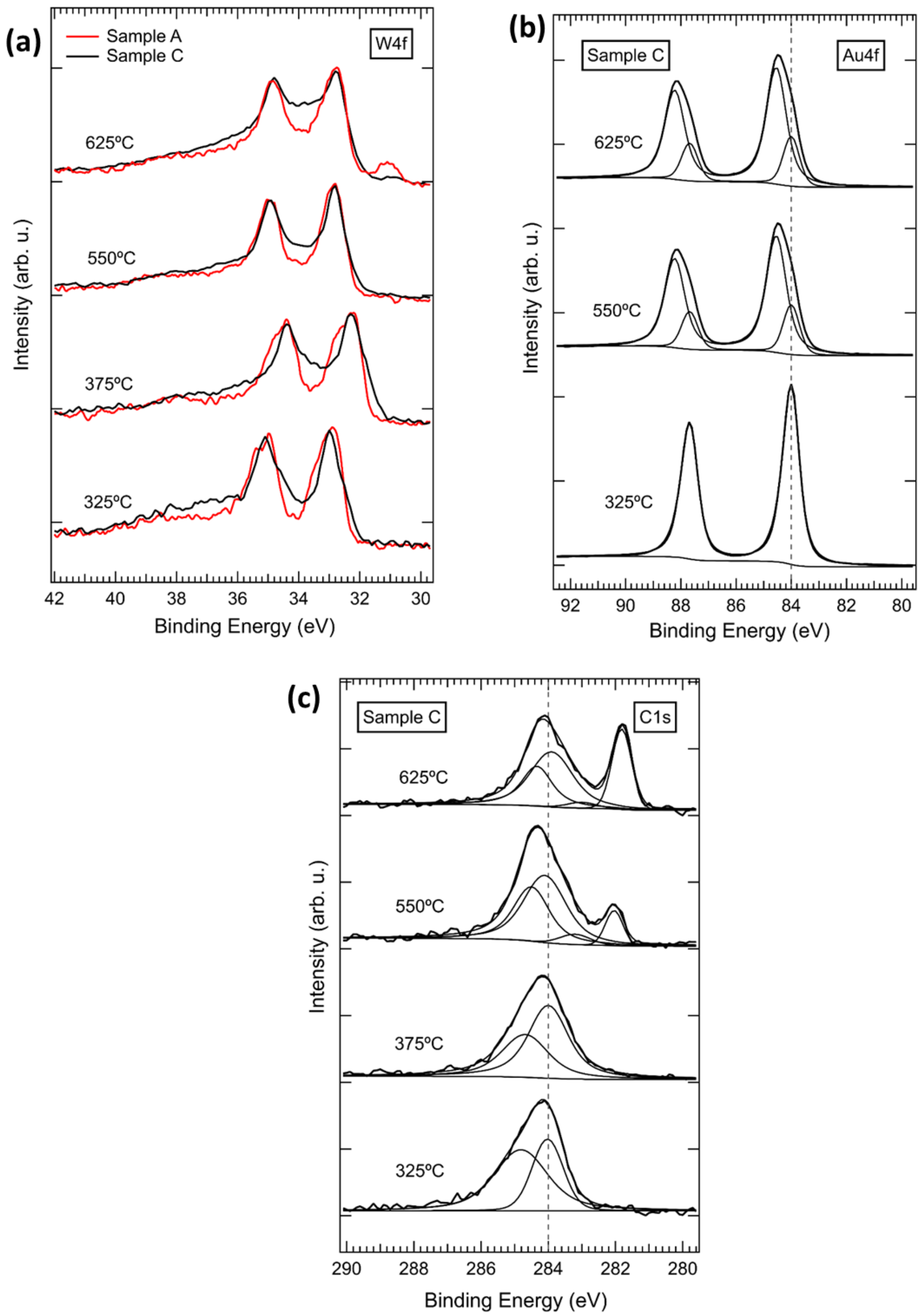

Figure 4.7. Core level spectra: (a) **W4f** sample A and sample C, normalized select spectra, (b) sample C, **Au4f**, select spectra and (c) sample C, **C1s**, select spectra.

A tentative explanation can be offered to understand the different behavior for samples A and C: the smaller thermal load in sample C imposes kinetic limitation on the competing solid state reactions, and favors carburization of Ti over oxidation – oxygen is distributed within the polymer and its reaction with Ti is sterically hindered and occurs preferably after prolonged annealing. On the other hand, a higher thermal load in sample A and earlier onset of graphitization facilitates the thermodynamically preferred oxidation reaction to the detriment of carbide formation, and promotes rapid use of Ti and consequently de-alloying.

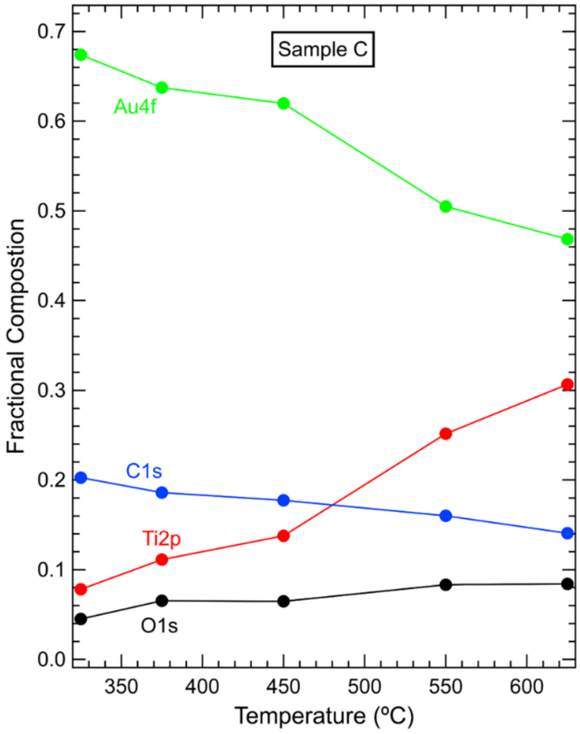

Figure 4.8: Fractional composition including Au, Ti, C, and O for Sample C (larger annealing temperature steps, and WS_2 interlayer).

4.4 Supporting Information

Figure 4.9 includes the optical micrographs of Sample C (S1a) and Sample A (S1b) taken with a Hirox RH-8800 Light Microscope. The WS_2 regions are labeled and appear as pale lavender shapes, darker than the background. The exposed Au substrate is a lighter and beige colored region, the slightly darker color compared to the WS_2 mostly outside the red circle is residue from the sample transfer, and Si/SiO_2 regions from fiducial markers appear as sharp, navy blue, geometric shapes. The region where XPS spectra were collected is marked by a red circle with a diameter of 1.93 mm and controlled by the aperture set during the measurement. This region was selected by maximizing the W4f signal in the x, y and z directions.

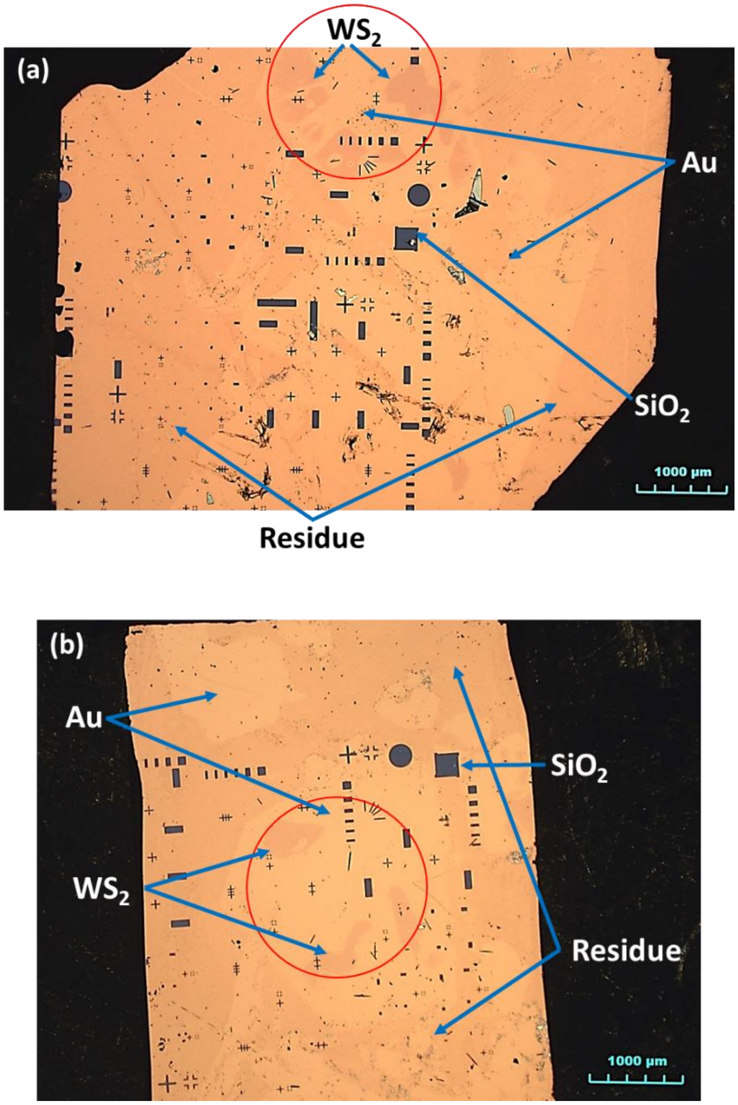

Figure 4.9: Optical Microscopy of (a.) Sample A and (b.) Sample C. The red circle marks the 1.93 mm region which corresponds to the XPS data collection area.

Figure 4.10 is a visual summary of the annealing protocol used for all three samples. Sample A was annealed in n = 17 steps with T_n increasing from 275 to 625 °C in increments of 12.5 to 50 °C with 12.5 °C intervals between 275 and 625 °C. Sample B annealing started at 375 °C and was annealed a total of n = 15 steps increasing from 375 to 625 °C, and with otherwise identical increments to Sample A. Sample C was annealed in n = 6 steps with T_n increasing from 325 to 625 °C in increments of 50 to 100 °C. The heating time to reach the respective temperature t_1 was about 20 min, the isothermal anneal t_2 = 15 min, and cool down t_3 is about 1 hr. XPS was performed after each annealing step, once the sample cooled to below 100 °C.

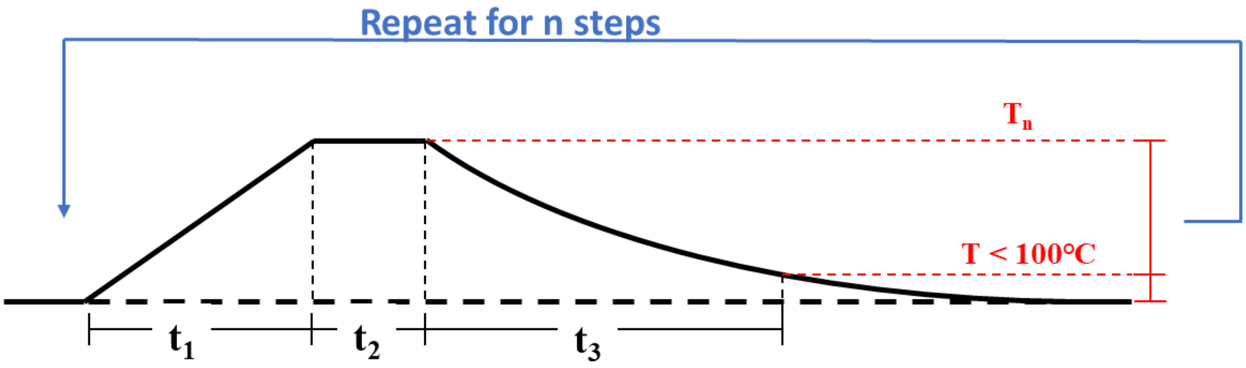

Figure 4.10: Annealing protocol for all samples and n is the number of annealing steps, T_n is the annealing temperature at a particular annealing step, t_1 is the heating ramp up time, t_2 is isothermal annealing time T_n and t_3 is the time for the sample to cool below 100°C followed by XPS analysis.

Figure 4.11 compares the cumulative annealing time for samples A & C across the entire annealing process. The cumulative annealing time determines the overall thermal load. At lower temperatures, the thermal loads are similar for samples A and C, but they begin to diverge between 375-450 °C. At temperatures >450 °C, the difference in thermal load is quite significant and is discussed in the main body of the manuscript.

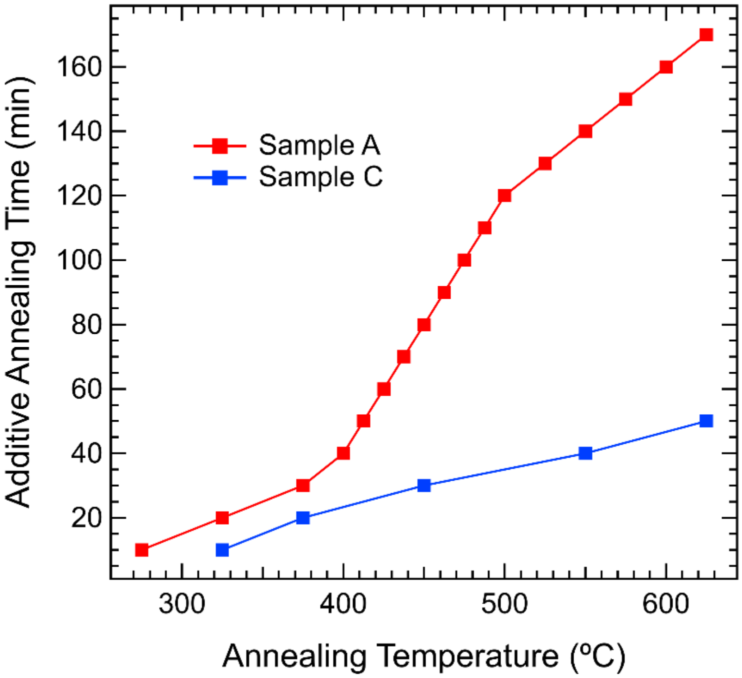

Figure 4.11: Cumulative annealing time for samples A & C as a function of annealing temperature.

Figure 4.12 summarized the complete set of core level spectra, which are vertically offset for each temperature. This dataset correspond to the small temperature increment annealing experiment - sample A. The spectra included in the main body of this publication are marked in red. The very small increments (12.5-50 °C) allow us to pinpoint more precise reaction initiation temperatures.

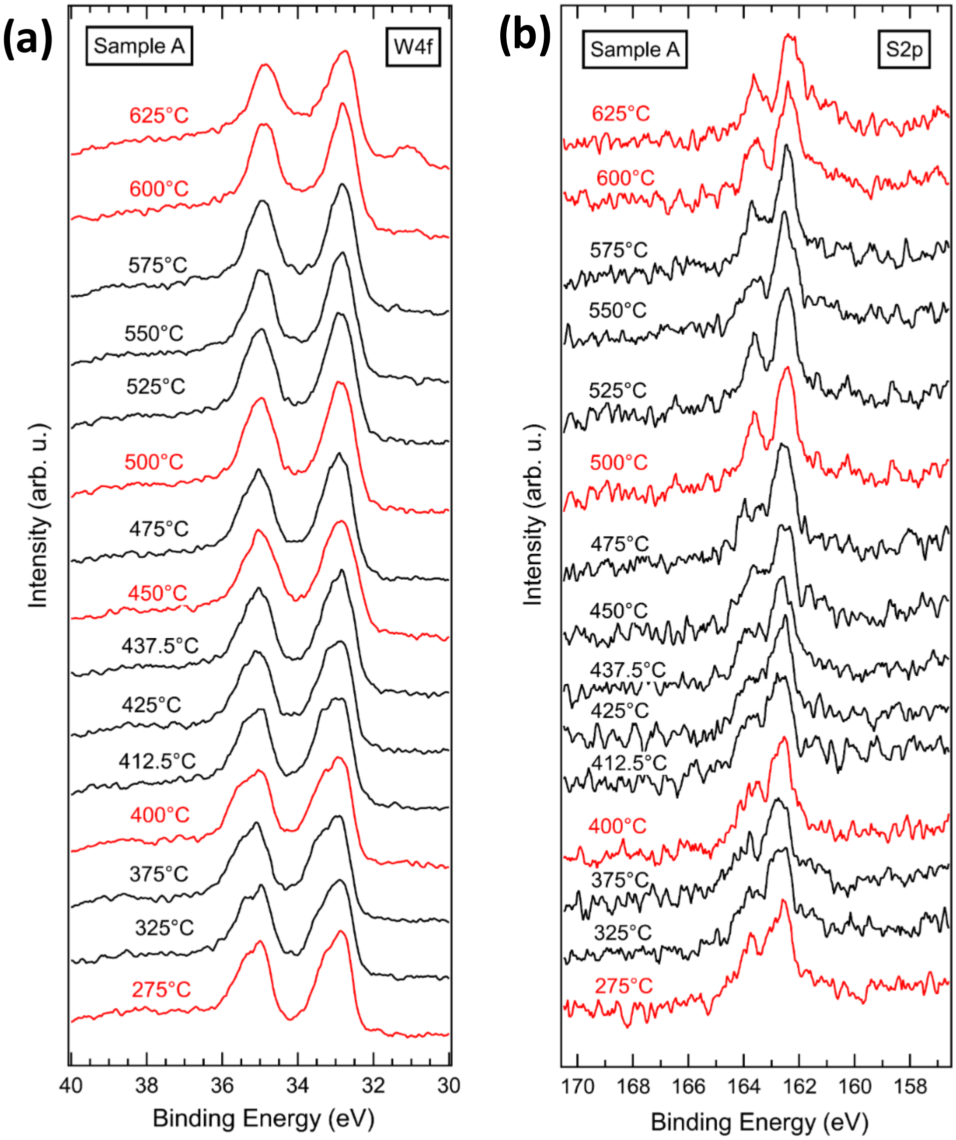

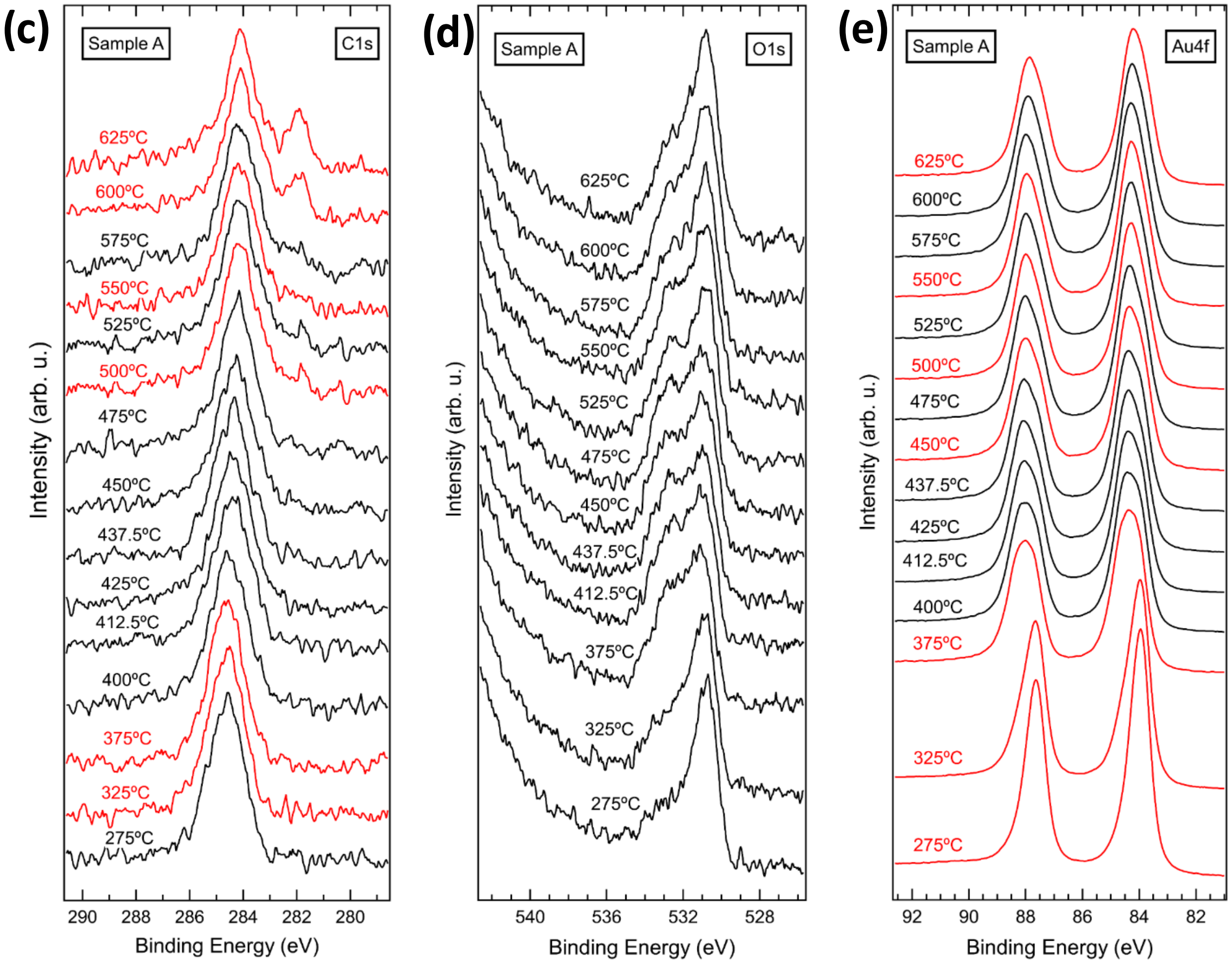

Figure 4.12: All core level spectra for Sample A: (a) W4f (b) S2p (c) C1s (d) O1s, and (e) Au4f, with the red spectra marking those included in previous figures.

Figure 4.13 illustrates the Ti3p core level as a function of annealing temperature for Sample B. The Ti3p peak overlaps with the W4f spectra and, therefore impacts the W4f core level analysis. However, since sample B does not include any WS_2 it is possible in this case to assess the Ti reactions and get an idea about the peak shape hiding underneath the W4f core level.

The Ti3p peak maximum is positioned at ~38 eV, which is characteristic for TiO_2, and for higher annealing temperatures an additional contribution around 35 eV starts to dominate the spectra, and can be attributed to sub-stoichiometric TiO_{2-x}. The reduction of Ti occurs because more Ti reaches the surface by diffusion, but the oxygen inventory at the surface is limited under UHV conditions. This reduction is also seen in the Ti2p core level included in Section 4.3 Figure 4.6.

The dashed gray lines included in Figure 4.13 indicate the positions of the W4f core level boundaries and illustrate the impact of the Ti3p core level on the analysis of the W4f core levels. The energy window around 42 eV mostly impacts the background on the high energy side of W4f, and overlaps with the high binding energy side of the $W4f_{5/2}$ peak, while at higher temperatures the $W4_{7/2}$ peak shape is also impacted. Clearly, if enough titanium is present, the Ti3p core level will contribute to the spectra collected in the W4f binding energy range.

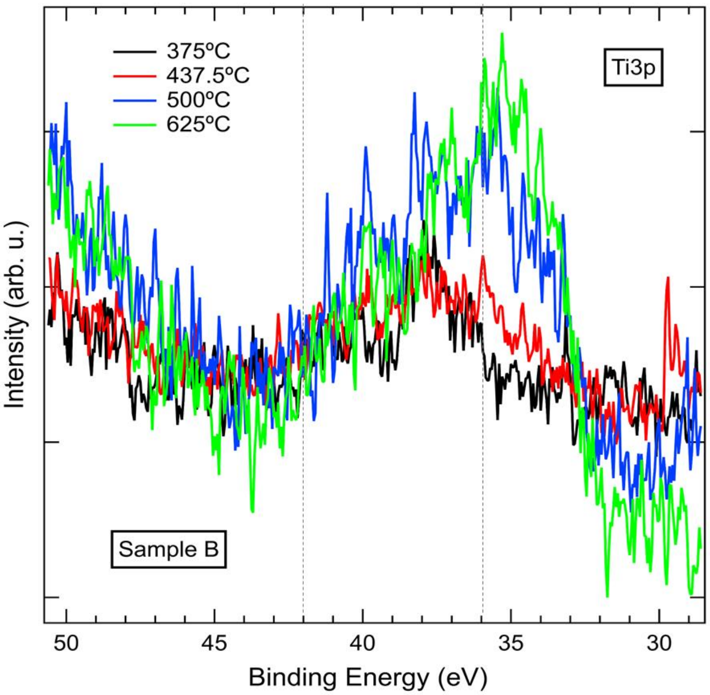

Figure 4.13 Ti3p core level spectra of Sample B for selected annealing temperatures.

4.5 Discussion

The reactions between the Ti-Au substrate sandwich, the WS_2 layer, and the residue are complex and lead to a heterogeneous surface, whose chemical composition has the potential to significantly modify the behavior of any device structure. The XPS analysis of the chemical reactions presented here offers insight into the processes at the surface, and in the near-surface region but integrates over an area where WS_2 contributions are maximized. The presence of significant amounts of carbon and oxygen indicate that at least some of the residue has migrated across the surface from closely adjacent areas. Adventitious carbon as well as some W-oxide, which has formed during the exposure of the sample to air, participate in the surface reactions. However, the most reactive element in this complex mixture is Ti, which rapidly diffuses from the Si/SiO_2 interface through the Au-layer into the near surface region, where it reacts with all components of the system.

The Au-Ti alloy formation is seen for all samples, albeit to a lesser degree in sample B where Ti is consumed more rapidly due to the higher relative oxygen concentration and therefore removed from the near-surface alloy. Sample B does not include WS_2 and the oxygen can only be supplied from the residue layer. In addition, the C/O ratios in all samples are similar pointing to the residue itself as the primary source of oxygen and carbon. Ti diffusion to the surface starts at relatively low temperatures (<275 ºC) and $AuTi_2$ alloy formation is followed by de-alloying at T>500 ºC when Ti is depleted by reactions with C and O. Ti-carbide starts to form at about the same temperature opening an additional reaction channel. At T>600 ºC even WS_2 reacts with Ti and a small contribution from Ti_2S_3 can be seen in the S2p peak. Rapid diffusion of Ti through the noble metal thin film substrate has also been observed for Pt, where it significantly modified the subsequent oxide growth to the detriment of the desired properties.[90,91] The polycrystalline nature of the noble metal film provides rapid diffusion paths, and the highly reactive Ti will dominate the surface chemical reactions.

On the other hand, the WS_2 layer is relatively stable but shows the commonly observed loss of S and consequently p-type doping when annealed above about 400ºC. The presence of a significant amount of W-oxide was surprising, and likely due to oxidation of defects, or at the perimeter of the WS_2 islands.[92] Despite the presence of residue the formation of W-carbide is not observed, and the carbidic peak in the C1s spectra is caused by stoichiometric and sub-stoichiometric Ti-carbide. The residue itself undergoes graphitization, which is initiated at about 400 ºC and progresses continuously for higher temperatures. WS_2 presents two contributions as seen in the W4f spectra, and we suspect that this is due to variations in defect concentrations, or presence of residue on top of the individual WS_2 islands and flakes.

The sequence of solid state reactions as a function of temperature is rather similar for all samples considered here but differs in magnitude. Diffusion of Ti through the noble metal layer is seen in all samples, and Ti as a highly reactive element drives many of the solid state reactions which play out at the surface. The presence of O, C containing reactants such as residue, or traces of adventitious carbon leads to a rapid reaction with Ti, and limits the formation of Au-Ti alloys, but also inhibits desorption of residue from the surface by the formation of rather stable oxide and carbide compounds. It is not known whether Ti reacts with defects in the WS_2 layer, but it cannot be excluded. Despite the relative stability of WS_2 these changes in surface and alloy composition can severely inhibit the reliable and reproducible formation of contacts, or deposition of gate oxides making it rather challenging to build and test devices and sensors. Ideally Ti should be eliminated as a sticking agent for any fabrication or device process where T can exceed ambient conditions. Eliminating Ti will extend the thermal stability range with respect to solid state chemical reaction to about 400 ºC which marks the onset of significant S loss. In addition, eliminating Ti will also make it feasible to remove at least some of the residue by a low temperature annealing procedure rather than initiating a reaction.

4.6 Conclusion

Thermal annealing of monolayer WS_2 on Au/Ti under UHV initiates a range of reactions that give insight into the thermal stability of this material system. The XPS results presented here were collected in a stepwise fashion to determine the initiation temperature of each reaction. The temperature step size is varied to examine the effect of thermal load. An additional sample is examined of Au/Ti without the WS_2 monolayer present, to determine the impact of WS_2 on the reaction processes. The results of all three experiments are compared and contrasted here.

It is found that the same sets of reactions occur on all three samples, but some of these reactions initiate at different temperatures and proceed to different extents. In all three samples, the Ti diffuses up the Au nanograins, causing a variety of surface reactions. Most of the Ti react with the oxygen left behind by the polymer residue or alloys with the Au, but, at higher temperatures, it also reacts with carbon and sulfur. Clearly, Ti is not stable in this system, and we recommend it not be used in any device structures that will be annealed >275 ºC. It is suggested that Ti be replaced as the sticking agent for Au. One possible replacement being explored in the Cress group is Chromium. Ti diffusion could also potentially be mitigated by oxidizing the Ti prior to Au deposition (which occurs naturally in many synthesis methods) or by increasing the grain size of the Au layer to decrease potential diffusion pathways.

Despite the reactivity of Ti, the WS_2 is relatively stable. The sulfur only begins to react with Ti ~600ºC, the W oxide is reduced, and W does not form a carbide. The primary reaction involving WS_2 is the sublimation of sulfur which causes p-type doping, and is expected to occur at the temperatures studied here. These reactions offer insight into the stability of WS_2 on Au/Ti for future integration into heterostructure devices.

Chapter 5:

“Data-Driven Assessment of Chemical Vapor Deposition Grown MoS2 Monolayer Thin Films”

Anna Costine, Prasanna Balachandran, Petra Reinke

My contribution to this work was the construction of the entire database (Section 5.3), which included critical assessment of the literature presented, and assistance with the interpretation of statistical analysis and machine learning results lead and provided by Prof. Balachandran. The manuscript was written collaboratively by all authors, and has been submitted to the Journal of Applied Physics.

5.1 Introduction

It has been a decade since the first publication of a transistor with an MoS_2 channel, which sparked interest in the synthesis and use of transition metal dichalcogenides (TMD) in the single to few layer limit.[93–96] TMDs offer intriguing properties, which include valleytronics, charge density waves, and catalytic activity.[97] The TMD band structure depends strongly on the number of layers, and the band gap increases rapidly when moving from about four to a single layer. The concomittant transition to a direct band gap is coveted for electronic and optical applications. The weak interlayer bonding offers an easy path to produce single layer material by exfoliation, but this method, while suitable for laboratory experimentation, is not scalable. TMD synthesis requires control of the number of layers, quality of the material (such as grain boundaries and defects), orientation with respect to substrate, and composition. Chemical vapor deposition (CVD) that starts from solid state sources and metal-organic chemical vapor deposition (MO-CVD) with metal-organic precursors dominate growth studies.[14,94,96,98–128] In addition to single layer material, the assembly of multilayer heterostructures (2D van-der-Waals crystals)[8] made from TMDs, h-BN, graphene and oxides has garnered increasing attention due to their unique versatility.[14,122,129–138] The ability to grow high quality complex 2D layered structures by sequential deposition remains challenging because each new layer has to be grown under conditions that promote high quality growth but are not detrimental to the first layer.

The outcome and scaling of the growth process are generally difficult and time consuming to develop. This is mainly due to the complex interplay between several physical and chemical processes including precursor sublimation, transport through the gas phase, gas phase chemical reactions, surface adsorption and diffusion, and nucleation and growth on a hot substrate. A critical prerequisite to growing high quality van-der-Waals crystals is the full knowledge of the parameter space, which is challenging to navigate without the integration of physics-guided models and experiments.[139–141] However, it is non-trivial for any modeling effort to map every single experimental condition to the desired growth outcome.

We illustrate here the use of data-driven methods to map the parameter space for the CVD growth of MoS_2 monolayer material using data from the experimental literature. MoS_2 is the material of choice for our work since it offered the largest number of publications on materials synthesis among the TMDs. The CVD growth of MoS_2 dominates the literature because it is relatively easy to set up using a tube furnace and solid state precursors (S, MoO_3) making it uniquely accessible to exploit its properties. There has been a recent surge of interest in the application of machine learning (ML) methods in materials and molecular sciences.[17,18,142–154] These methods have been demonstrated to play an important part in distilling key descriptors that carry the most relevant information, establishing quantitative structure-property relationships, predicting new materials prior to synthesis, serving as a surrogate for high-fidelity physics-based simulations, navigating a vast synthesis search space in an efficient manner, and guiding growth of thin films either autonomously or with a human-in-the-loop. It is envisioned that augmenting the results inferred from ML with targeted new experiments, spectroscopy, microscopy, and/or physics-guided modeling can accelerate the understanding into the nucleation and growth mechanisms of MoS_2 monolayer formation.

Our main objective in this work is to utilize ML methods to identify the boundaries and gaps within the deposition parameter space for TMD materials. This strategy is envisioned to open a path to future "programmable" 2D van-der-Waals crystal synthesis, where the growth conditions are severely restrained by the need to accommodate diverse materials. All aspects of ML learning and outcome are discussed in the main body of the manuscript, while details of data search and curation (including a detailed discussion of statistical learning outcomes, and experimental context) are included in the Supplemental Information. In a meta-study such as this work that uses heterogeneous data from a wide range of sources, it is critical to assess the validity of the collected data and use only those data points that can be compared in a meaningful manner. The statistical analysis can not only provide a prescriptive approach to materials synthesis but should in the future be combined with a detailed mechanistic understanding and modeling of the growth process to open new avenues for materials synthesis. The present manuscript is a starting point and uses MoS_2 grown with CVD as a case study. It is based entirely on the established literature and uses the limited data extracted from MoS_2 growth studies. Unfortunately, it is not common to include failed experiments in a published work, which removes critical information from the record and makes it more challenging to achieve a comprehensive assessment of the deposition parameter space. Ultimately, we would like to link the outcome of the statistical analysis to the underlying atomic scale mechanisms, and achieve predictive capabilities to map out strategies for van-der-Waals crystal growth.[141]

5.2 Methods

The construction of a dataset for analysis of MoS_2 synthesis started with a literature search using Web of Science and Google Scholar in the time window from 2013 to 2017. The synthesis of high quality, larger area material emerges in the literature around 2013 a few years after 2D materials garnered widespread interest.[64,155] The details of the construction of the dataset from the literature are described in the Supplemental Information Sections I-III, and a complete datasheet is included in the Supplemental Material. The methods introduced here can be extended to different materials, a larger number of publication, or can be applied to analyze datasets from a single reactor. The scouring of data is currently done "by hand" but we envision that future work can integrate a more automated approach.[156]

We categorize the dataset into five components (see Figure 5.1): (i) Type of CVD method employed (single-vapor or double-vapor), (ii) Substrates used (mostly SiO_2/Si, some with other substrates among them Graphene, Quartz, and h-BN), (iii) Growth parameters (growth temperature at substrate, growth pressure, growth time), (iv) Precursor characteristics - Molybdenum (Mo) and Sulfur (S) source and precursor temperature, and (v) Characterization data (Raman Spectroscopy and a diverse set of microscopy methods) to qualify whether a specific growth condition has resulted in a Monolayer, Bilayer, Multilayer, or No Layers at all. We limited the precursor type to the most frequently used MoO_3 (powder or films) and S-powders. We also limited the growth method to double-vapor CVD. The input variables considered are temperatures for both Mo- and

S-precursors, highest growth temperature at the substrate, growth time and growth pressure. Our analysis does currently not capture the effect of substrate material on the MoS_2 growth outcome due to the small number of experiments (< 4) for each substrate other than SiO_2/Si. This is a shortcoming of current dataset, and an opportunity for future work. Additional details can be found in Section 5.3.

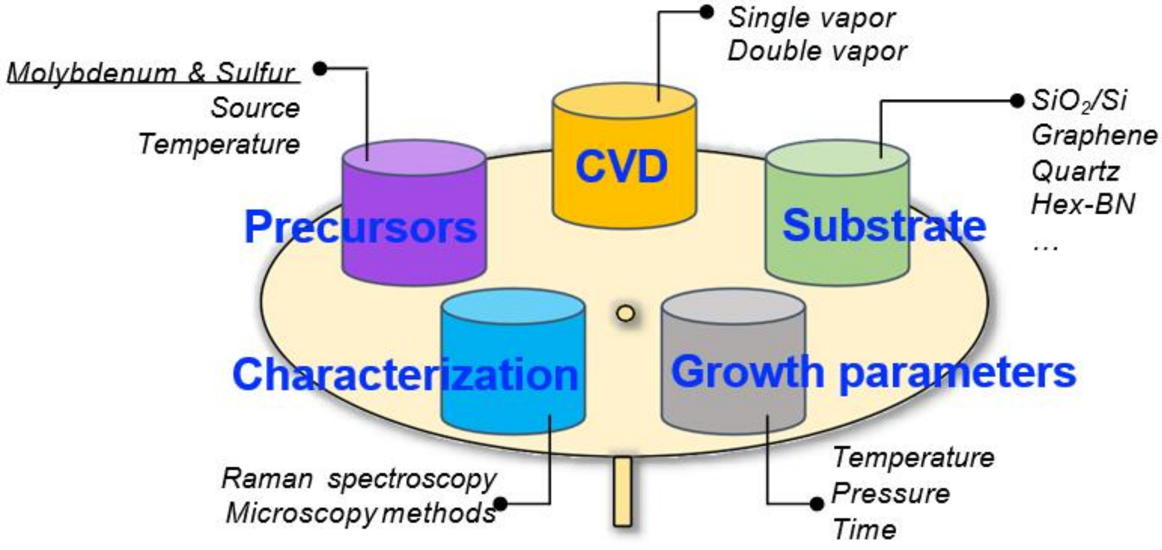

Figure 5.1: A schematic representation of the key descriptors or growth variables in the compiled MoS_2 dataset used for the statistical learning analysis.

The output variable is a binary categorical variable: Monolayer vs Not a Monolayer. The labelling is based on the spectral signature from the Raman spectroscopy data.[126] The difference in wavenumber between the positions of two distinct Raman active peaks, E_{2g}^{1} and A_{1g}, is ≤ 21 cm^{-1} is generally assigned to “Monolayer” material in unstrained layers, and all other spectral signatures are assigned to “Not a Monolayer” and include variable layer thicknesses. We used the author self-identified layer thickness from the respective publication, which is mostly in agreement with the general assignment of layer thickness mentioned above (see Supplemental Information Section III summarizes all Raman data). Overall, there are a total of 65 data points in our dataset; 41 are Monolayers and 24 represent Not a Monolayer thin films.

Several off-the-shelf statistical methods, namely box plots,[157] parallel coordinate plots,[158] metric multidimensional scaling (MDS),[159] and pairwise Pearson correlation analysis[160] are utilized to extract trends and patterns in the compiled MoS_2 growth data. In addition, the random forests method[161,162] is used to establish a quantitative relationship between the growth variables and the outcome (MoS_2 Monolayer vs Not a Monolayer). The choice of random forest method is motivated by the fact that it can shed light on to the important growth variables that govern the formation of MoS_2 monolayers. All calculations were performed in the R statistical environment.[163] In the main manuscript, we focus our discussion on the results from metric MDS and random forests. Results from other methods are presented in the Supplementary Information Section IV.

5.3 Dataset Construction

Figure 5.2 summarizes the data collection strategy in a flow chart, and a description of the decision process is included in the main body of the manuscript. The flowchart visualizes the process of data search, eliminations and additions. It includes the data point and publication number for each step and illustrates the progression of data consolidations. Version 7 is the final dataset which was used for the analysis, and includes references cited here.[14,94,96,98–128] Construction of the data set for statistical analysis requires collection of as many data as possible extracted from the literature, which include comparable information. For example, different synthesis methods might yield the same single layer, high quality material, but the use of different precursors prohibits a direct comparison of the parameter space.

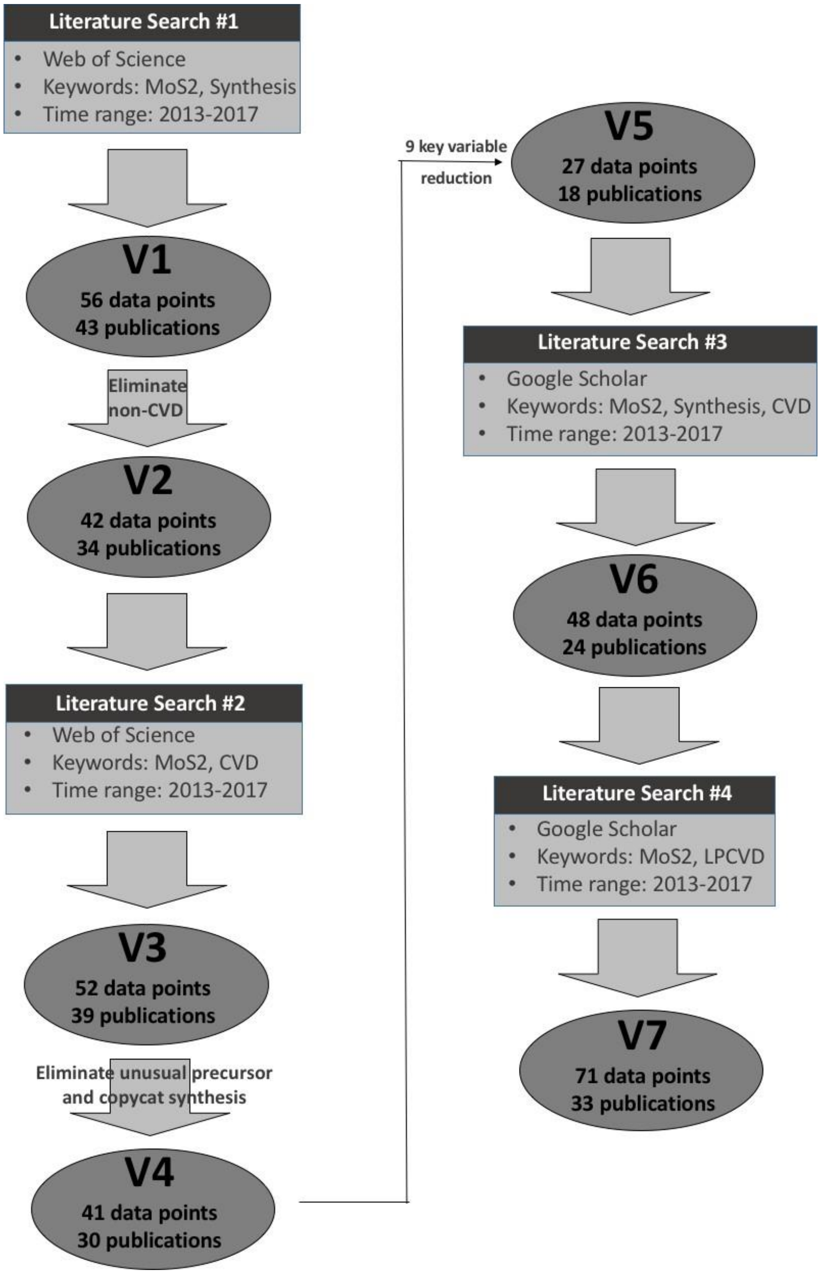

Figure 5.2: Visualization of the data collection strategy.

Search V1 in Figure 5.2 used keywords MoS_2 and synthesis, and search V2 used MoS_2 and CVD in a Boolean search in Web of Science. Search V1 delivered 56 data points from 43 publications. Individual publications can include several data points, hence the publication count is lower than the number of data point. 34 out of the 43 publications used CVD, making it the primary synthesis method and defined the keywords for search V2. Other synthesis methods such as atomic layer deposition (ALD), physical vapor deposition (PVD), MO-CVD (metal organic chemical vapor deposition), and molecular beam epitaxy (MBE) were used infrequently, and did not yield a large enough dataset. The 9 non-CVD method publications were therefore eliminated. Search V3 used CVD as a keyword and delivered an additional set of 5 publications and a final data set of 52 data points. In V4 unusual precursors and "copycat" publications, which used a synthesis process described in a prior publication without variation, were eliminated.

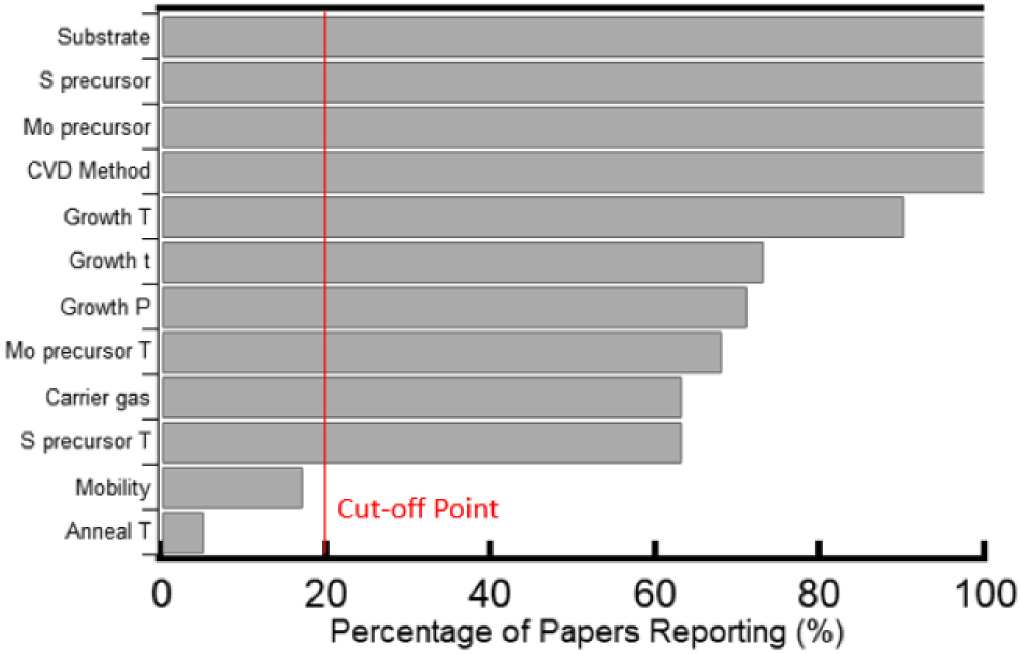

Figure 5.3: Percentage of publications V1 reporting each parameter listed on the y-axis (Substrate, S precursor, Mo precursor, CVD Method, Growth temperature, Growth time, Growth pressure, Mo precursor temperature, Carrier gas, S precursor temperature, Mobility, and Annealing temperature). The cutoff point at 20% is the limit each variable must exceed in order to be included in the analysis. Mobility and annealing temperature failed to exceed this minimum.

In the next step (V5) the growth parameters used most frequently to characterize the CVD process were identified, and selection is primarily determined, and unfortunately also limited, by reporting practices. The following parameters were collected: synthesis method, precursor materials, precursor temperatures, substrate type and temperature, pressure, time, number of layers as determined by Raman spectroscopy, post-growth annealing temperature, and carrier gas flow rate. Figure 5.3 illustrates the frequency of parameter reporting and those reported in less than 20% of publications were excluded. This eliminated post-growth annealing temperature and charge carrier mobility. Additionally, carrier gas was removed from consideration because the flow rates reported are volumetric, but reactor volume is rarely mentioned preventing a meaningful comparison between different set-ups. Publications which used NaCl or nucleation promoters are excluded. Publications with unusual precursor were also exclude: S and MoO_3 in powder form are the predominant precursor materials.

By eliminating infrequent and non-transferrable processing data, the parameter space is reduced to 9 key variables: Mo precursor type, S precursor type, substrate type, growth temperature, Mo precursor temperature, S precursor temperature, growth time, pressure, and the resulting number of layers in the MoS_2 product measured with Raman spectroscopy or self-identified in the publication. Publications, which did not include information about these nine parameters were excluded from further analysis. Search V6 and V7 vary keywords, and search engine for the same time period, and applied the same down selection strategies introduced in V5. Although we collected literature data for both single-vapor and double-vapor CVD growth method, there were only seven data points for the single-vapor CVD. Single and double vapor methods are distinguished by differences in gas phase transport and interdependence of processing variables.

None of the single-vapor CVD experiments resulted in MoS_2 monolayers. Therefore, we do not consider them for statistical analysis.

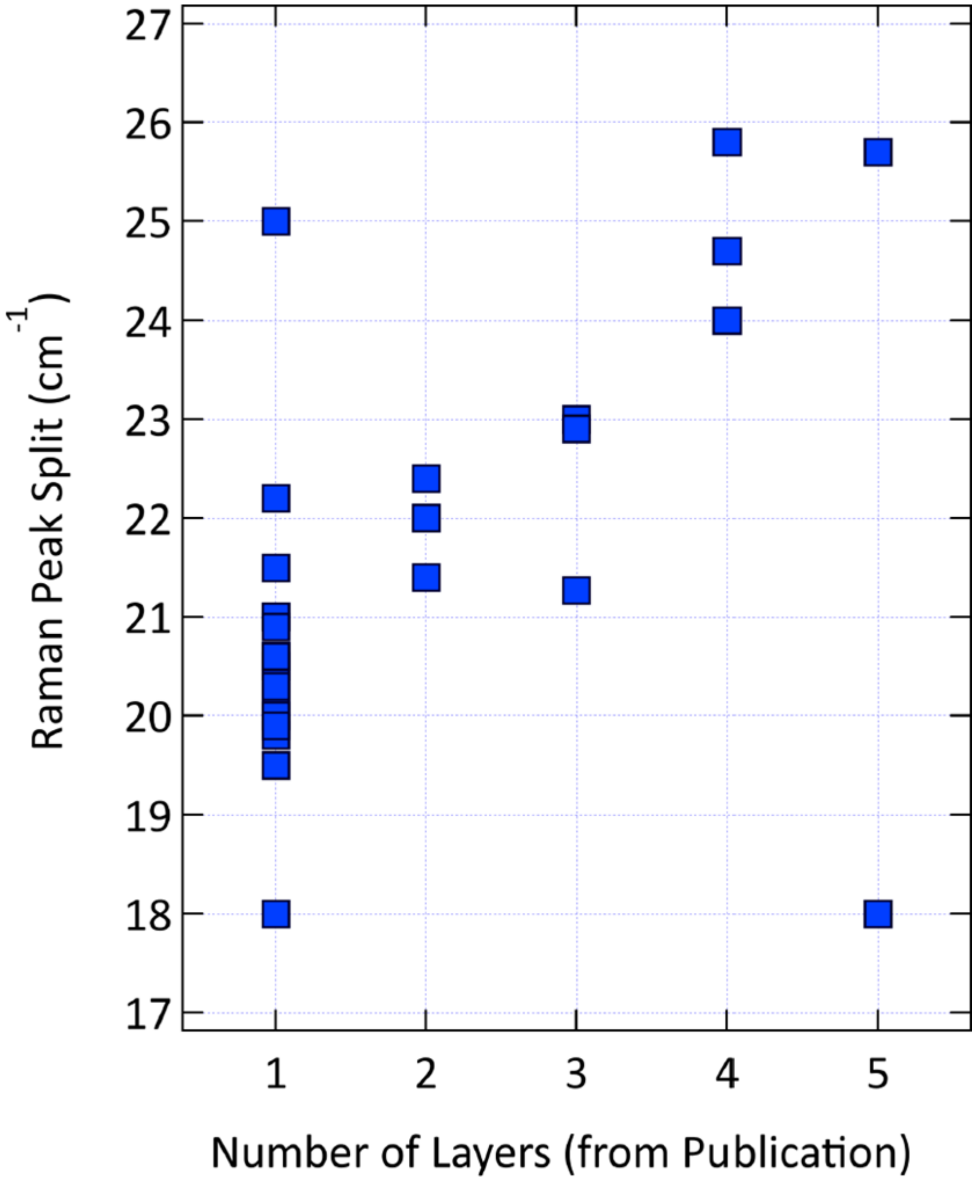

Figure 5.4: Comparison between Raman peak position measured from the spectra displayed in the respective publication, and the number of layers given in the text of the respective publication.

Raman spectroscopy and microscopy methods, which cover length scales between nm and hundreds of µm, are frequently included for material characterization. Raman spectroscopy data were extracted from the publications and are summarized in Figure 5.4. A collection of microscopy images available from the final dataset is shown in Figure 5.5. The shape of MoS_2 crystallites is an important aspect of the growth process, but variations in coverage, growth time, and magnification of microscopy images unfortunately makes this a particularly difficult property to quantify across publications. Other methods of characterization are less common and therefore not suitable for a comparison across data sets.

This down-selection might appear rather harsh and indeed eliminates several interesting studies, which are detailed in their experimental descriptions, but lack one or several pieces of information. For example, many publications report the distance between substrate and precursor, rather than precursor temperatures and had to be excluded. The precursor concentration in the gas phase varies with transport characteristics of the reactor, but variability in reactor geometry prohibits a direct comparison. Ideally the temperature profile in the reactor and precursor temperature should be reported to allow for assessment (and comparison) of precursor concentration gradients. However, of these parameters only precursor temperature is reported frequently and therefore used here.

Some variables, while well reported, were difficult to translate between experiments: Most notable was the growth temperature/ time scheme. Many papers included pre-heating, annealing, and specific ramping speeds/ times that may have some effect on the final product. However, for simplicity, the present analysis only considers the highest temperature reached and the time the sample was held at that temperature. We suspect that reporting practices depend on choice of the experimenter to report parameters which most heavily influence the outcome in a given reactor, but tend to neglect others which are kept constant throughout the work, or are not seen mentioned in the literature.

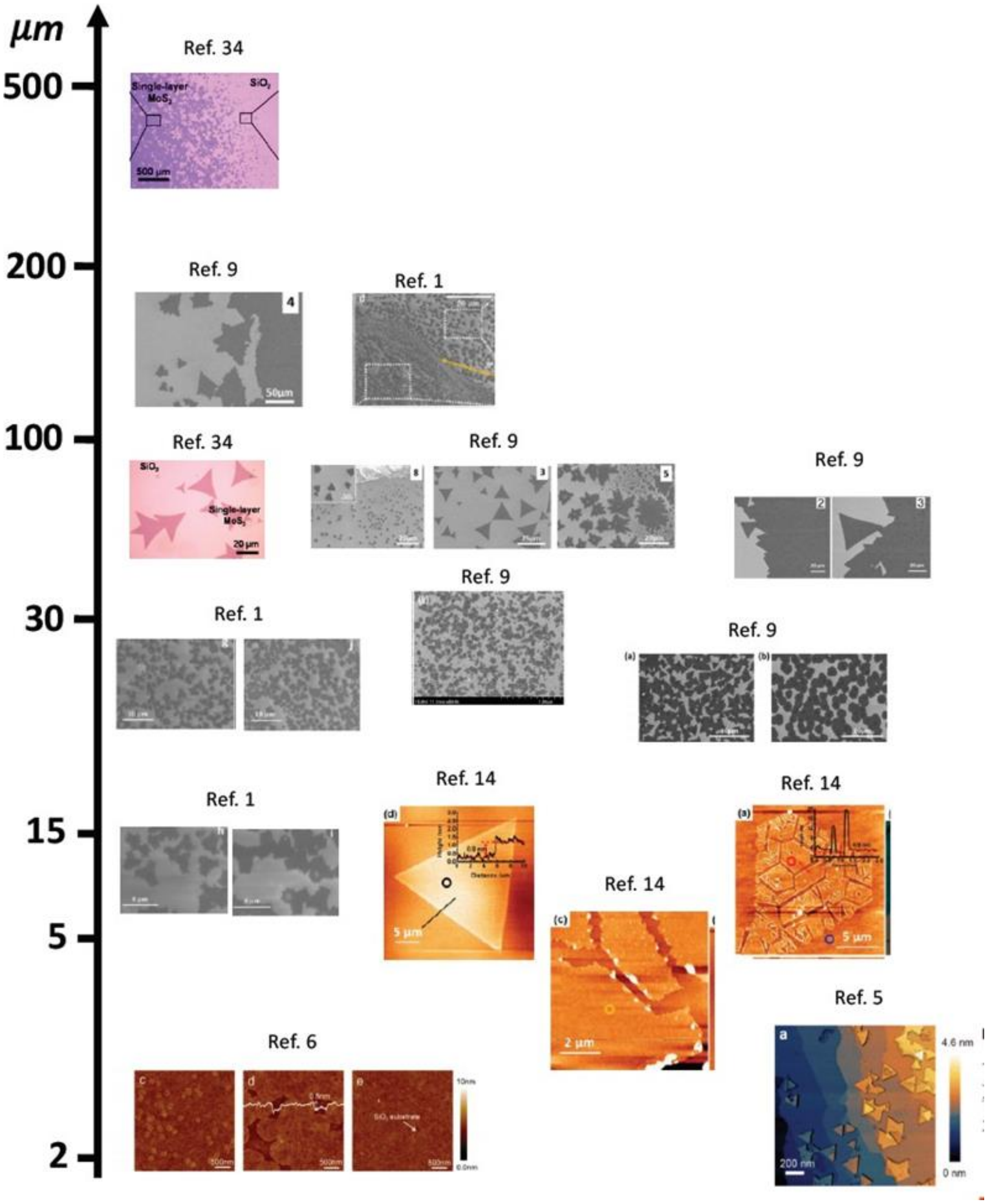

Figure 5.5: Image collection from publications used in this manuscript – Scanning Electron Microscopy images from references1,9 and Atomic Force Microscopy Images from references[100,101,108,128] All images were reproduced with permission from the respective journal.

The definition of Monolayer is deceptively simple but includes near-continuous films, large islands, as well as surfaces populated with a large density of smaller islands, and different island/grain shapes (triangles, stars, hexagons, ribbons, etc.). The definition of a Monolayer is in this work tied to the results of Raman spectroscopy[127,128] and summarized in Figure 5.4.

A selection of microscopy images available for the final dataset V7 is presented in Figure 5.5 to illustrate the breadth of shapes. The MoS_2 islands are difficult to classify in a universal manner owing to variations in coverage, magnification of microscopy images, and the lack of a common, quantitative descriptor for island shapes. Future work will ideally include a systematic, quantitative description of shapes, and cite nuclei densities and size distributions across large ensembles of islands. Unfortunately, microscopy techniques and the corresponding analysis are labor intensive and often only presented for a narrow selection of data which forced us to neglect island/grain shapes, and distributions in the current analysis. The "outcome" used for the development of random forest predictions was therefore restricted to the categorical classification using Monolayer or Not a Monolayer.

Figure A1 in the Appendix summarizes the information for all datasets, which were included in the data analysis. References[14,94,96,98–128] correspond to the Data Set included in the Excel file. Figure 5.3 illustrates the frequency of use in specific growth and outcome parameters assessed after V1. The description given below corresponds to the various columns shown in A1 of the Appendix.

<u>Columns A-E</u>: Manuscript Identifier

<u>Column F:</u> Type of CVD reactor

<u>Columns G-H:</u> Information about precursor type (powder, thin film) and temperature during the growth process

<u>Columns K,L:</u> Substrate type and temperature during the growth process

Columns M-O: growth time and pressure

Column P: Outcome of growth process. “Monolayer” of “Not a Monolayer” is used to encode outcome.

Column Q: Raman spectroscopy (see Figure 5.4) and a wide range of microscopy techniques (see Figure 5.5) were used to assess MoS_2 film thicknesses. Unfortunately Raman peak split values are not reported (or were not measured) in ten of the datasets. The distance between the E_{2g}^{1} and A_{1g} peaks is a common measure of the number of MoS_2 layers, and the distinction between single layer and multilayer is quite reliable but can be ambiguous in the presence of strain. The separation of double, triple and quadruple layer material is much less distinct (see Figure 5.4). This supports use of the binary classifier “Monolayer” and “Not a monolayer.”

5.4 Results from Statistical Learning

In Figure 5.6 and Figure 5.7, the box plots and parallel coordinate plots are shown for the double-vapor CVD method, respectively. The box plot shows that a majority of data points fall within the interquartile range (IQR), except for some specific instances associated with Molybdenum precursor temperature, Sulfur precursor temperature, and growth time. The parallel coordinate plot, on the other hand, identifies sets of specific growth conditions that are unique relative to other common conditions explored in the literature. Two notable exceptions correspond to the work of: (i) Lee et al.,[115] who used an exceptionally high Sulfur precursor temperature (650 ºC) and (ii) Jeon et al.,[110] who chose a long growth time (~240 min.). In addition, the work of Ponomarev et al.[94] and Sharma et al.[117] can also be identified as outliers due to the uncommon choice of growth time relative to other published work. In Table 5.2 in Section 5.6, we list the four outliers identified by box plot and parallel coordinate plot. Thus, without considering the response (i.e., whether a given growth condition resulted in a Monolayer or Not a Monolayer) box plots and parallel coordinate plots provide a succinct summary of the data distribution in our dataset.

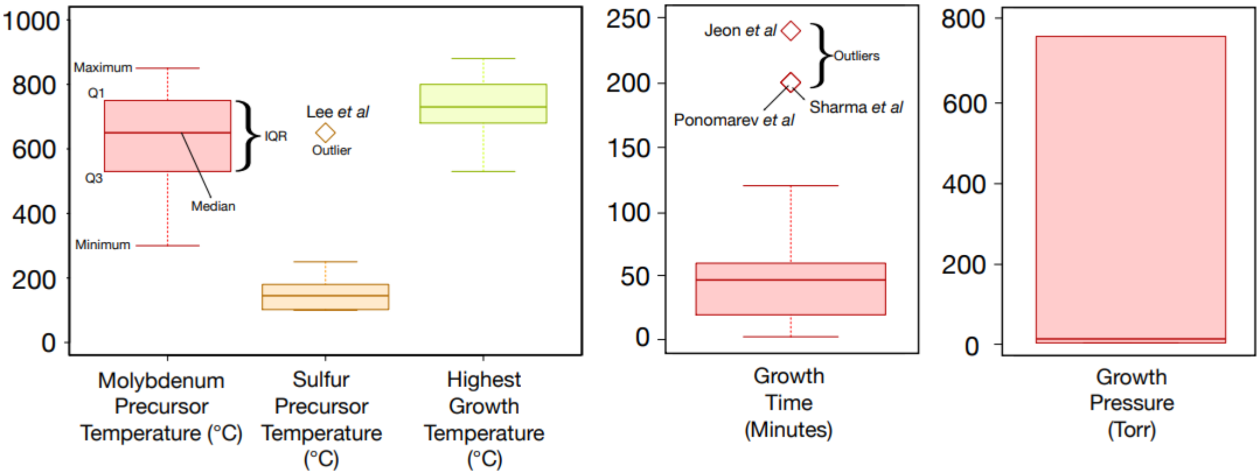

Figure 5.6: Box plot for the five growth variables in the double-vapor CVD MoS2 dataset. In the plot, the median, quartiles (Q1 and Q3), interquartile range (IQR), minimum, maximum, and the outliers are labeled. Some of the prominent outliers are also labeled in the Box plot (eg., Lee et al., Jeon et al., Ponomarev et al., and Sharma et al.).

To gain additional insights, each growth variable is now mathematically constrained with respect to the outcome (i.e., whether a particular experiment had resulted in a MoS_2 Monolayer or Not a Monolayer). The results are visualized in the form of a Boxplot and are shown in Figure 5.8. The dataset contained 64 observations and among them 41 and 23 were characterized (or labeled) as a Monolayer and Not a Monolayer, respectively. All five growth variables show significant overlap in the way the data is distributed, which makes it difficult to uncover relevant trends. The most discernible trend is found in the Mo precursor temperature Figure 5.8a, where it can be inferred that at higher Mo precursor temperatures, bilayer or multilayer MoS_2 thin films were formed. For all other growth parameters the conditions required for Monolayer (and Not a Monolayer) growth are closely matched as seen in the overlap of the respective box plots. For the

Sulfur precursor temperature the monolayer regime starts at lower temperature, and the growth temperature (substrate temperature) extends to higher values for the Not a monolayer regime. This suggests that the concentration of the Mo precursor is the critical parameter to achieve control over the number of layers. Note that the local concentration of the Mo precursor at the substrate is controlled by a complex interplay of reactor geometry, reactant transport and collisions in the gas phase, sublimation temperature at a given pressure, and carrier gas flow rate.

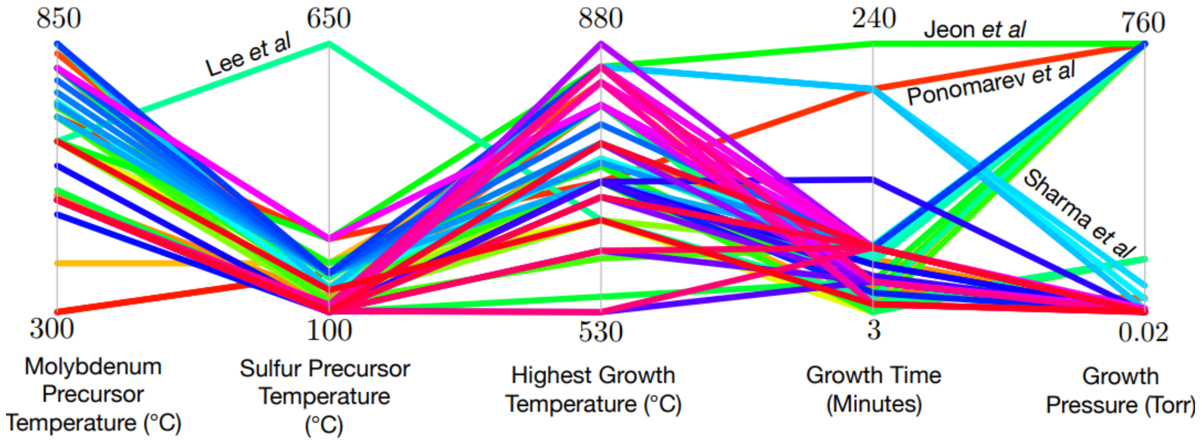

Figure 5.7: Parallel Coordinate Plot for the five growth variables in the double-vapor CVD MoS_2 dataset. Data points that deviate from the general behavior and that are also identified by the Box plot are labeled here (eg., Lee *et al.*, Jeon *et al.*, Ponomarev *et al.*, and Sharma *et al.*).

A non-parametric Mann-Whitney test was performed to determine whether a given growth variable is taken from two independent probability distributions.[128] One of the important characteristics of a Mann-Whitney test is that it makes no assumption on the type of distributions from which the data samples are drawn. When the distributions are different (i.e., p-value < 0.05) then there is a dependence between the growth parameter (eg., Mo precursor temperature) and the growth outcome (Monolayer vs Not a Monolayer). This is a desired result when the target is to deterministically grow MoS_2 monolayers. On the other hand, when the distributions are identical (p-value $\geq$ 0.05), then that specific growth parameter cannot distinguish between the growth outcomes. This is not a desired result for guiding MoS_2 monolayer growth. The result from Mann-Whitney test is shown in Table 5.1. For both Molybdenum precursor temperature and growth time parameters, the p-value is smaller than 0.05 which indicates that the distributions that govern the formation of Monolayers are independent from those that would yield other growth outcomes (eg., bilayer, multilayer etc) for the two parameters. Thus, we infer that only Molybdenum precursor temperature and growth time have non-identical distributions for the two classes (Monolayer vs Not a Monolayer). This result has an important implication, namely that the remaining three growth variables have identical distributions.

In Figure 5.8d, where the growth time is compared between Monolayer and Not a Monolayer, a new data point corresponding to the work of Ji et al. emerges as an outlier.[120] For instance, Ji et al. designed a set of experiments by varying the Mo precursor temperature and growth time that led to Monolayer, Multilayer and No layers. The longest and the shortest growth times resulted in multilayers and monolayers, respectively. However, the intermediate growth times resulted in the formation of no layers in their experiment. On closer examination, we found that in the experiments that led to no layer growth, Ji et al also modified the Mo precursor temperature. This example shows the complexity of MoS_2 growth and the need for a multivariate approach to uncover hidden patterns.

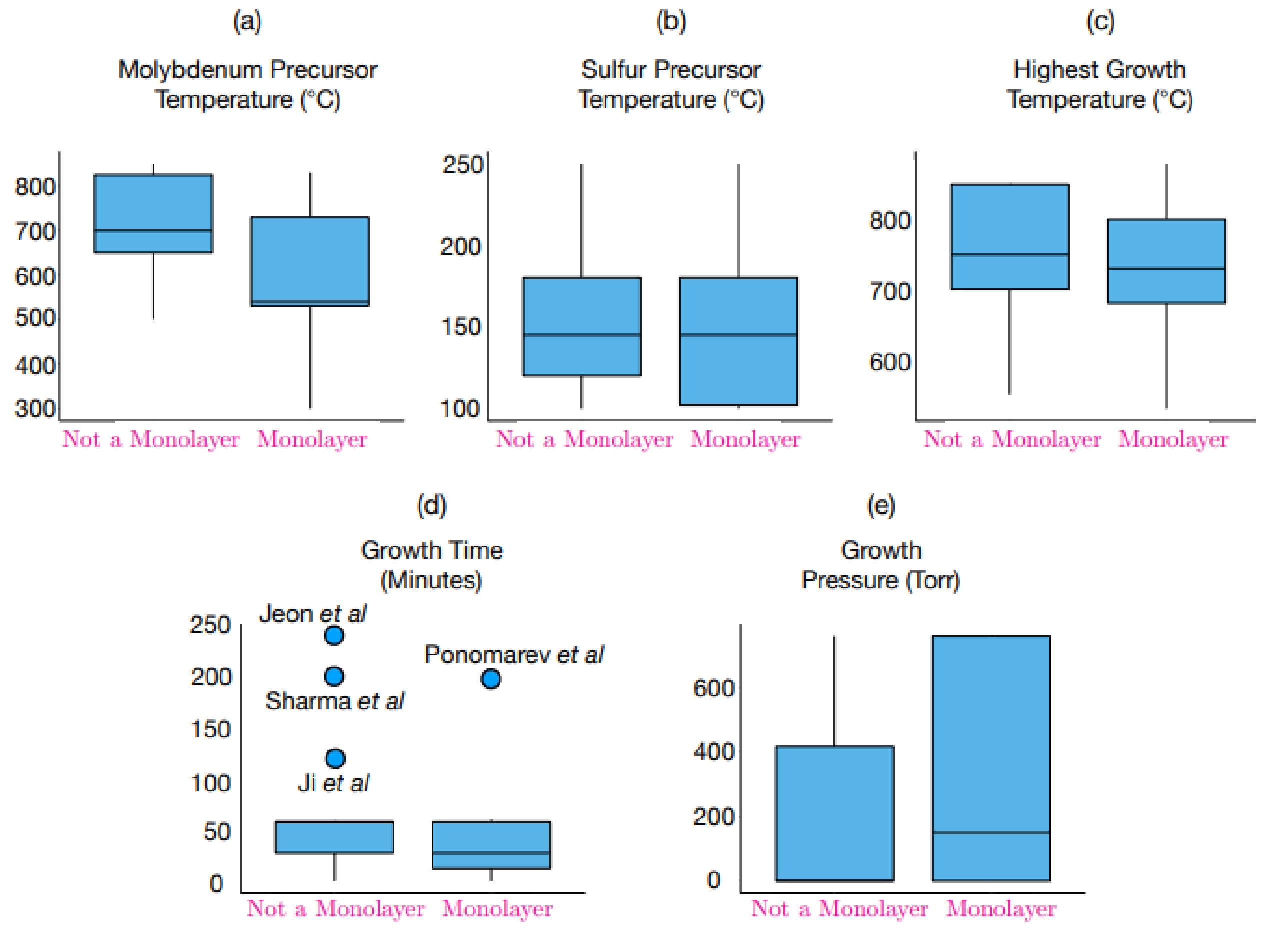

Figure 5.8: A series of boxplots with a class-specific breakdown of each growth variable (a) Mo precursor temperature, (b) S precursor temperature, (c) Highest growth temperature, (d) Growth time, and (e) Growth pressure.

In Figure 5.9a and b, the pairwise statistical correlation analysis for the five growth variables is shown with and without the outlier data point of Lee et al., respectively. In both plots, no strong linear correlation can be found. Further, the removal of Lee et al. data point only affects the correlation structure that pertain to the S precursor temperature (Figure 5.9b). The strongest statistical correlation in our dataset is estimated to be R = +0.65 (R2 = 0.4225) between Sulfur precursor temperature and growth pressure, which is still weak and insufficient to associate any meaningful linear relationship between the two growth parameters.

Table 5.1: The Mann-Whitney test to identify the statistical significance of a given growth variable in distinguishing MoS_2 monolayer from others. A *p*-value of less than 0.05 indicate that the growth variable is statistically significant, suggesting that the particular variable is taken from non-identical distributions for the two classes or outcomes (Monolayer *vs* Not a Monolayer).

Growth variable	*p*-value
Mo precursor temperature (°C)	**0.007**
S precursor temperature (°C)	0.576
Highest growth temperature (°C)	0.468
Growth time (minutes)	**0.031**
Growth pressure (Torr)	0.259

In Figure 5.10, three 2-D scatterplots are shown where the abscissa and the ordinates are deduced from the relative importance outcome of the random forest method. From Figure 5.10a and b, it can be inferred that when the Mo precursor temperature is greater than 800 ^{o}C, it is highly unlikely to obtain a Monolayer, and multi-layer material dominates. The same holds true for longer growth times, which allows for nucleation and growth of higher layers, and this is by itself an intuitive outcome. On the other hand, when the Mo precursor temperature is $\leq$ 400 ^{o}C, only MoS_2 monolayer is formed. At other values of Mo precursor temperature, irrespective of the growth pressure or growth time, no discernible trend emerges. In terms of growth pressure, most of the experiments were performed either at low or high values which is clearly seen in the parallel coordinate plot shown in Figure 5.7. There is a gap between 200 Torr and 760 Torr (1 atm pressure), where relatively few experimental data exists. In the low growth pressure regime, a majority of the experiments were performed at pressure values less than 1 Torr. Growth pressure can be challenging (and expensive) to control in a CVD system, but it is a critical parameter in adjusting the partial pressure of the precursor material, which is controlled by sublimation.

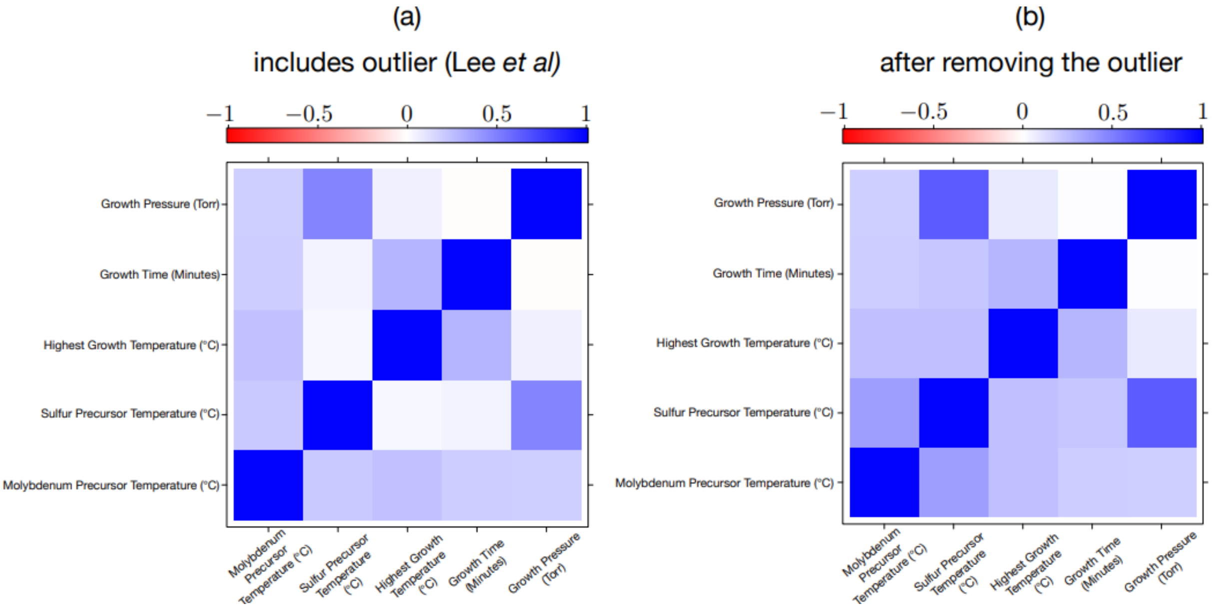

Figure 5.9: Pair-wise statistical correlation analysis of the five growth variables in a double-vapor CVD method. Dark blue and dark red color represent positive and negative correlation, respectively.

One of the implications of our work is the rapid identification of the promising CVD growth conditions that favor MoS_2 monolayer formation by eliminating a vast parameter space that will not yield the desired result. This outcome has the potential to affect both physics-based simulations and experiments. For instance, in the case of physics-based simulations, the insights can serve as a starting point for exploring mechanistic thermodynamic and kinetic models[8] that have been shown to be predictive of specific geometric shape, size, and aspect ratio from triangular to hexagonal growth as a function of the CVD growth parameters. Simulations that leverage the mechanistic models focus on well-defined growth conditions to predict the morphology and our work can provide a rational basis for informing those conditions. On the other hand, the insights uncovered can optimally guide new experiments towards promising regions in the vast parameter space that will enable one to rapidly establish the phase boundaries (eg., Monolayer vs Not a Monolayer) and minimize redundant experiments, thus saving both time and cost.

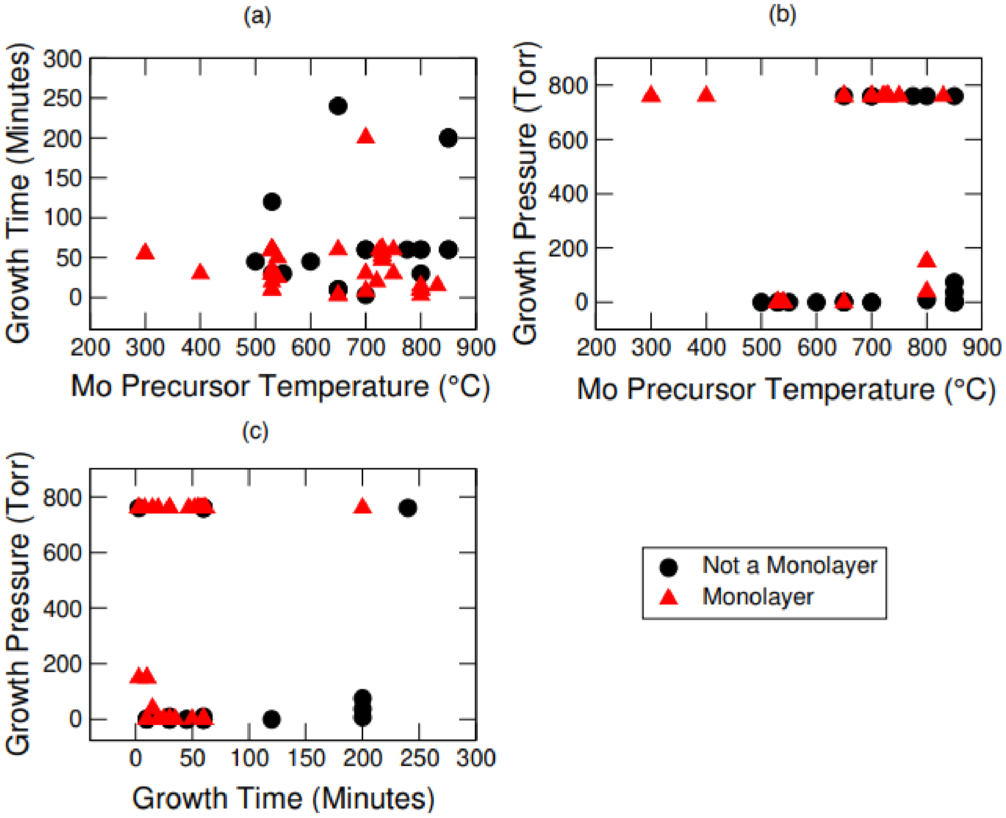

Figure 5.10: Scatterplots between (a) Mo precursor temperature *vs Growth* time, (b) Mo precursor temperature *vs* Growth pressure, and (c) Growth time *vs* Growth pressure. The three growth variables were identified as important by the random forest method. Red filled triangle and black filled dots represent experiments that have led to successful MoS_2 Monolayer growth and that have not, respectively

5.5 Discussion of Statistical Learning

The work described in the previous sections is a first step to the quantitative assessment and predictions of growth outcome for a complex process. The prediction accuracies clearly depends on the quality of the input, which is difficult to guarantee using solely literature data as can be seen from the detailed description of the selection process. Ideally the input data are derived from one CVD reactor which removes many of the ambiguities introduced by the use of literature data. We are aware that most research groups have a much larger (unpublished) databases from their experimental work, which will allow for fine-grained definitions of growth parameters and outcome. In addition to the commonly reported Raman and microscopy information, data on coverage, island density, island size distributions, and island shape would be excellent outcome descriptors which deepen the mechanistic understanding. The statistical and machine learning analysis presented in this publication can easily be extended to include a larger set of parameters, including growth parameters and outcome information.

Even with the highly inclusive outcome definitions, a few publications distinguished themselves as being particularly far outside the parameter space.[94,107,112,114] These publications were identified as outliers during the analysis and will be discussed in detail here. Only one of these outliers (Lee et al.) is far enough outside of the parameter space that it was eliminated from the dataset as described in the Results section. The justification for elimination is two-fold: uncertainty in the data point's accuracy and the inability to define the parameter space around it. As can be seen in Figure 5.11 of Section 5.6, Lee et al. lies well outside of the data structure, and, when removed (Figure 5.11b of Section 5.6), the data structure shows little change. The question of accuracy pertains to whether the information reported by Lee et al. is compatible with our data collection technique, and whether fundamental differences in the growth method make it incompatible with the current dataset.

Lee et al. report a furnace temperature of 650 ºC and show schematically that the substrate and both precursors are positioned close to each other in the center of the furnace.[112] Reporting furnace temperature instead of substrate and Mo precursor temperature when they are centered in the furnace is quite common. Sulfur, on the other hand, is usually positioned at some distance from the furnace center and the temperature is measured separately. As a result, the value reported for the furnace temperature was taken as the temperature of the substrate and both precursors. It is unlikely that sulfur reached this temperature, however, because its evaporation temperature at the operating pressure (760 Torr) is 445 ºC.[129] Thus, leading to a rapid loss of S from the furnace center and possibly recondensation somewhere on the furnace walls. Therefore, the S precursor temperature is unknown, and a temperature for the S precursor is not a reliable value. Since the S precursor temperature is a variable required for our analysis, this data point is not informative. Additionally, the results shown by Lee et al. are consistent with what is expected for CVD performed in an excess of S. With an excess of Sulfur, the S-rich edges will grow faster than the Mo-rich edges,[104] which leads to the hyperbolic triangle shape, which is seen in Lee et al.'s study.

There are a few additional outliers which we decided to include in the entirety of the analysis. Based off their smaller level of variation and careful overview of the publication source, they remained in the data set to maximize inclusivity. These publications were all identified as outliers because of their unusually long growth times as seen in Figure 5.6, although there is a range of possible explanations for this choice in a given experiment. One publication, Ponomarev et al., used an unconventional heating scheme, which involved unusually slow ramping and cooling which made the exact growth time difficult to estimate and was therefore not fully compatible with our data collecting methods.[94] In other cases, it is likely that the longer growth time simply lead to a much thicker layer of MoS_2 better described as bulk material. This is the case for Ji et al. who grew a much thicker MoS_2 film than other publications whose outcome is labeled as "multilayer" (Not a Monolayer). The comparison of growth times is therefore not valid anymore and the boxplot in Figure 5.6 correctly identifies it as an outlier.[120] Sharma et al.[117] and Jeon et al.[110] do not report a layer number, which makes it difficult to judge if the same argument applies as for Ji et al.[120] In the case of Jeon et al. the use of an unusual substrate, carbon nanotubes bundles on SiO_2, might account for the deviation from the overall parameter space.[107] It is, however, nonetheless prudent to include these data points in the analysis because their somewhat unusual synthesis features position them at the edge of the parameter space but not as far outside as the work by Lee et al.[115]

5.6 Results from Machine Learning

In Figure 5.11 the results from the unsupervised metric MDS analysis are shown. The input to MDS is a five-dimensional data matrix that spans all five growth variables: Mo precursor temperature, S precursor temperature, highest growth temperature, growth time, and growth pressure. The MDS method reduces the dimensionality of the data to two under the constraint that the nearest-neighbor distances between data points are preserved. The Monolayer (filled red triangles) vs Not a Monolayer (filled black circles) data points are labeled only for visualization purposes.

The main difference between Figure 5.11a and Figure 5.11b is the appearance of an outlier data point corresponding to the work of Lee et al.[115] which was removed from the dataset in Figure 2b incurring only marginal changes. In Figure 5.11b a few more data points display a unique character and are positioned slightly outside the main data agglomeration and are marked in the graph. These points correspond to the work of Jeon et al.[110], Ponomarev et al.[94], and Sharma et al.[117] and Boxplots and Parallel coordinate plots also identify them as outliers in the dataset (see

Section 5.4 Figure 5.7 and 5.8). The growth conditions are given in Table 5.2 and show unusual values for S-precursor temperature, growth pressure and substrate materials. Substrate choice does not, as a rule, cause outliers and other experiments with non-SiO_2/Si substrates are positioned well within the center of the data cluster. From visual inspection of both Figure 5.11a and Figure 5.11b, no discernible "boundary" distinguishes between the outcome of MoS_2 monolayers from those that do not form monolayers. Thus, the MDS analysis motivates the use of supervised machine learning methods to uncover a relationship between the growth variables and the outcome of monolayer growth.

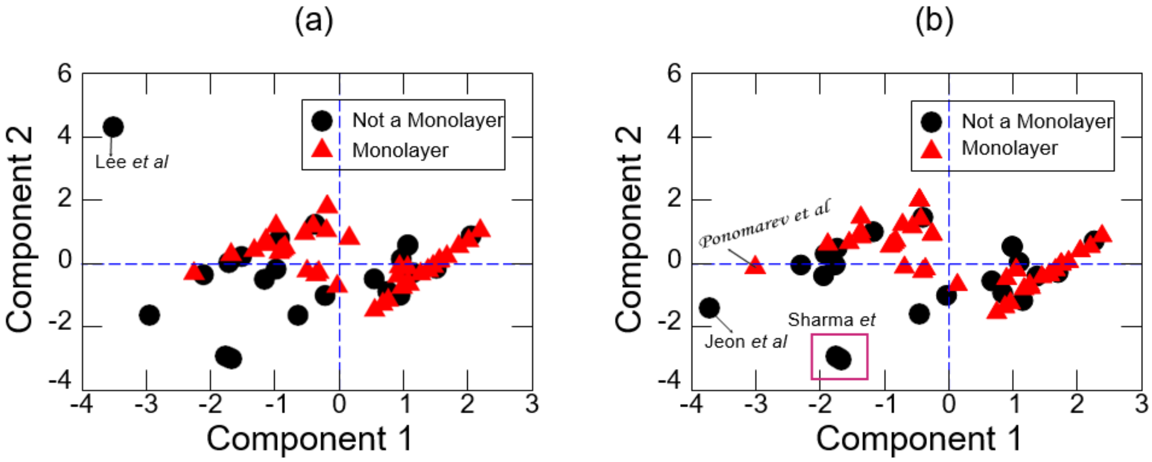

Figure 5.11: Two-dimensional (2-D) plots (Component 1 vs Component 2) from metric multidimensional scaling (MDS) analysis that (a) includes the outlier (Lee et al.[115]) and (b) after removing the outlier. Black filled dots represent growth conditions that did not result in a Monolayer and red filled triangles represent growth conditions that resulted in a Monolayer growth. Also highlighted are the data points that were identified as outliers in the Box plot and parallel coordinate plot (Jeon et al.,[110] Ponomarev et al.[94] and Sharma et al.[117]), which are shown in the Figures 5.6 and 5.7 of Section 5.4. It can be inferred from (b) that the removal of Lee et al. data point only changed the data structure marginally.

Table 5.2: List of outliers identified by the statistical methods in the MoS_2 growth dataset. The key growth variable that lead to the respective data point to be identified as an outlier (on the basis of metric MDS, box plot and parallel coordinate plot) is marked in bold face font. Lee et al.[115] and Sharma et al.[117] use SiO_2/Si as the substrate material. Jeon et al.[110] and Ponomarev et al.[94] use carbon nanotubes on SiO_2/Si and sapphire as substrate, respectively, for MoS_2 growth.

Literature	Mo precursor temperature (°C)	S precursor temperature (°C)	Highest growth time (minutes)	Growth pressure (Torr)	Growth temperature (°C)	Outcome
Lee *et al.*	650	**650**	650	15	760	Multilayer
Jeon *et al.*	650	250	850	**240**	760	Multilayer
Ponomarev *et al.*	700	250	700	**200**	760	Monolayer
Sharma *et al.*	850	145	850	**200**	37.5	Multilayer/No layer

We use the random forest method for building models from data.[161,162] Random forest is an ensemble-based learning method, where many unbiased or decorrelated models (in the form of unpruned decision trees) are generated from the training data and the final outcome is decided based on aggregating the results from each tree. The process of constructing many models is enabled by the bootstrap sampling method (sampling with replacement).[164] Typically, in each bootstrap training set, about one-third of the samples in the original training data are left out, which is referred to as the out-of-bag (OOB) samples. Random forests are trained from the bootstrap training sets and the trained models are tested on the OOB samples. Since the outcome of each of the OOB samples are known, it is relatively straightforward to assess the model accuracies from the OOB error rate.

Initially, a pre-specified (ntree) number of bootstrap samples are drawn from the original training data. Typically, the value of ntree ranges between 50 and 10,000 trees. Then, for each of the bootstrap samples, a classification tree is grown using a randomly chosen pre-specified number of input features (mtry). The algorithm then selects the best features for splitting at each node from the various random trials. Since ntree is a large number, corresponding number of decision trees are independently grown from the different bootstrap samples of the training set. There are two hyperparameters that must be tuned to balance the tradeoff between accuracy and complexity: ntree and mtry. In this work, we vary ntree from 50 to 10,000 trees, in step of one tree during the training process. Further, for each ntree we vary mtry from two to five (given that we have five growth variables). If more than one ntree − mtry combination gives the same minimum OOB error rate, a random forest with the smallest ntree was chosen as the final model (Occam's razor[165]). Since the final decision is a consensus vote from each tree, one can also associate a probability with each prediction. One of the attractive characteristics of random forests is that it provides a relative importance ranking of an input feature. We assess the relative importance of each feature based on the estimate of the loss in prediction performance when that particular feature is not considered from the bootstrap training set for building the model.

While uncovering feature importance can provide insightful understanding of the data, random forests do not address the question of whether a given input feature is relevant for model building. There is a subtle difference between importance and relevance. For instance, importance indicates the relative impact of each variable in affecting the response. A variable may be least important, but may still be relevant and should not be thrown away. Thus, relevance refer to a more stringent feature selection condition and must augment the importance condition. To this end, we follow the work of Kursa and Rudnicki[166] for finding relevant input variables. The approach involves creating a "shadow descriptor" for each of the input variable whose values are obtained by randomly shuffling the values from the original input variables. Once the shadow descriptors are developed, the random forest classification is performed using the extended dataset (that will now also include the shadow descriptors) and one can calculate the relative importance of all features in the extended dataset. Kursa and Rudnicki note that the importance of a shadow descriptor can be nonzero only due to random fluctuations. Thus, these shadow descriptors will serve as a reference for deciding which input features are relevant.

The random forest method is trained on 64 data points (the work of Lee et al. was not included in the learning). There are 41 and 23 data points that were labeled as a Monolayer and Not a Monolayer, respectively. In total, 39,804 random forest ensemble models were built. The optimized hyperparameter values correspond to ntree = 1573 and mtry = 2, which resulted in the lowest OOB error rate of 17.2% (the accuracy is 82.8%). In the OOB data samples, the random forest correctly classified 37/41 and 16/23 data points as a Monolayer and Not a Monolayer, respectively, and the outcome can be predicted with an accuracy of 82.8%. The top three important growth variables are identified to be Mo precursor temperature, growth pressure, and growth time (in this order). The feature selection algorithm also returned with the result that all five growth variables are relevant for this dataset and the relative importance of all shadow descriptors are below that of the five main input features (see Figure 5.12).

Having built the classification models, the next step is to demonstrate its predictive capability. We constructed a "virtual" dataset of possible experiments subject to the following constraints. We vary only the top two important variables (Mo precursor temperature and Growth pressure) and fix the values for S precursor temperature, highest growth temperature and growth time to the median value in the training set. These choices were motivated by the results shown in Figure 5.12.

A total of 16,872 potential experiments were formulated. The goal is to predict specific conditions that will result in a MoS_2 monolayer growth using the trained random forest models. The results are shown in Figure 5.13, which indicates that there is a large region in the CVD space defined by Growth pressure and Mo precursor temperature, where the probability of growing MoS_2

is > 0.5. Lower Mo precursor temperatures and higher growth pressures tend to favor the formation of Monolayer material. Low probability of growing MoS_2 monolayers is confined to the high Mo precursor temperature and low growth pressure regime (bottom right corner of the plot). In addition, there is also an intermediate growth condition (Mo precursor temperature = 550–800 ºC and growth pressure = 5–30 Torr), where the predicted probability values range between 0.4 and 0.6 for growing MoS_2 monolayers. This specific growth window represent the uncertainty in the random forest models. We recommend more experiments in the vicinity of the uncertain CVD growth space to gain further insights, and to ultimately construct maps that can guide experimentation.

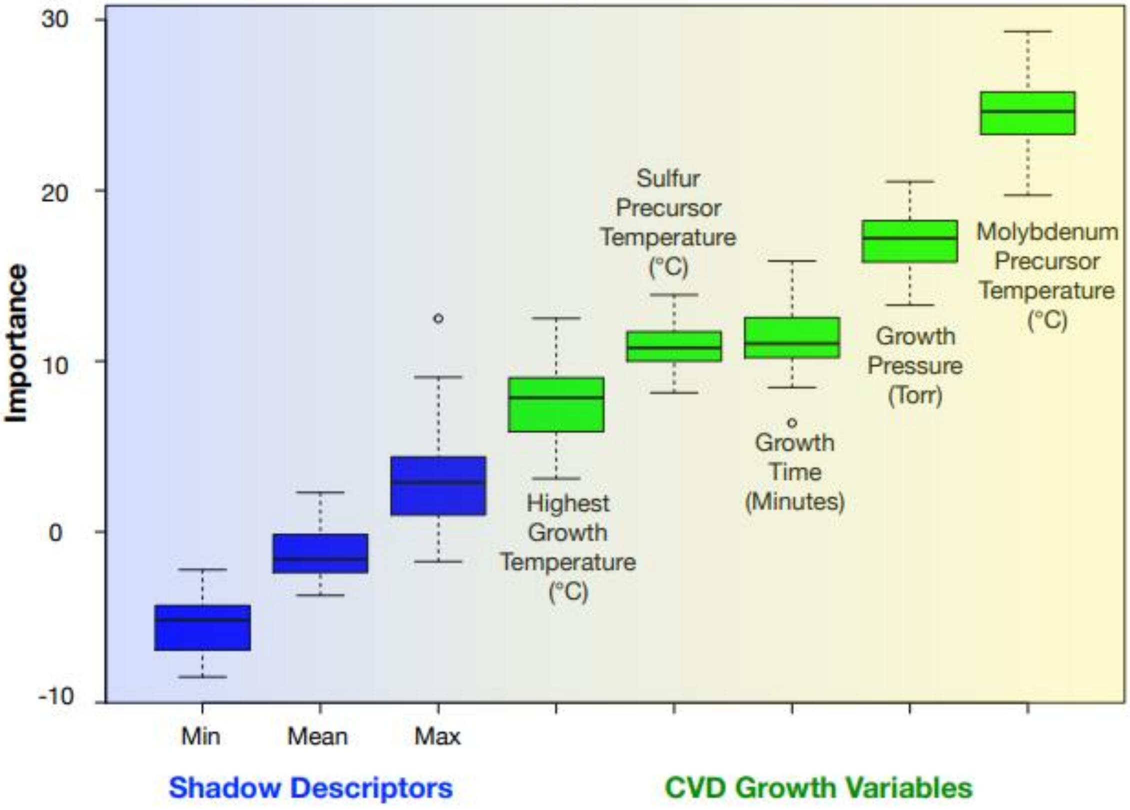

Figure 5.12: Feature importance plot indicating that all five growth variables (green boxes) are relevant relative to the shadow descriptors (blue boxes).

5.7 Discussion of Machine Learning

The results of the data analysis considering response have unveiled a number of synthesis trends leading to ranking of growth parameters in importance as shown in Figure 5.12. The concentration of Mo precursor is dictated by the temperature of the Mo precursor, and the pressure in the reactor, which is a consequence of the physics of the sublimation process. The temperature of the Mo precursor, according to our results, should never be higher than 800 ºC for monolayer growth. A similar temperature cut-off at 775 ºC (at atmospheric pressure) was found experimentally by Zhou et al.[119] The same rationale applies to Sulfur, which explains why the optimal Sulfur precursor temperature for monolayer synthesis is higher at higher growth pressures. Almost all low pressure CVD publications resulting in monolayer material were published by two research groups at the same university, and their synthesis operated overall at lower S- and Mo precursor temperatures.

A systematic study on the impact of pressure on MoS_2 growth by Najmaei et al.[167] was excluded from the analysis because of the use of MoO_3 ribbons as source material, whose sublimation behavior differs from the more commonly used MoO_3 powder. However, this work nonetheless illustrates that variation in pressure leads to a response in MoS_2 deposition outcome (shape, density, number of layers) which is similar in scope to variations seen with temperature. This leads us back to the precursor temperature-pressure map developed in Figure 5.13, which links the two growth parameters in a quantitative, and physically meaningful manner. These result suggests that the influence of operating pressure is strong but currently underutilized. Exploring the temperature-pressure parameter map offers a versatile path to adaption of the growth parameter space.

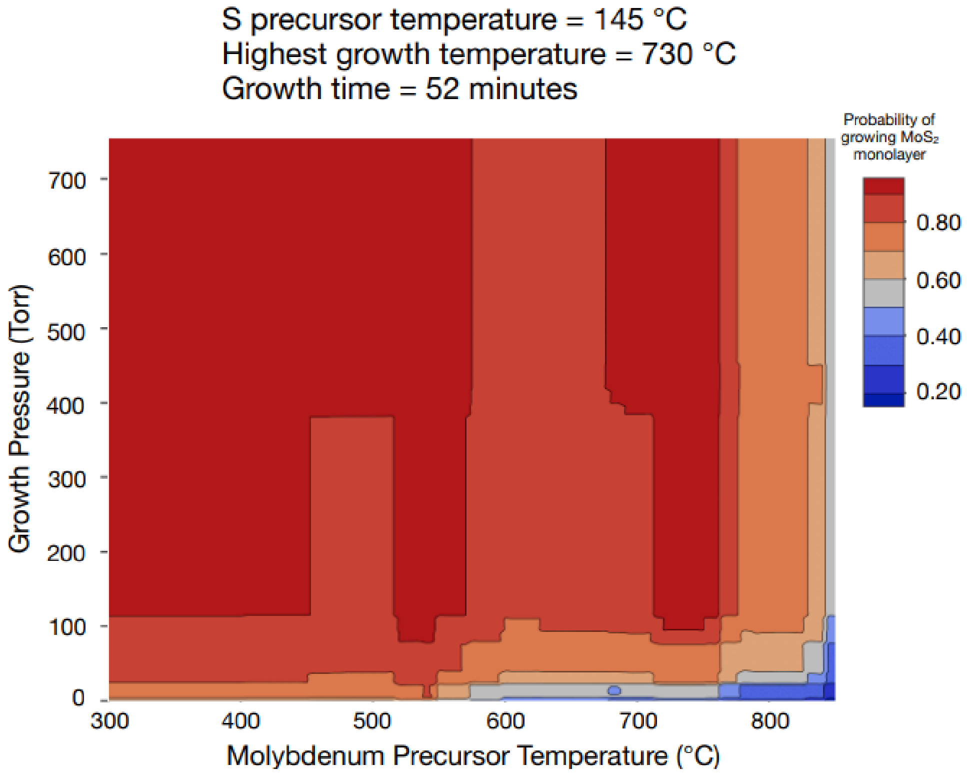

Figure 5.13: Predictions from random forest in terms of the probability of growing MoS_2 monolayers are shown as a contour plot. The S precursor temperature, highest growth temperature, and growth time were held constant at 145 ºC, 730 ºC, and 52 minutes, respectively, which are the median values in the training set. Both, Mo precursor temperature and growth pressure, were allowed to vary in the range shown in the figure. The low probability of MoS_2 monolayer growth is confined to the high Mo precursor temperature and low growth pressure regime.

Although we were able to correlate the results to the plausible mechanisms of nucleation and growth, the small size of the dataset precludes us from making any deterministic conclusions. Further, it can also be seen that the growth parameter space is not fully explored, as evident from Figure 5.13. This poses challenge for any data-driven procedure that is not driven by physical laws because the trained mathematical functions will seek to interpolate based on known data. One of the strategies to overcome this deficiency will be to perform targeted new experiments in the regions where either the experimental data is sparse or where the random forest models are most uncertain. An example for an uncertain data population is the Mo precursor temperature range of

575 to 775 ^{0}C combined with a growth pressure range of 5 to 30 Torr (keeping other parameters constant, including substrates) where the probability of forming a monolayer is between 0.40 to 0.60.

We hypothesize that such experiments will shed key insights in distinguishing growth parameters that will lead to monolayer vs multilayers. Augmenting these results with physics-guided simulations can uncover the elusive mechanistic insights into the nucleation and growth of MoS_2 monolayers. The Mo precursor temperature-growth pressure map shown in Figure 5.13 represents only a snapshot of the current machine learning capabilities. In principle, a large library of similar probability growth maps can be constructed using other parameter values that will be of interest to the broader growth community. Finally, we encourage the community to report more frequently on "failed experiments", i.e., experiments which did not deliver the desired outcome to improve and train machine learning models. Overall this will reduce the number of redundant experiments, advance insight in growth mechanisms, and allow to evaluate and plan growth strategies for complex materials, specifically van-der-Waals crystals.

5.8 Conclusion

Starting from 64 observations of experimental MoS_2 growth data compiled from published literature, we extracted insights into factors that govern the growth of MoS_2 monolayers using CVD method. Our analyses uncovered a wide operating parameter range to grow MoS_2 monolayers (within the scope of our definition of a monolayer). Mo precursor temperature and growth pressure are identified as key factors in distinguishing monolayers from bi- or multilayers. The importance of precursor temperature is widely recognized, while growth pressure is infrequently used to control materials synthesis. Predictions from trained models illustrate how variations in the growth parameters impact the growth of 2D MoS_2 films, which can serve as a useful guide for targeted synthesis and can easily be extended to integrate new datasets.

Chapter 6:

"Synthesis and STM/S Characterization of Ribbon-Silicene on h-MoSi$_2$"

My contributions to this work include synthesis and characterization of the silicene, silicene ribbon, and other surface reconstructions on the silicide surfaces. This work was performed at the Oak Ridge National Laboratory in collaboration with Dr. Zheng Gai at the Center for Nanophase Materials Science. A publication is anticipated in fall 2020.

6.1 Introduction

Silicene is a single layer of Si atoms arranged in a honeycomb lattice, structurally and electronically similar to graphene.[22,168] A range of intriguing properties have been theoretically predicted for silicene[168], which has prompted many experimental studies. One of these is a stronger intrinsic spin-orbit interaction (SOI) than graphene.[169] The SOI induces a bandgap in silicene which has been calculated to be 1.55 meV by Density Functional Theory (DFT).[168] This allows for the quantum spin Hall effect (QHSE) to be explored at experimentally accessible temperatures.[168,170] The buckled structure allows for bandgap tunability.[20,168] Varying a perpendicular electrical and magnetic field has been shown to cause a series of topological phase transitions in silicene.[20] These properties make silicene a promising material for electronic and spintronic devices.[169,170]

The tunable electronic structure arises in silicene because of its buckled structure. Si atoms are not stable in a purely sp^2 configuration and therefore adopt a mixed sp^2/sp^3 type bonding by shifting apart from each other slightly (~0.1 nm or less) in the z direction. A less buckled structure will have more sp^2 type bonding and a more Dirac-like nature (linear E(k) dispersion and high electron mobility).[171] This type of buckling is considered more favorable for potential applications. Experimental realization of low buckled silicene strongly depends on the type of substrate it is synthesized on. The most commonly used substrate for synthesis is Ag (111), but it is discussed controversially due to its similarity with surface alloys.[169,172,173] Silicene has also been synthesized on other substrates including Ir, $IrSi_3$, PbSe and ZrB_2.[171,174–176] In the past few years, more research has been focused on silicene synthesis on more technologically relevant substrates.[21,177] Especially promising are substrates that retain the low buckled structure of silicene and are suitable for device integration.

The work discussed here will add to these efforts to synthesize low buckled silicene on substrates that allow for the Dirac nature to be preserved and measured, which also requires a semiconducting substrate to avoid hybridization between silicene and substrate bands. Hexagonal semiconducting silicides are used as the substrate in the work presented here. These materials offer favorable lattice matching with silicene, and their semiconducting nature should allow for more precise measurements and conservation of the intrinsic electronic structure.[43] The Reinke group has already developed a process to synthesize low-buckled silicene on h-$MoSi_2$ (see Section 2.2.2 Figure 2.5) and determined the range of synthesis condition under which it forms.[47] Through a detailed study of the kinetics of silicene formation, the work presented here will show that a broad range of silicene-related surface structures and nanostructures can be synthesized in the same material system. The most interesting of these surface structures appears as a ribbon-like structure and occurs on h-$MoSi_2$ crystallites, highlighting the diversity of this material as a substrate for silicene synthesis.

The challenge lies in properly characterizing novel surfaces in the diverse metal silicide material system. Previous publications have shown that a range of silicide phases can form, with many unexplored surface geometries.[43] Si is also well known to be easily doped by metals, which causes the surface to reconstruct in a variety of ways, depending on the amount of metal deposited.[178] Additionally, a number of different geometries of self-assembled metal silicide nanowire can be synthesized on Si substrates.[179] The work presented here will focus on the surface structures of flat top h-$MoSi_2$ (0001) crystallites surfaces described in Section 2.2.1.

6.2 Experimental

Two methods for silicide and silicene synthesis were performed. For both methods, h-$MoSi_2$ crystallites are grown by depositing Mo onto a Si(001)2×1 reconstructed surface, followed by annealing. The methods differ in Si cleaning method (flash annealing to ~1200 ºC or hydrogen termination) and in whether the sample is exposed to ambient conditions. The amount of Mo deposited (0.3 nm-18 nm) and annealing temperature (700-1000°C) were used for both synthesis methods.

6.2.1 Method 1

The first method (Figure 6.1) was developed using the VT-STM at UVa in prior work and is extended to the LTHB-STM in this work. These synthesis systems are not exactly the same, as will be shown by the variability in the results. Method 1 is performed entirely in UHV and with a 2×1 reconstructed Si(100) substrate. The reconstruction was obtained by annealing the Si substrate to ~1200 ºC,[46] and then examined with STM to ensure a high-quality surface reconstruction was present. Si reconstructions are highly vulnerable to disruption by impurities, so it is necessary to confirm that the substrate is atomically clean. Immediately after recovering the desired Si reconstruction, 1-60 layers of Mo are deposited onto the Si substrate at room temperature via e-beam deposition. The substrate is then annealed in the temperature range 750-1000 ºC to reveal a range of surface reconstructions that are characterized with STM.

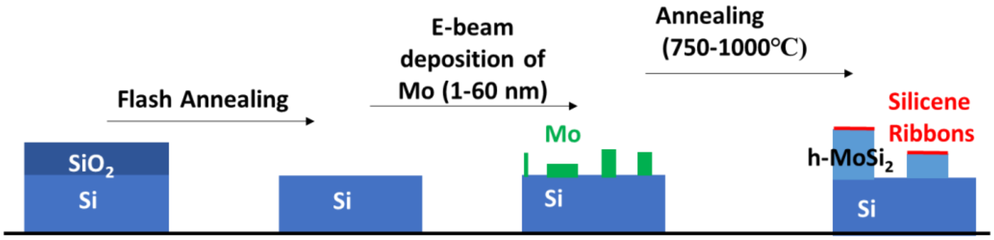

Figure 6.1: Synthesis Method 1 which is conducted entirely under UHV and can be performed at UVa or ORNL.

6.2.2 Method 2

An alternate synthesis method (Figure 6.2) was developed through a collaboration with the McDonnell research group. The motivation for this synthesis method is to achieve ease of direct comparison between UVa and ORNL results, and facilitate experimentation. Method 2 involves performing the depositon under vaccum in one lab and then transferring the sample to the characterization chamber of another lab. This transfer involves the Mo/Si sample spending time under ambient conditions. The Mo layer is meant to act as a protective layer for the Si substrate, to keep it from oxidizing. Molybdenum oxide volatilize at 600 ºC (lower than any annealing temperature used in this work),[180] so the air oxide should be removed while the Mo-Si reaction occurs. The efficacy of this method will depend on the kinetics of the air oxide removal compared to the kinetics of the Mo-Si reaction.

Another difference between Methods 1 and 2 is the cleaning method for the Si surface. In Method 2, the SiO_2 is removed with an HF etching process to H-terminate the substrate. Once under vaccum, the H termination is removed by annealing to reveal a 2×1 surface reconstruction. The presence of this reconstruction can be checked with Low-Energy Electron Diffraction (LEED). Next, 10 nm of Mo is e-beam deposited onto the Si substrate, and the Mo/Si substrate is transferred to ambient conditions. The sample is at ambient conditions for a maximum of 8 hours, after which it is transferred to vaccum at ORNL. The annealing is performed in this vaccum chamber before characterization with the LTHB-STM.

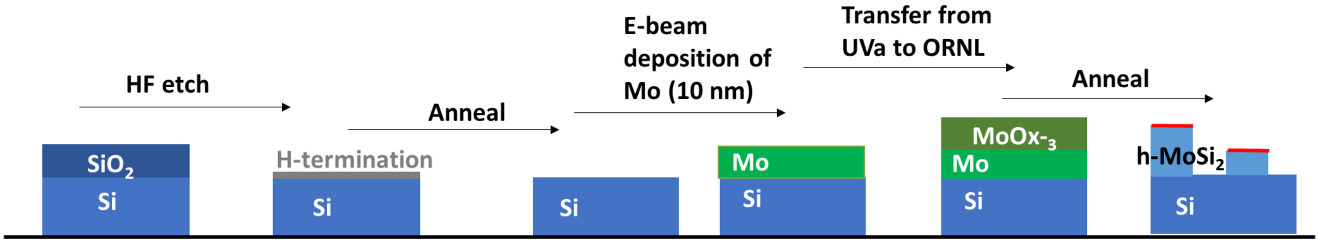

Figure 6.2: Synthesis Method 2 which is started in the McDonnell lab at UVa and completed at ORNL.

6.3 Results

All surface structures characterized here lie on h-$MoSi_2$ crystallites in the (0001) plane, as shown in Figure 6.3. These crystallites were found to exist at all Mo-surface coverages tested (1-60 nm) and are obtained by annealing in the temperature range 750-900 ºC. At temperatures ~1000 ºC, the more thermodynamically favorable tetragonal phase of $MoSi_2$ forms, which is consistent with the literature as described in Section 2.2.1. There is some temperature dependence of the surface reconstructions that are observed on h-$MoSi_2$ in this work, which will be discussed below. The atomic surface structures reported in detail below also appear to be independent of the amount of Mo deposited (over the 1-60 nm range tested).

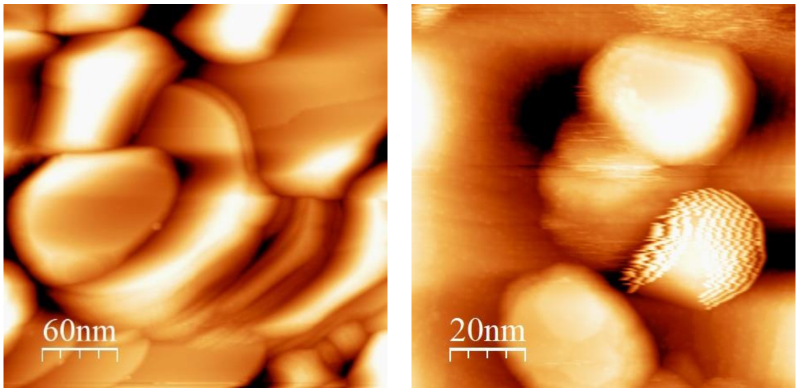

Figure 6.3: STM images of the h-MoSi$_2$ surface taken at V_B = -1.5 V and I_t = 0.1 nA, at (a) high Mo coverages and (b) low Mo coverages against a Si background.

Three electronically and geometrically distinct surface structures were observed and characterized, and are discussed in detail below. Ribbon-silicene, Reconstruction 1, and Reconstruction 2.1 are synthesized with Method 1, while Reconstruction 2.2 and Reconstruction 3 are synthesized with Method 2.

1. Ribbon-Silicene (Section 6.3.1): The electronic structure of ribbon-silicene shows a V-shaped density of states around the Fermi energy, indicating Dirac-like behavior.
2. Additional Surface Reconstructions (Section 6.3.2): The two additional surface reconstructions that coexist with silicene were found to have semiconducting nature.
    a. Reconstruction 1: This reconstruction appears as a large unit cell superstructure with distorted hexagonal symmetry, which matches a superstructure found in our previous results at lower annealing temperatures during the silicide formation.
    b. Reconstruction 2.1: The other is a highly defective honeycomb with topography images that are strongly dependent on bias voltage. The filled state images appear to vary in geometry depending on slight tip changes.

3. Alternative Synthesis Method (Section 6.3.3): Synthesis Method 2 did not give exactly the same results as Method 1. However, there are important similarities between the reconstructions observed with different methods, which will be discussed in Section 6.3.3.
    a. Reconstruction 2.2: The most similar surface between the two methods is called Reconstruction 2 (called 2.1 for Method 1 and 2.2 for Method 2). This reconstruction is semiconducting with bias dependent topography images.
    b. Reconstruction 3: A ribbon-like structure coexists with Reconstruction 2.2. This structure does not appear to have the same geometry within ribbons as ribbon-silicene.

These reconstructions observed on h-$MoSi_2$ crystallites will be characterized and compared, in terms of their geometric and electronic structures.

6.3.1 Ribbon-conformation of Silicene

A ribbon-like surface structure seen in Figure 6.4 was observed that is tentatively interpreted as a new conformation of silicene. This structure is only found on h-$MoSi_2$ crystallites, as shown in Figure 6.4a, which are synthesized entirely at ORNL and characterized with the LTHB-STM. These crystallites appear similar to the prior silicene results obtained at UVa (shown in Figure 2.5) in terms of size (~15-120 nm diameter) and shape. The key difference is the tendency of the silicide crystallites in the ORNL experiments to form dense clusters. Ribbon-silicene is always observed on these clustered, flat-top hexagonal crystallites, as shown in Figure 6.4a and Figure 6.6a. The ribbon-silicene is found at high coverages (Figure 6.4a) and low coverages (Figure 6.6a) with respect to silicide crystallites with no differences in their atomic geometry or electronic structure. This reconstruction is also present on h-MoSi$_2$ crystallites synthesized from low to high temperatures (750-900 ^{o}C).

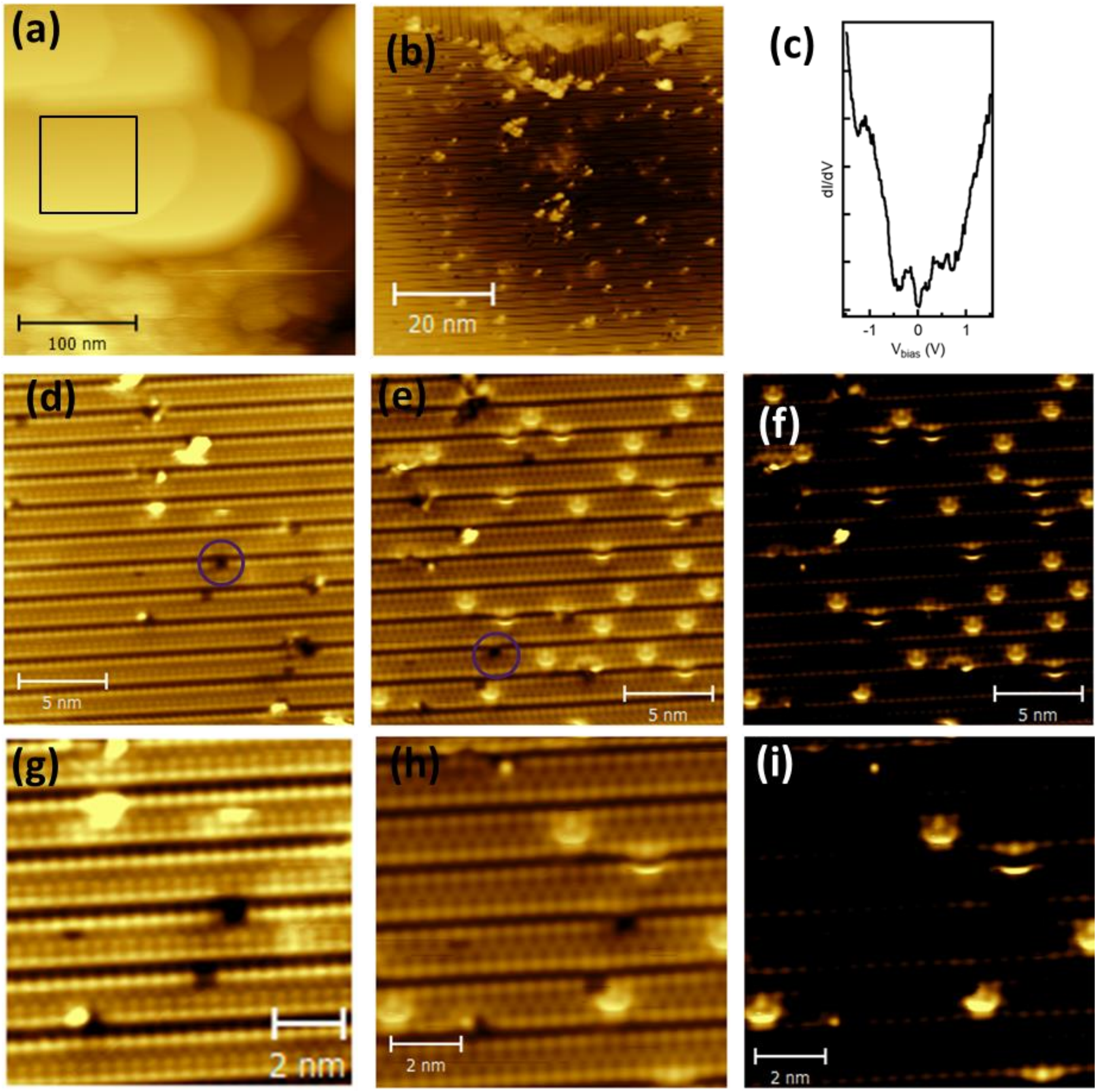

Figure 6.4: Ribbon-silicene on h-MoSi$_2$ crystallites at high Mo coverages, showing (a) the h-MoSi$_2$ crystallites, (b) the grain boundary between ribbon-silicene domains, (c) an average of 20 dI/dV spectra over a linescan along a ribbon axis, (d) 20×20 nm empty state image (V_B = +1.5 V), (e) 20×20 nm filled state image (V_B = -1.5 V), (f) the defects in the 20×20 nm filled state image isolated by contrast manipulation (V_B = -1.5 V), (g) 10×10 nm zoom-in of the empty state image (V_B = +1.5 V), (h) 10×10 filled state image (V_B = -1.5 V), and the defects within the 10×10 filled states image isolated by contrast manipulation (V_B = -1.5 V). All images are at I_t = 0.1 nA

Examining the surface structure within the crystallites, we see tightly spaced ribbons (periodicity of 1.73 ± 0.03 nm) with a characteristic set of defects, as shown in Figure 6.4b. These ribbons appear to be composed of two rows of distorted honeycombs. The ribbon structure is an unusual result to observe on a hexagonal crystallite. While silicene is known to form nanoribbons,[181] prior literature shows these nanoribbons form long, rectangular crystallites. Also unusual, is the presence of a 90° grain boundary between silicene domains, as shown in Figure 6.4b. These geometric differences between the h-$MoSi_2$ crystallites (structures shown in Figure 2.4 of Section 2.2.1) and the silicene-ribbon suggest that the surface may be decoupled from the underlying substrate. The atomic scale structure of the silicene-ribbons are reminiscent of Si-Si dimers observed on buckled Si(100), which are more stable under cryostatic conditions.[182,183] The electronic structure (Figure 6.4c) also suggests that the silicene-ribbons are decoupled, as they has sharp band edges and V type LDOS, indicative of Dirac-type nature. Silicene only has this nature when it is low-buckled and electronically decoupled from the substrate.[21,39] Both, the geometric and electronic structure suggest the silicene is decoupled from the h-$MoSi_2$ substrate.

The internal structure of the ribbons can be seen in Figure 6.4d,e,g,h. These images show the surface geometry of the filled and empty states at two different magnifications. Figure 6.5a shows a line-scan in the direction perpendicular to the ribbon direction. The atomic structure is also shown in the structure model in Figure 6.5b,c. The red and blue atoms in Figure 6.5b,c show the outer and inner apparent atoms locations, respectively. The black atoms correspond to the "dark" trenches, and a justification for their positioning in this model will be described further below. The spacing of the inner-ribbon atoms (blue in Figure 6.5b,c) is 0.36 ± 0.03 nm, which matches perfectly with the lattice constant from the prior silicene work at UVa.[47] The outer-ribbon atoms (red in Figure 6.5b,c) are brighter, larger, and more widely spaced (0.46 ± 0.04 nm). Interestingly, this spacing corresponds exactly to the lattice constant for h-$MoSi_2$. This information suggests the ribbon-silicene may be a transition structure to silicene, decoupled on the ribbon and tethered to the $MoSi_2$ surface at the ribbon boundary.

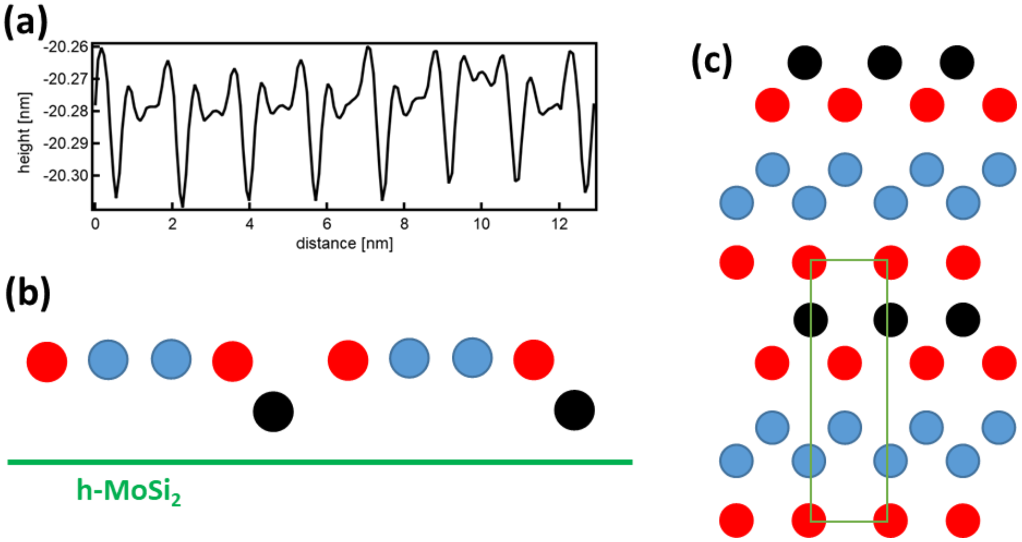

Figure 6.5: (a) A line-scan perpendicular to the ribbon direction taken from a filled states image. The structure model shows the (b) side view and (c) top view. The model is color coded for convenience of discussion: inner-ribbon atoms (blue), outer ribbon atoms (red), and hidden atoms (black).

The filled and empty state images show the same surface geometry, although with slight differences in brightness (Figure 6.4g,h). However, there is a specific type of defect in the filled state images that does not appear when the empty states are imaged. For ease of comparison, a purple circle is shown in Figure 6.4d,h around a defect that has no bias dependence. This marker allows direct comparison of the filled and empty state images. The specific features of the strongly bias dependent defect are shown in Figures 6.4f,i. This defect is three atomic layers wide in the y-direction (perpendicular to the ribbon direction), with the lower two atomic layers forming a curve and the upper layer forming a bright spot. It appears in a similar shape on top of the ribbons, and in-between them. The appearance of these characteristic defects could, in the future, help describe the details of the ribbon-silicene with the help of DFT calculations.

The similarity between defects within and between ribbons suggests that the depressions may be structurally similar to the ribbons themselves. These dark spaces could not be atomically resolved with STM, so any insight into their characteristics is speculative. The similarity of the defect structure suggests that the structure of the dark regions is similar to the visible ribbon structure. Therefore, only one row of atoms is hypothesized to lie in the dark region, as this would make the characteristic defect which overlaps with the dark region three atomic layers wide. The hidden atoms are also assumed to be positioned lower (buckled) in the z-direction (Figure 6.5b). Line scans show that the depressions are less than 0.1 nm in apparent depth (Figure 6.5a), which is a reasonable degree of buckling. However, it is possible that the tip picks up states from the sides of the ribbons, and the actual dark region is much deeper. The line scans can neither confirm nor deny the buckling hypothesis and future work in Density Functional Theory (DFT) is needed to test the surface stability. It also can not be confirmed whether the buckled atoms lie above the $MoSi_2$ substrate (as pictured in Figure 6.5b) and are part of the buckled silicene layer, or if they are attached to, or even part of the $MoSi_2$ substrate.

The ribbon-silicene can also be synthesized at low Mo coverages, as shown in Figure 6.6a. This Figure shows the clustered h-$MoSi_2$ crystallites against a Si background. Higher resolution images Figure 6.6b reveal that the ribbon-silicene can grow in layers. The first and second layer of ribbon-silicene are directly in line with each other, with the dark regions and

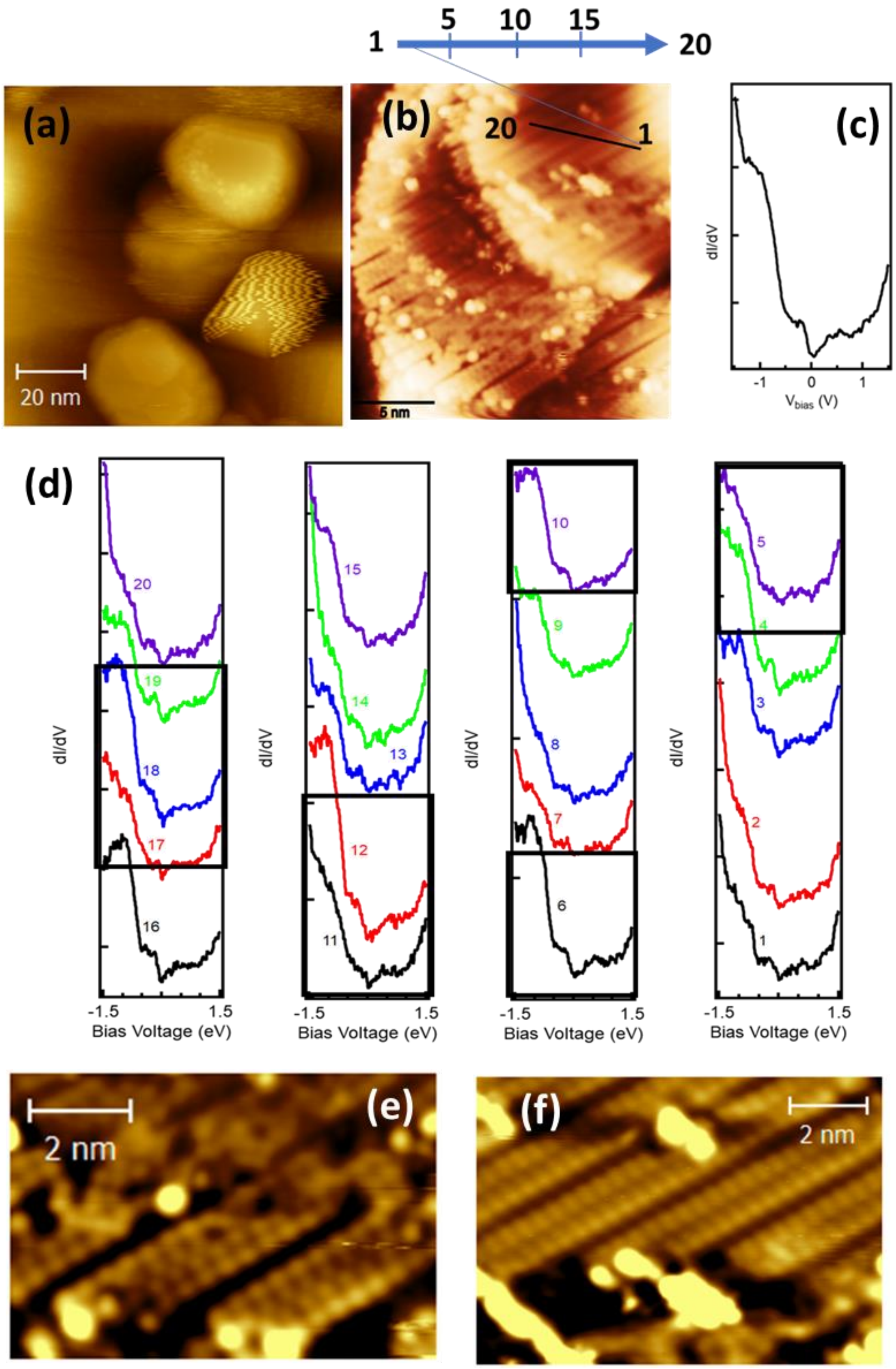

Figure 6.6: Ribbon-silicene on h-MoSi$_2$ crystallites at low Mo coverages, showing (a) the h-MoSi$_2$ crystallites, (b) the layered structure of ribbon-silicene, (c) an average of 20 dI/dV spectra over a linescan, (d) the 20 individual dI/dV spectra within the linescan, (e) zoom-in on the lower ribbon-silicene layer, and (f) zoom-in on the upper ribbon-silicene layer. Imaging conditions: $V_B = -1.5$ V, $I_t = 0.1$ nA.

ribbons lining up perfectly between the upper and lower layer. We can be sure this is not a double-tip effect as the defects are not replicated between the upper and lower layer.

Another feature of the layered structure is that the upper layer differs slightly in the topographic STM images from the lower layer. The outer-ribbon atoms are identical in position, but the inner-ribbon atoms could not be atomically resolved. This discrepancy could be due to a slight difference in buckling between upper and lower layers, or it could be attributed to difficulties in imaging a defect-rich, layered surface. Regardless, the electronic structure (Figure 6.6c) matches the prior ribbon-silicene results (Figure 6.4c), suggesting any difference between layers is subtle. The electronic structure is fairly constant across the ribbons, as shown in Figure 6.6d. The only change in electronic structure with geometry, is the surface state at about -1.2 eV. The spectra that have this state are marked by the black boxes in Figure 6.6d, and correspond to the dark regions between ribbons, suggesting a difference in electronic structure of the lower buckled atoms.

6.3.2 Alternate Surface Reconstructions

There are two alternate surface reconstructions that coexist with ribbon-silicene and are also found on h-$MoSi_2$ crystallites. Both reconstructions are semiconducting and bias dependent in the topography images, although to different degrees. In this section, the alternate surface reconstructions will be electronically and geometrically characterized, and their stabilities relative to ribbon-silicene will be discussed.

One of these reconstructions forms a large, distorted hexagonal superstructure shown in Figure 6.7. This structure will be referred to as Reconstruction 1. R1 is composed of widely spaced superstructure lattice points, with a smaller more closely spaced repeating structure between the superstructure points. The ratio of the number of apparent atoms between large superstructure lattice points and the smaller ones is 1:2. The grain boundary angle between two domains is 60° which is expected for a hexagonal geometry. This surface geometry also has a slight bias dependence. The large superstructure is visible in both the filled and empty state images, but the more closely spaced lattice points are only visible in the filled state images.

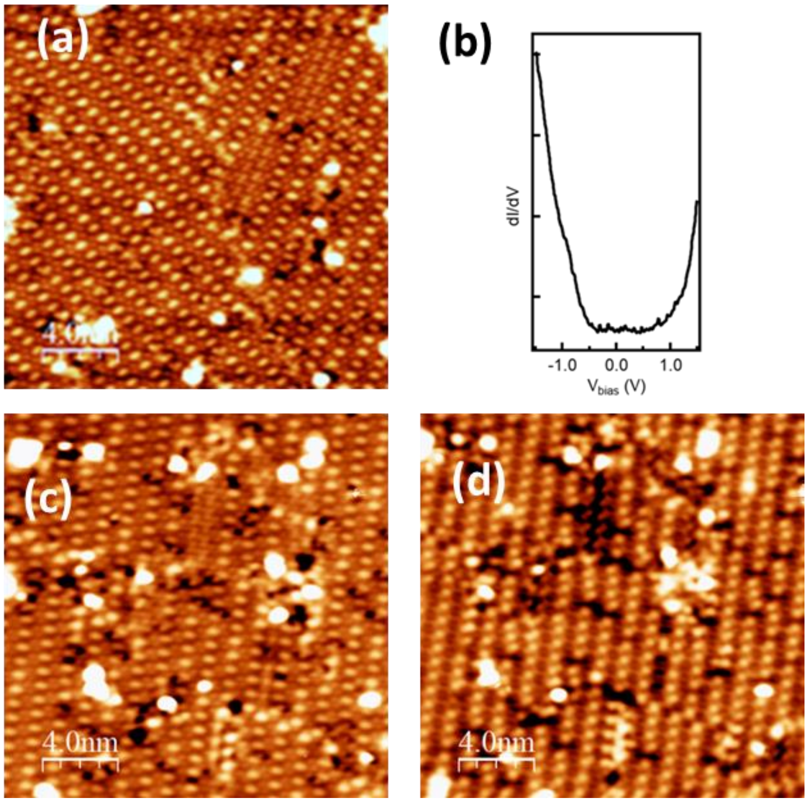

Figure 6.7: STM results for Reconstruction 1, showing the (a) grain boundary on a 20×20 filled states image, (b) an average of 20 dI/dV spectra over a linescan, (c) 20×20 nm filled state image (V$_B$ = -1.5 V), (d) and a 20×20 nm empty state image (V$_B$ = +1.5 V). All images are at I$_t$ = 0.1 nA

Reconstruction 1 bears a strong resemblance to the "low-temperature reconstruction" from prior silicene work at UVa. Both reconstructions coexist with silicene, but are observed more frequently at the lower end of the temperature range (750-800 °C). The previous work was not able to atomically resolve the dimmer atoms between the superstructure. For this reason, the bias dependence of this reconstruction was not revealed. Now that we have more information about this reconstruction from the LTHB-STM images taken at ORNL, it is clear that the previous model for this reconstruction was flawed. The updated ball and stick model for R1 is shown in Figure 6.8. This model is based on a previous interpretation by Roge et. al. for the $ErSi_{1.7}$ reconstruction on Si(111).[184] The authors suggest the distorted hexagonal structure is due to ordered Si vacancies which causes a shift of the nearest neighbor atoms. In analogy, the Mo atoms shift away from the vacancies, and the Si atoms shift toward the vacancies. This effect results in the distorted hexagonal superstructure shown below, where only the upper and lower lying Mo atoms are visible in the STM. The ideal h-$MoSi_2$ lattice is shown to help illustrate the shift of atoms. This model agrees with our experimental results and has literature backing but should also be tested with DFT to ensure it is indeed a stable surface structure.

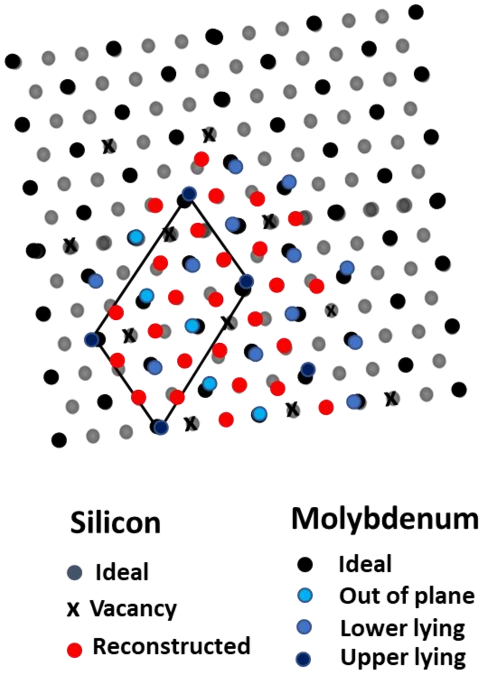

Figure 6.8: The ball and stick model for Reconstruction 1. The large/ bright and small/ dim atoms seen in the STM images correspond to the upper lying and lower lying Mo atoms, respectively, in this model.

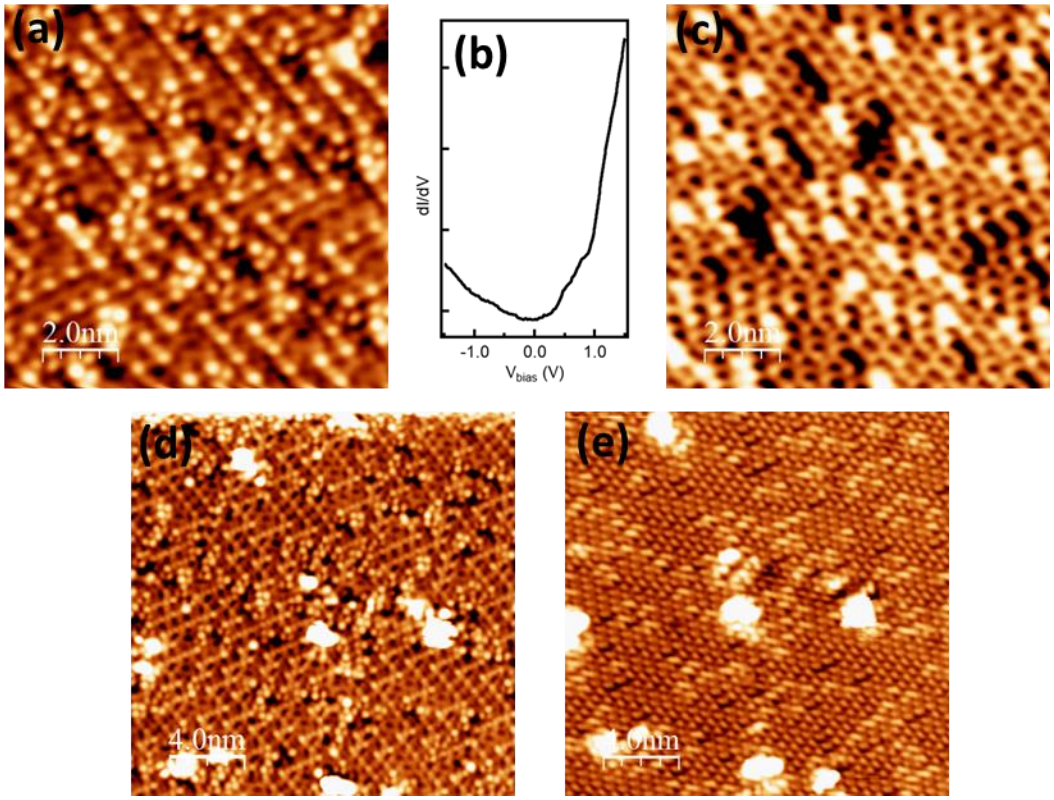

Figure 6.9: STM of Reconstruction 2.1 showing (a) a 10×10 nm image of the filled states (V_B = -1.5), (b) dI/dV average spectrum of 20, (c) a 10×10 nm image of the empty states (V_B = +1.5 V), (d) 30×30 nm image of the filled states (V_B = -1.5), and (e) 30×30 nm image of the empty states (V_B = +1.5). All images are taken at I_t = 0.05 nA.

The other reconstruction found to coexist with ribbon-silicene is Reconstruction 2.1, shown in Figure 6.9. This reconstruction is highly sensitive to bias voltage and tip changes. The bias dependence is illustrated in Figure 6.9a-c. The band edges appears to be highly anisotropic (Figure 6.9b), which is consistent with the high bias-dependence of the images. The electronic structure is semiconducting with a small bandgap of ~0.2 eV. The filled state image (Figure 6.9a) appears a zig zag pattern with an angle of ~60^o between lines of brighter atoms. The spacing between these bright lines is somewhat constant, with some larger spaces or gaps. These gaps correspond to the darker regions in the empty state image (Figure 6.9c) which give the impression of holes embedded in the surface. The larger scale filled (Figure 6.9d) and empty (Figure 6.9e) state images show the same image segment but display a seemingly different atomic arrangement for the empty states.

Figure 6.10 confirms that the difference in empty state images between Figure 6.9c, and 6.9e is due to a tip change. The apparent difference in geometry between Figure 6.9c and e could be the tip changing the surface or the surface changing the tip. However, Figure 6.10 shows the change in geometry occurs exactly in line with the motion of the tip, showing that the STM topography is highly susceptible to tip changes.

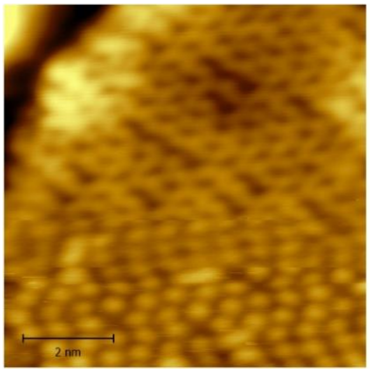

Figure 6.10: STM topography of Reconstruction 2.2, showing the tip change.

Reconstruction 2.1 presents a large variability in local surface structures compared to the other reconstructions, with varying atomic arrangements and degrees of buckling, which is best seen in the empty state images (6.9c,e). The atomic arrangement appears tetragonal in some regions and honeycomb in others, with limited long range order. R2.1 appears most often at higher temperatures (800-1000 °C). This reconstruction is also found to coexist with t-$MoSi_2$, the more thermodynamically favorable structure, at temperatures ~1000 °C (Figure 6.11a-c). The tetragonal phase of $MoSi_2$ is frequently found to have a larger crystallite area and always has a triangular morphology.

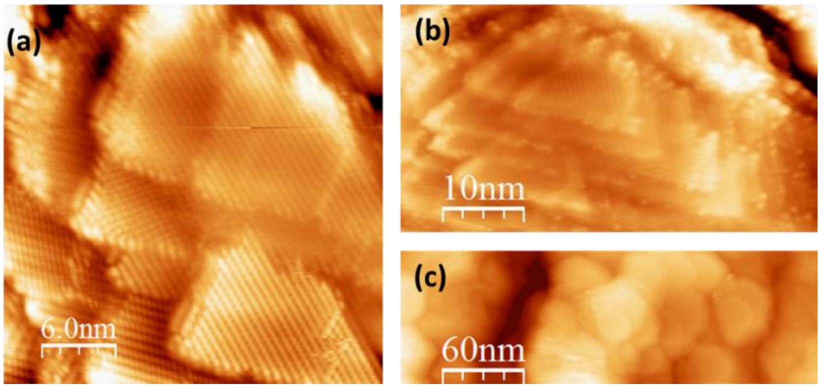

Figure 6.11: STM images showing, t-MoSi$_2$ at (a) a larger scale and (b) a smaller scale. (c) h-MoSi$_2$ is shown to coexist with t-MoSi$_2$. Imaging conditions: V_B = -1.5 V and I_t = 0.1 nA.

6.3.3 Alternate Synthesis Method (Method 2)

Method 2 leads to smaller silicide crystallites on average that are not atomically flat enough to image (Figure 6.12a). Nevertheless, a small number of flat-top h-MoSi$_2$ crystallites were present, as shown in Figure 6.12b. The surface structures of these crystallites will be electronically and geometrically characterized here.

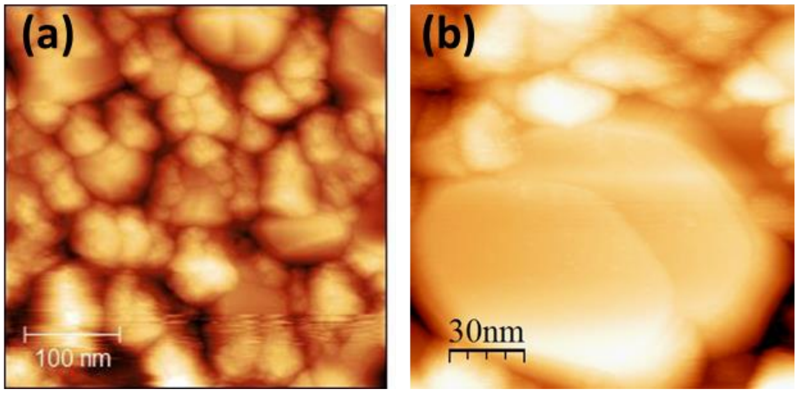

Figure 6.12: STM images of the Mo-Si surface when Method 2 is used, showing (a) the large-scale surface structure, and (b) the h-MoSi2 crystallites. Imaging conditions: V_B = -1.5 V, I_t = 100pA.

The most common surface structure found on the h-MoSi$_2$ crystallites is shown in Figure 6.13. This structure will be referred to as Reconstruction 2.2. This structure is as strongly bias dependent as Reconstruction 2.1, discussed in the previous section. These two structures are also geometrically similar. The filled states image of Reconstruction 2.2 (Figure 6.13a) has the same type of zig zag pattern as the filled states image of Reconstruction 2.1 (Figure 6.9d). The main difference is that the bright lines in R2.1 appear much dimmer in R2.2. The angle of the corners in R2.2 are 60º, similar to that of R2.1, and the bright, round defects are also seen in both reconstructions. The empty states of R2.2 (Figure 6.13b,c) are quite similar to the empty states of R2.1 before the tip change (Figure 6.9e). There is no long range order, and the short range order appears qualitatively to have a higher degree of disorder, compared to R2.1. The filled states of R2.2 also appear to have some regions where brighter atoms form lines corresponding to those in the filled states. There is a blurry, diagonal line going through these R2.2 images of unknown origin that can be used as a visual aid when comparing the atomic arrangements.

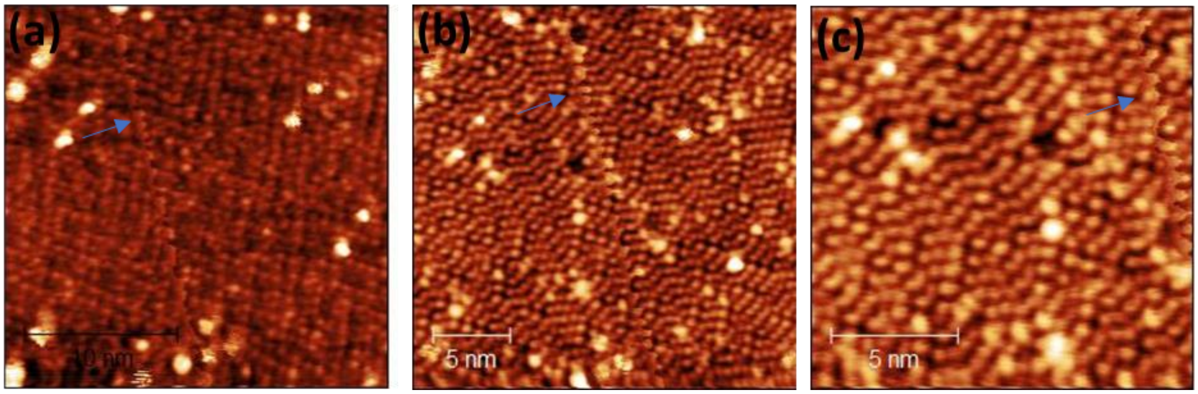

Figure 6.13: STM topography of Reconstruction 2.2 observed on h-$MoSi_2$ synthesized via Method 2, showing (a) a 25×25 nm image of the filled states (V_B = -1.5 V), (b) a 25×25 nm image of the empty states (V_B = +1.5 V), and a (c) 15×15 nm image of the empty states (V_B = +1.5 V). All images are taken at I_t = 0.01 nA.

Another surface structure appearing on an h-$MoSi_2$ crystallite synthesized with Method 2, is that shown in Figure 6.14. This structure will be referred to as Reconstruction 3 and is of interest because it has a similar ribbon type pattern to that of ribbon-silicene discussed previously. The ribbon pattern found here is less ordered than ribbon silicene. The spacing between dark lines is inconsistent in magnitude and the order within the ribbons varies. It is possible that Reconstruction 3 is a transition structure but it seems more likely that the high number of impurities, introduced under ambient conditions, inhibited the formation of high-quality ribbon-silicene. Still, the similarities between the results of Methods 1 and 2 suggest that with further optimization and perhaps the help of a vacuum suitcase, Method 2 will be able to reproduce the prior silicene results.

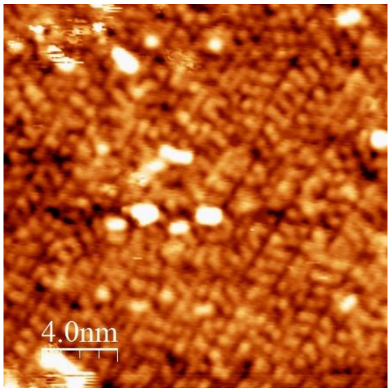

Figure 6.14: STM topography of Reconstruction 3 observed on h-$MoSi_2$ synthesized via Method 2. Imaging conditions: V_B = -1.5 V, I_t = 0.01 nA

6.4 Discussion

A wide range of reconstructions are observed to coexist with ribbon-silicene, all of which are found on flat top h-$MoSi_2$. A number of experiments were performed to determine the dependence of these reconstructions on annealing temperature during formation of silicide crystallites, and thickness of the Mo layer deposited. The effects of these variables are presented in Figure 6.15, with different reconstructions organized by color for ease of interpretation. It can be seen that R1 (framed in blue) is more commonly found in the lower temperature range, R2 (framed in red) is more commonly found at the higher temperature range, and ribbon-silicene (framed in green) is formed at temperatures overlapping with these two reconstructions. Figure

6.15 also shows the formation of t-$MoSi_2$ (framed in purple) at the highest temperatures studied.[185] While many reconstructions coexist with each other, the effect of temperature is still significant. The thickness of the Mo layer (between 1 and 60 nm) appears to have at most a minor impact, as all surface reconstructions are formed at the extreme ends of Mo thickness.

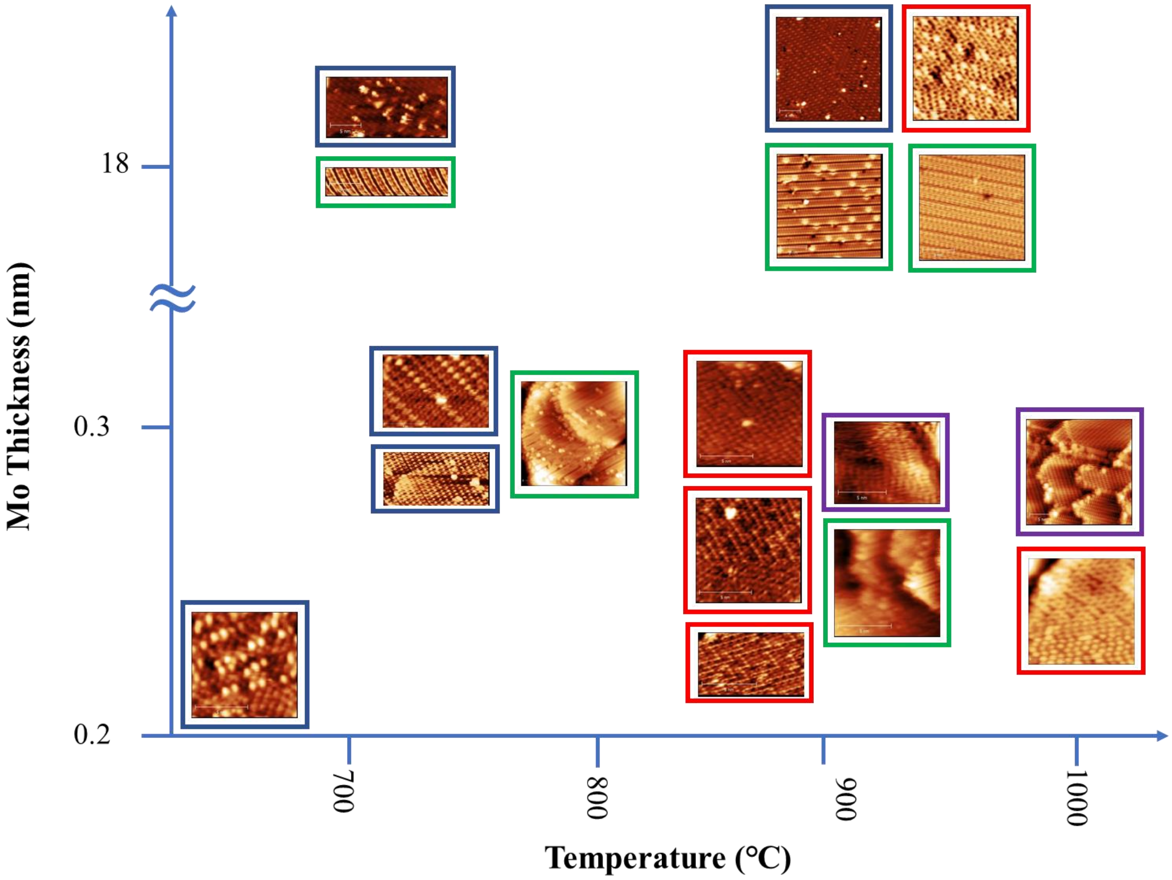

Figure 6.15: Schematic illustrating relationship between thickness of Mo deposited, annealing temperature and surface reconstruction observed with STM. The reconstructions are color coded as follows: R1 = blue, ribbon-silicene = green, R2 = red, t-$MoSi_2$ = purple.

The uniformity of the atomic arrangements on flat-top h-$MoSi_2$ at varied Mo thickness makes sense considering there is a large reservoir of Si available. Therefore, the most Si-rich stoichiometry possible for a Mo-Si, $MoSi_2$, is always formed.[185] It is unusual however that we find no impact of crystallite size (due to strain) on the atomic or electronic structures within the crystallites or on the crystallites morphology, as is common for silicide nano-crystallites.[186,187] The annealing temperature does have a much larger impact on the surface reconstruction formed, which is in agreement with prior silicene results from UVa. The wide range of surface structures formed here mirrors the large number of silicene reconstructions that have been shown to form on the most commonly studied substrate, Ag(111).[19,169,188] Some of those phases have been shown to be Ag-Si alloys,[172] and that is a possibility we cannot completely eliminate for our results without further studies. Experimental work on the chemical nature of the reconstructions or theoretical calculations on the stability of different surface structures would enhance our understanding of this material system greatly.

We hypothesize that the progressive development of the surface structures until silicene ribbons are formed is related to a "decoupling" or delamination of a silicene surface layer from the MoSi2 (0001) surface. In this model, R1 is the first structure to form, at lower temperatures (650-700 ºC). R1 has a distorted honeycomb of Si atoms with ordered Si vacancies and Mo atoms in the center, as shown in the structural model (Figure 6.8). At higher temperatures (750- 900 ºC), the honeycomb of Si atoms begins to decouple, with depressions where the silicene still interacts with the underlying h-$MoSi_2$ (Figure 6.8). Given enough time at high annealing temperature, silicene would fully decouple from the underlying silicide surface. A complete understanding of the different structures requires in the future DFT calculations which will help to understand the experimental results.

6.5 Conclusion

A range of silicene related surface reconstructions are synthesized on flat-top h-$MoSi_2$ crystallites. Two different synthesis methods are employed, giving varied results. The surfaces are observed at ORNL with an STM operating at liquid nitrogen temperatures (77 K). The resultant surface structures are electronically and geometrically characterized. This work focuses on flat-top h-$MoSi_2$ crystallites, as this is the Mo-Si crystallite morphology that has lattice matching with silicene. We observe a reconstruction that is likely ribbon-silicene, with a similar lattice constant to silicene (~0.36 nm) and Dirac-type band edges. The topography appears differently in images of the filled and empty states. The reconstruction also has bias-dependent characteristic defects. These traits make the ribbon-silicene an ideal candidate for DFT calculations. A structural model is suggested for future DFT work.

There are several alternate surface reconstructions that are observed on h-$MoSi_2$ crystallites. These surface reconstructions are formed in temperature ranges and Mo thicknesses that overlap with the synthesis conditions forming ribbon-silicene. R1 is formed in the lower temperature range, and presents as a large unit cell superstructure in a distorted hexagonal arrangement. R2 is formed in the higher temperature range and has a high level of local disorder, making it difficult to assign a unit cell. This reconstruction also has a large bias dependence, with empty state images showing a mixed honeycomb/ tetragonal surface reconstruction. Mo thickness (in the range 0.3- 18 nm) does not have an impact on the surface reconstructions observed. A structural model is proposed to describe the reconstructions observed here, which involves a step-by-step delamination of the silicene from the underlying h-$MoSi_2$ as the sample is annealed. In future work, DFT calculations will be performed to test this model.

Chapter 7: Summary and Future Plans

In the work presented here, a range of 2D materials are synthesized and characterized to ease the transition towards incorporating these materials into multilayer heterostructure devices. The materials investigated (TMDs, silicene and graphene/2D GaN) were chosen for their promising electronic and/or optical properties that make them candidates for a variety of applications, including heterostructure devices.[30,130,132,168] The techniques chosen were tailored to the materials properties to be explored for each experiment.

For instance, when exploring the thermal stability of monolayer WS_2, it was useful to determine the chemical bonds present following each annealing step which made XPS an attractive method. This characterization method informed us that the material system (monolayer WS_2/Au/Ti) underwent a number of surface reactions between the temperatures 275- 625 ºC. The majority of these reactions involve Ti, which is shown to diffuse to the surface at temperatures as low as 275 ºC. Fortunately, the WS_2 is relatively stable, only reacting with Ti at temperatures >600 ºC. WS_2 also lost its air oxide and was doped due to sulfur sublimation, which are both expected to occur in the annealing temperature range explored here. Monolayer WS_2/Au has fairly good thermal stability in the range 275- 600 ºC, but Ti is too reactive in this system to be used as the sticking agent for Au. It is evident that a different sticking agent will have to be used for future device structures.

This thesis also explores the optimal parameter space for the synthesis of monolayer MoS_2 by collecting a dataset of synthesis parameters from literature and exploring it with statistical and machine learning methods. MoS_2 is an ideal material for this type of data-driven approach due to the relatively large volume of publications dedicated to MoS_2 synthesis. A large number of publications was required in order to create a complete dataset. However, despite the numerous publications, the collection of relevant data with respect to materials quality remains challenging. Many publications do not report data for key parameters, or they report them in a manner incompatible with this quantitative approach. The finalized dataset was analyzed with data-driven approaches, allowing for the definition of the ideal parameter space for monolayer MoS_2 synthesis and the determination of which synthesis factors had the largest impact. Mo precursor temperature and chamber pressure were found to be the strongest influencers on MoS_2 growth. Future work will involve dataset construction in a more automated approach or via experimental work to explore sizable gaps in the parameter space. This work provides knowledge of the synthesis parameter space which is necessary to grow 2D materials on top of each other to form multilayer heterostructures.

The synthesis and characterization of silicene on substrates that retain its Dirac-type electronic structure are of the utmost importance for realization of silicene's intriguing theoretically predicted electronic properties. Here, silicene synthesis on h-$MoSi_2$ is explored because this substrate has lattice matching with silicene (which avoids formation of high-buckled silicene) and a semiconducting nature (which avoids band hybridization with silicene). A range of silicene-related structures are synthesized on h-$MoSi_2$ and characterized with STM/STS at cryostatic temperatures (77 K). Among these, is a ribbon-like honeycomb reconstruction with Dirac-type band edges. Structural models are suggested, which will have to be tested with DFT calculations in future work.

I performed two other characterization studies in my time at UVa that are not included here. The first was a study of the nucleation mechanism of graphene encapsulation of Ga. This encapsulation method is a key step in synthesizing 2D GaN, a novel wide-gap semiconductor that is not stable in the 2D form without graphene stabilizing its dangling bonds, and forms at the graphene-substrate interface. The graphene was characterized in this work before and after Ga deposition in order to shed light on which defects the Ga intercalated through. These defects were electronically and geometrically characterized with STM/STS. Preliminary results suggest that the graphene has a number of vacancies and divacancies before Ga deposition. After deposition, the Ga appears to passivate these defects, but also gathers at the step edges and covers the pristine graphene as well. Future work will involve characterization of graphene sample with significantly less Ga deposited to determine which sites are favored.

The other characterization study not included in this thesis is an atomic scale characterization of the electronic and geometric structure of MBE-grown 2D WSe_2 on graphite with STM/STS. This surface is explored because of its potential in optical and electronic devices, and the defects are of interest because they control the optical and electronic properties. Preliminary results show a rich diversity of point defects, some of which are bias-dependent in their expression in the STM topography images. Future work will involve the complete analysis of the surface defects on monolayer WSe_2, and comparison to previous r.t. STM/STS results taken at UVa.[189]

Appendix

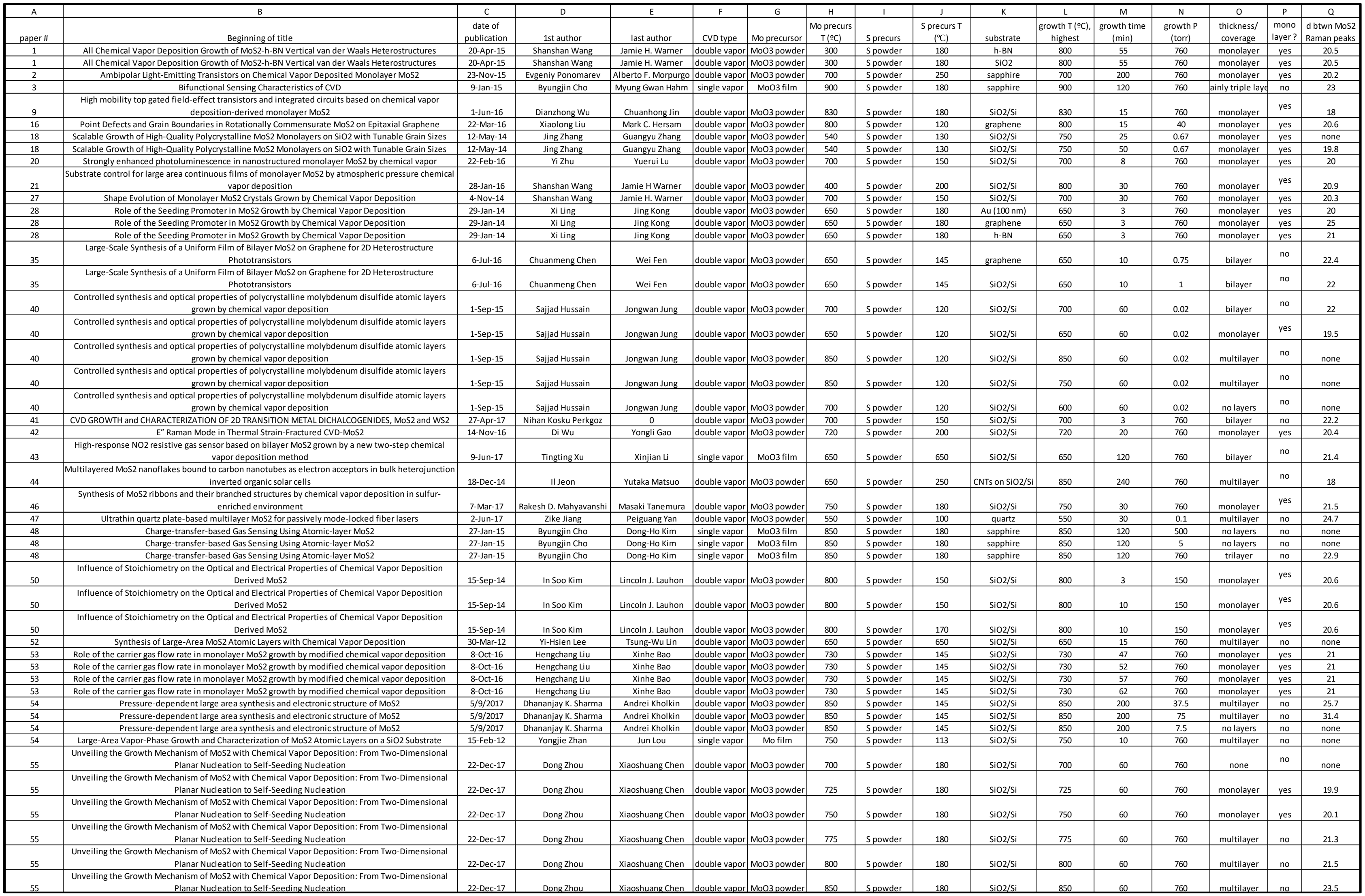

A	B	C	D	E	F	G	H	I	J	K	L	M	N	O	P	Q
paper #	Beginning of title	date of publication	1st author	last author	CVD type	Mo precursor	Mo precurs T (ºC)	S precurs	S precurs T (℃)	substrate	growth T (ºC), highest	growth time (min)	growth P (torr)	thickness/ coverage	mono layer ?	d btwn MoS2 Raman peaks
1	All Chemical Vapor Deposition Growth of MoS2-h-BN Vertical van der Waals Heterostructures	20-Apr-15	Shanshan Wang	Jamie H. Warner	double vapor	MoO3 powder	300	S powder	180	h-BN	800	55	760	monolayer	yes	20.5
1	All Chemical Vapor Deposition Growth of MoS2-h-BN Vertical van der Waals Heterostructures	20-Apr-15	Shanshan Wang	Jamie H. Warner	double vapor	MoO3 powder	300	S powder	180	SiO2	800	55	760	monolayer	yes	20.5
2	Ambipolar Light-Emitting Transistors on Chemical Vapor Deposited Monolayer MoS2	23-Nov-15	Evgeniy Ponomarev	Alberto F. Morpurgo	double vapor	MoO3 powder	700	S powder	250	sapphire	700	200	760	monolayer	yes	20.2
3	Bifunctional Sensing Characteristics of CVD	9-Jan-15	Byungjin Cho	Myung Gwan Hahm	single vapor	MoO3 film	900	S powder	180	sapphire	900	120	760	ainly triple laye	no	23
9	High mobility top gated field-effect transistors and integrated circuits based on chemical vapor deposition-derived monolayer MoS2	1-Jun-16	Dianzhong Wu	Chuanhong Jin	double vapor	MoO3 powder	830	S powder	180	SiO2/Si	830	15	760	monolayer	yes	18
16	Point Defects and Grain Boundaries in Rotationally Commensurate MoS2 on Epitaxial Graphene	22-Mar-16	Xiaolong Liu	Mark C. Hersam	double vapor	MoO3 powder	800	S powder	120	graphene	800	15	40	monolayer	yes	20.6
18	Scalable Growth of High-Quality Polycrystalline MoS2 Monolayers on SiO2 with Tunable Grain Sizes	12-May-14	Jing Zhang	Guangyu Zhang	double vapor	MoO3 powder	540	S powder	130	SiO2/Si	750	25	0.67	monolayer	yes	none
18	Scalable Growth of High-Quality Polycrystalline MoS2 Monolayers on SiO2 with Tunable Grain Sizes	12-May-14	Jing Zhang	Guangyu Zhang	double vapor	MoO3 powder	540	S powder	130	SiO2/Si	750	50	0.67	monolayer	yes	19.8
20	Strongly enhanced photoluminescence in nanostructured monolayer MoS2 by chemical vapor	22-Feb-16	Yi Zhu	Yuerui Lu	double vapor	MoO3 powder	700	S powder	150	SiO2/Si	700	8	760	monolayer	yes	20
21	Substrate control for large area continuous films of monolayer MoS2 by atmospheric pressure chemical vapor deposition	28-Jan-16	Shanshan Wang	Jamie H Warner	double vapor	MoO3 powder	400	S powder	200	SiO2/Si	800	30	760	monolayer	yes	20.9
27	Shape Evolution of Monolayer MoS2 Crystals Grown by Chemical Vapor Deposition	4-Nov-14	Shanshan Wang	Jamie H. Warner	double vapor	MoO3 powder	700	S powder	150	SiO2/Si	700	30	760	monolayer	yes	20.3
28	Role of the Seeding Promoter in MoS2 Growth by Chemical Vapor Deposition	29-Jan-14	Xi Ling	Jing Kong	double vapor	MoO3 powder	650	S powder	180	Au (100 nm)	650	3	760	monolayer	yes	20
28	Role of the Seeding Promoter in MoS2 Growth by Chemical Vapor Deposition	29-Jan-14	Xi Ling	Jing Kong	double vapor	MoO3 powder	650	S powder	180	graphene	650	3	760	monolayer	yes	25
28	Role of the Seeding Promoter in MoS2 Growth by Chemical Vapor Deposition	29-Jan-14	Xi Ling	Jing Kong	double vapor	MoO3 powder	650	S powder	180	h-BN	650	3	760	monolayer	yes	21
35	Large-Scale Synthesis of a Uniform Film of Bilayer MoS2 on Graphene for 2D Heterostructure Phototransistors	6-Jul-16	Chuanmeng Chen	Wei Fen	double vapor	MoO3 powder	650	S powder	145	graphene	650	10	0.75	bilayer	no	22.4
35	Large-Scale Synthesis of a Uniform Film of Bilayer MoS2 on Graphene for 2D Heterostructure Phototransistors	6-Jul-16	Chuanmeng Chen	Wei Fen	double vapor	MoO3 powder	650	S powder	145	SiO2/Si	650	10	1	bilayer	no	22
40	Controlled synthesis and optical properties of polycrystalline molybdenum disulfide atomic layers grown by chemical vapor deposition	1-Sep-15	Sajjad Hussain	Jongwan Jung	double vapor	MoO3 powder	700	S powder	120	SiO2/Si	700	60	0.02	bilayer	no	22
40	Controlled synthesis and optical properties of polycrystalline molybdenum disulfide atomic layers grown by chemical vapor deposition	1-Sep-15	Sajjad Hussain	Jongwan Jung	double vapor	MoO3 powder	650	S powder	120	SiO2/Si	650	60	0.02	monolayer	yes	19.5
40	Controlled synthesis and optical properties of polycrystalline molybdenum disulfide atomic layers grown by chemical vapor deposition	1-Sep-15	Sajjad Hussain	Jongwan Jung	double vapor	MoO3 powder	850	S powder	120	SiO2/Si	850	60	0.02	multilayer	no	none
40	Controlled synthesis and optical properties of polycrystalline molybdenum disulfide atomic layers grown by chemical vapor deposition	1-Sep-15	Sajjad Hussain	Jongwan Jung	double vapor	MoO3 powder	850	S powder	120	SiO2/Si	750	60	0.02	multilayer	no	none
40	Controlled synthesis and optical properties of polycrystalline molybdenum disulfide atomic layers grown by chemical vapor deposition	1-Sep-15	Sajjad Hussain	Jongwan Jung	double vapor	MoO3 powder	700	S powder	120	SiO2/Si	600	60	0.02	no layers	no	none
41	CVD GROWTH and CHARACTERIZATION OF 2D TRANSITION METAL DICHALCOGENIDES, MoS2 and WS2	27-Apr-17	Nihan Kosku Perkgoz	0	double vapor	MoO3 powder	700	S powder	150	SiO2/Si	700	3	760	bilayer	no	22.2
42	E" Raman Mode in Thermal Strain-Fractured CVD-MoS2	14-Nov-16	Di Wu	Yongli Gao	double vapor	MoO3 powder	720	S powder	200	SiO2/Si	720	20	760	monolayer	yes	20.4
43	High-response NO2 resistive gas sensor based on bilayer MoS2 grown by a new two-step chemical vapor deposition method	9-Jun-17	Tingting Xu	Xinjian Li	single vapor	MoO3 film	650	S powder	650	SiO2/Si	650	120	760	bilayer	no	21.4
44	Multilayered MoS2 nanoflakes bound to carbon nanotubes as electron acceptors in bulk heterojunction inverted organic solar cells	18-Dec-14	Il Jeon	Yutaka Matsuo	double vapor	MoO3 powder	650	S powder	250	CNTs on SiO2/Si	850	240	760	multilayer	no	18
46	Synthesis of MoS2 ribbons and their branched structures by chemical vapor deposition in sulfur-enriched environment	7-Mar-17	Rakesh D. Mahyavanshi	Masaki Tanemura	double vapor	MoO3 powder	750	S powder	180	SiO2/Si	750	30	760	monolayer	yes	21.5
47	Ultrathin quartz plate-based multilayer MoS2 for passively mode-locked fiber lasers	2-Jun-17	Zike Jiang	Peiguang Yan	double vapor	MoO3 powder	550	S powder	100	quartz	550	30	0.1	multilayer	no	24.7
48	Charge-transfer-based Gas Sensing Using Atomic-layer MoS2	27-Jan-15	Byungjin Cho	Dong-Ho Kim	single vapor	MoO3 film	850	S powder	180	sapphire	850	120	500	no layers	no	none
48	Charge-transfer-based Gas Sensing Using Atomic-layer MoS2	27-Jan-15	Byungjin Cho	Dong-Ho Kim	single vapor	MoO3 film	850	S powder	180	sapphire	850	120	5	no layers	no	none
48	Charge-transfer-based Gas Sensing Using Atomic-layer MoS2	27-Jan-15	Byungjin Cho	Dong-Ho Kim	single vapor	MoO3 film	850	S powder	180	sapphire	850	120	760	trilayer	no	22.9
50	Influence of Stoichiometry on the Optical and Electrical Properties of Chemical Vapor Deposition Derived MoS2	15-Sep-14	In Soo Kim	Lincoln J. Lauhon	double vapor	MoO3 powder	800	S powder	150	SiO2/Si	800	3	150	monolayer	yes	20.6
50	Influence of Stoichiometry on the Optical and Electrical Properties of Chemical Vapor Deposition Derived MoS2	15-Sep-14	In Soo Kim	Lincoln J. Lauhon	double vapor	MoO3 powder	800	S powder	150	SiO2/Si	800	10	150	monolayer	yes	20.6
50	Influence of Stoichiometry on the Optical and Electrical Properties of Chemical Vapor Deposition Derived MoS2	15-Sep-14	In Soo Kim	Lincoln J. Lauhon	double vapor	MoO3 powder	800	S powder	170	SiO2/Si	800	10	150	monolayer	yes	20.6
52	Synthesis of Large-Area MoS2 Atomic Layers with Chemical Vapor Deposition	30-Mar-12	Yi-Hsien Lee	Tsung-Wu Lin	double vapor	MoO3 powder	650	S powder	650	SiO2/Si	650	15	760	multilayer	no	none
53	Role of the carrier gas flow rate in monolayer MoS2 growth by modified chemical vapor deposition	8-Oct-16	Hengchang Liu	Xinhe Bao	double vapor	MoO3 powder	730	S powder	145	SiO2/Si	730	47	760	monolayer	yes	21
53	Role of the carrier gas flow rate in monolayer MoS2 growth by modified chemical vapor deposition	8-Oct-16	Hengchang Liu	Xinhe Bao	double vapor	MoO3 powder	730	S powder	145	SiO2/Si	730	52	760	monolayer	yes	21
53	Role of the carrier gas flow rate in monolayer MoS2 growth by modified chemical vapor deposition	8-Oct-16	Hengchang Liu	Xinhe Bao	double vapor	MoO3 powder	730	S powder	145	SiO2/Si	730	57	760	monolayer	yes	21
53	Role of the carrier gas flow rate in monolayer MoS2 growth by modified chemical vapor deposition	8-Oct-16	Hengchang Liu	Xinhe Bao	double vapor	MoO3 powder	730	S powder	145	SiO2/Si	730	62	760	monolayer	yes	21
54	Pressure-dependent large area synthesis and electronic structure of MoS2	5/9/2017	Dhananjay K. Sharma	Andrei Kholkin	double vapor	MoO3 powder	850	S powder	145	SiO2/Si	850	200	37.5	multilayer	no	25.7
54	Pressure-dependent large area synthesis and electronic structure of MoS2	5/9/2017	Dhananjay K. Sharma	Andrei Kholkin	double vapor	MoO3 powder	850	S powder	145	SiO2/Si	850	200	75	multilayer	no	31.4
54	Pressure-dependent large area synthesis and electronic structure of MoS2	5/9/2017	Dhananjay K. Sharma	Andrei Kholkin	double vapor	MoO3 powder	850	S powder	145	SiO2/Si	850	200	7.5	no layers	no	none
54	Large-Area Vapor-Phase Growth and Characterization of MoS2 Atomic Layers on a SiO2 Substrate	15-Feb-12	Yongjie Zhan	Jun Lou	single vapor	Mo film	750	S powder	113	SiO2/Si	750	10	760	multilayer	no	none
55	Unveiling the Growth Mechanism of MoS2 with Chemical Vapor Deposition: From Two-Dimensional Planar Nucleation to Self-Seeding Nucleation	22-Dec-17	Dong Zhou	Xiaoshuang Chen	double vapor	MoO3 powder	700	S powder	180	SiO2/Si	700	60	760	none	no	none
55	Unveiling the Growth Mechanism of MoS2 with Chemical Vapor Deposition: From Two-Dimensional Planar Nucleation to Self-Seeding Nucleation	22-Dec-17	Dong Zhou	Xiaoshuang Chen	double vapor	MoO3 powder	725	S powder	180	SiO2/Si	725	60	760	monolayer	yes	19.9
55	Unveiling the Growth Mechanism of MoS2 with Chemical Vapor Deposition: From Two-Dimensional Planar Nucleation to Self-Seeding Nucleation	22-Dec-17	Dong Zhou	Xiaoshuang Chen	double vapor	MoO3 powder	750	S powder	180	SiO2/Si	750	60	760	monolayer	yes	20.1
55	Unveiling the Growth Mechanism of MoS2 with Chemical Vapor Deposition: From Two-Dimensional Planar Nucleation to Self-Seeding Nucleation	22-Dec-17	Dong Zhou	Xiaoshuang Chen	double vapor	MoO3 powder	775	S powder	180	SiO2/Si	775	60	760	multilayer	no	21.3
55	Unveiling the Growth Mechanism of MoS2 with Chemical Vapor Deposition: From Two-Dimensional Planar Nucleation to Self-Seeding Nucleation	22-Dec-17	Dong Zhou	Xiaoshuang Chen	double vapor	MoO3 powder	800	S powder	180	SiO2/Si	800	60	760	multilayer	no	21.5
55	Unveiling the Growth Mechanism of MoS2 with Chemical Vapor Deposition: From Two-Dimensional Planar Nucleation to Self-Seeding Nucleation	22-Dec-17	Dong Zhou	Xiaoshuang Chen	double vapor	MoO3 powder	850	S powder	180	SiO2/Si	850	60	760	multilayer	no	23.5

A	B	C	D	E	F	G	H	I	J	K	L	M	N	O	P	Q
paper #	Beginning of title	date of publication	1st author	last author	CVD type	Mo precursor	Mo precurs T (ºC)	S precurs	S precurs T (℃)	substrate	growth T (ºC), highest	growth time (min)	growth P (torr)	thickness/ coverage	mono layer ?	d btwn MoS2 Raman peaks
1LowP	Epitaxial Monolayer MoS2 on Mica with Novel Photoluminescence	Jul-30-2013	Qingqing Ji	Zhongfan Liu	double vapor	MoO3 powder	530	S powder	100	mica	700	20	0.225	monolayer	yes	none
1LowP	Epitaxial Monolayer MoS2 on Mica with Novel Photoluminescence	Jul-30-2013	Qingqing Ji	Zhongfan Liu	double vapor	MoO3 powder	500	S powder	100	mica	700	45	0.225	no layers	no	none
1LowP	Epitaxial Monolayer MoS2 on Mica with Novel Photoluminescence	Jul-30-2013	Qingqing Ji	Zhongfan Liu	double vapor	MoO3 powder	600	S powder	100	mica	700	45	0.225	no layers	no	none
1LowP	Epitaxial Monolayer MoS2 on Mica with Novel Photoluminescence	Jul-30-2013	Qingqing Ji	Zhongfan Liu	double vapor	MoO3 powder	530	S powder	100	mica	700	120	0.225	multilayer	no	none
1LowP	Epitaxial Monolayer MoS2 on Mica with Novel Photoluminescence	Jul-30-2013	Qingqing Ji	Zhongfan Liu	double vapor	MoO3 powder	530	S powder	100	mica	700	35	0.225	monolayer	yes	20
2LowP	Controllable Growth and Transfer of Monolayer MoS2 on Au Foils and Its Potential Application in Hydrogen Evolution Reaction	Sep-11-2014	J Shi	Zhongfan Liu	double vapor	MoO3 powder	530	S powder	102	Au foils	530	30	0.225	monolayer	yes	19.9
2LowP	Controllable Growth and Transfer of Monolayer MoS2 on Au Foils and Its Potential Application in Hydrogen Evolution Reaction	Sep-11-2014	J Shi	Zhongfan Liu	double vapor	MoO3 powder	530	S powder	102	Au foils	610	30	0.225	monolayer	yes	19.9
2LowP	Controllable Growth and Transfer of Monolayer MoS2 on Au Foils and Its Potential Application in Hydrogen Evolution Reaction	Sep-11-2014	J Shi	Zhongfan Liu	double vapor	MoO3 powder	530	S powder	102	Au foils	680	30	0.225	monolayer	yes	19.9
2LowP	Controllable Growth and Transfer of Monolayer MoS2 on Au Foils and Its Potential Application in Hydrogen Evolution Reaction	Sep-11-2014	J Shi	Zhongfan Liu	double vapor	MoO3 powder	530	S powder	102	Au foils	750	30	0.225	monolayer	yes	19.9
3LowP	Dendritic, Transferable, Strictly Monolayer MoS2 Flakes Synthesized on SrTiO3 Single Crystals for Efficient Electrocatalytic Applications	Jul-17-2014	Yu Zhang	Zhongfan Liu	double vapor	MoO3 powder	530	S powder	100	SrTiO3	880	60	0.225	monolayer	yes	18.3
4LowP	Monolayer MoS 2 Growth on Au Foils and On-Site Domain Boundary Imaging	Dec-15-2014	Jianping Shi	Yanfeng Zhang	double vapor	MoO3 powder	530	S powder	102	Au foils	680	60	0.124	monolayer	yes	19.9
5LowP	Large-Area, Transfer-Free, Oxide-Assisted Synthesis of Hexagonal Boron Nitride Films and Their Heterostructures with MoS2 and WS2	Sep-21-2015	Sanjay Behura	Vikas Berry	double vapor	MoO3 powder	800	S powder	250	h-BN	800	30	10	multilayer	no	25.9
5LowP	Large-Area, Transfer-Free, Oxide-Assisted Synthesis of Hexagonal Boron Nitride Films and Their Heterostructures with MoS2 and WS2	Sep-21-2015	Sanjay Behura	Vikas Berry	double vapor	MoO3 powder	800	S powder	250	h-BN	800	60	10	multilayer	no	25.9
6LowP	Unravelling Orientation Distribution and Merging Behavior of Monolayer MoS2 Domains on Sapphire	Nov-1-2014	Qingqing Ji	Zhongfan Liu	double vapor	MoO3 powder	530	S powder	100	sapphire	850	60	0.225	monolayer	yes	20
6LowP	Unravelling Orientation Distribution and Merging Behavior of Monolayer MoS2 Domains on Sapphire	Nov-1-2014	Qingqing Ji	Zhongfan Liu	double vapor	MoO3 powder	530	S powder	100	sapphire	830	60	0.225	monolayer	yes	20
6LowP	Unravelling Orientation Distribution and Merging Behavior of Monolayer MoS2 Domains on Sapphire	Nov-1-2014	Qingqing Ji	Zhongfan Liu	double vapor	MoO3 powder	530	S powder	100	sapphire	850	10	0.225	monolayer	yes	20
6LowP	Unravelling Orientation Distribution and Merging Behavior of Monolayer MoS2 Domains on Sapphire	Nov-1-2014	Qingqing Ji	Zhongfan Liu	double vapor	MoO3 powder	530	S powder	100	sapphire	830	10	0.225	monolayer	yes	20
7LowP	Oxygen-Assisted Chemical Vapor Deposition Growth of Large SingleCrystal and High-Quality Monolayer MoS2	Dec-1-2015	Wei Chen	Guangyu Zhang	double vapor	MoO3 powder	530	S powder	115	SiO2	850	30	0.5	multilayer	no	24.8
8LowP	Substrate Facet Effect on the Growth of Monolayer MoS2 on Au Foils	Mar-23-2015	Jianping Shi	Yanfeng Zhang	double vapor	MoO3 powder	530	S powder	102	Au foils	530	60	0.225	monolayer	yes	19.9
8LowP	Substrate Facet Effect on the Growth of Monolayer MoS2 on Au Foils	Mar-23-2015	Jianping Shi	Yanfeng Zhang	double vapor	MoO3 powder	530	S powder	102	Au foils	610	60	0.225	monolayer	yes	19.9
8LowP	Substrate Facet Effect on the Growth of Monolayer MoS2 on Au Foils	Mar-23-2015	Jianping Shi	Yanfeng Zhang	double vapor	MoO3 powder	530	S powder	102	Au foils	680	60	0.225	monolayer	yes	19.9
8LowP	Substrate Facet Effect on the Growth of Monolayer MoS2 on Au Foils	Mar-23-2015	Jianping Shi	Yanfeng Zhang	double vapor	MoO3 powder	530	S powder	102	Au foils	750	60	0.225	monolayer	yes	19.9
9LowP	Large-Scale Synthesis of a Uniform Film of Bilayer MoS2 on Graphene for 2D Heterostructure Phototransistors	Jul-06-2016	Chuanmeng Chen	Wei Feng	double vapor	MoO3 powder	650	S powder	145	SiO2/Si	650	10	1	bilayer	no	22.4

Figure A1. The dataset, which includes references cited here, [14,94,96,98–128] and is described further in Chapter 5: Columns A-E: Manuscript Identifier, Column F: Type of CVD reactor, Columns G-H: Information about precursor type (powder, thin film) and temperature during the growth process, Columns K,L: Substrate type and temperature during the growth process, Columns M-O: growth time and pressure, Column P: Outcome of growth process. "Monolayer" of "Not a Monolayer" is used to encode outcome and Column Q: Raman spectroscopy peak split.

References:

1. Zhang, Y., Tan, Y.-W., Stormer, H. L. & Kim, P. Experimental observation of the quantum Hall effect and Berry's phase in graphene. *Nature* **438**, 201–204 (2005).
2. Novoselov, K. S. *et al.* Two-dimensional gas of massless Dirac fermions in graphene. *Nature* **438**, 197–200 (2005).
3. Geim, A. K. & Novoselov, K. S. The Rise of Graphene. *Nat. Mater.* **6**, (2007).
4. Benoit Dubertret, Thomas Heine & Mauricio Terrones. The Rise of Two-Dimensional Materials. *Acc Chem Res* **48**, (2015).
5. Kara, A. *et al.* A review on silicene — New candidate for electronics. *Surf. Sci. Rep.* **67**, 1–18 (2012).
6. Manzeli, S., Ovchinnikov, D., Pasquier, D., Yazyev, O. V. & Kis, A. 2D transition metal dichalcogenides. *Nat. Rev. Mater.* **2**, 17033 (2017).
7. Watanabe, K., Taniguchi, T. & Kanda, H. Direct-bandgap properties and evidence for ultraviolet lasing of hexagonal boron nitride single crystal. *Nat. Mater.* **3**, 404–409 (2004).
8. Geim, A. K. & Grigorieva, I. V. Van der Waals heterostructures. *Nature* **499**, 419–425 (2013).
9. Zhu, M., Sun, Z., Fujitsuka, M. & Majima, T. Z-Scheme Photocatalytic Water Splitting on a 2D Heterostructure of Black Phosphorus/Bismuth Vanadate Using Visible Light. *Angew. Chem. Int. Ed.* **57**, 2160–2164 (2018).
10. Xu, H. *et al.* 2D heterostructure comprised of metallic 1T-MoS_2/Monolayer O-g-C_3N_4 towards efficient photocatalytic hydrogen evolution. *Appl. Catal. B Environ.* **220**, 379–385 (2018).
11. Ross, J. S. *et al.* Interlayer Exciton Optoelectronics in a 2D Heterostructure p–n Junction. *Nano Lett.* **17**, 638–643 (2017).

12. Chen, J., Xiao, X., Wang, Y. & Ye, Z. Ag nanoparticles decorated WO_3/g-C_3N_4 2D/2D heterostructure with enhanced photocatalytic activity for organic pollutants degradation. *Appl. Surf. Sci.* **467–468**, 1000–1010 (2019).

13. Cho, B. *et al.* Chemical Sensing of 2D Graphene/MoS_2 Heterostructure device. *ACS Appl. Mater. Interfaces* **7**, 16775–16780 (2015).

14. Chen, C. *et al.* Large-Scale Synthesis of a Uniform Film of Bilayer MoS_2 on Graphene for 2D Heterostructure Phototransistors. *ACS Appl. Mater. Interfaces* **8**, 19004–19011 (2016).

15. Chen, C. *et al.* Large-Scale Synthesis of a Uniform Film of Bilayer MoS_2 on Graphene for 2D Heterostructure Phototransistors. *ACS Appl. Mater. Interfaces* **8**, 19004–19011 (2016).

16. Li, X. & Zhu, H. Two-dimensional MoS2: Properties, preparation, and applications. *J. Materiomics* **1**, 33–44 (2015).

17. Schleder, G. R., Padilha, A. C. M., Acosta, C. M., Costa, M. & Fazzio, A. From DFT to machine learning: recent approaches to materials science–a review. *J. Phys. Mater.* **2**, 032001 (2019).

18. Struble, T. J., Coley, C. W. & Jensen, K. F. Multitask Prediction of Site Selectivity in Aromatic C-H Functionalization Reactions. 28.

19. Li, H., Hui-Xia, F. & Meng, S. Silicene: from monolayer to multilayer — A concise review. *Chin. Phys. B* **24**, 086102 (2015).

20. Prarokijjak, W. & Soodchomshom, B. Large magnetoresistance dips and perfect spin-valley filter induced by topological phase transitions in silicene. *J. Magn. Magn. Mater.* **452**, 407–414 (2018).

21. Grazianetti, C. & Molle, A. Engineering Epitaxial Silicene on Functional Substrates for Nanotechnology. *Research* **2019**, 1–8 (2019).

22. Akbari, E. *et al.* Silicene and graphene nano materials in gas sensing mechanism. *RSC Adv.* **6**, 81647–81653 (2016).

23. Loh, T. A. J., Chua, D. H. C. & Wee, A. T. S. One-step Synthesis of Few-layer WS_2 by Pulsed Laser Deposition. *Sci. Rep.* **5**, 18116 (2016).

24. Ovchinnikov, D., Allain, A., Huang, Y.-S., Dumcenco, D. & Kis, A. Electrical Transport Properties of Single-Layer WS_2. *ACS Nano* **8**, 8174–8181 (2014).

25. Perrozzi, F. *et al.* Thermal stability of WS_2 flakes and gas sensing properties of WS_2/WO_3 composite to H_2, NH_3 and NO_2. *Sens. Actuators B Chem.* **243**, 812–822 (2017).

26. Das, S. & Appenzeller, J. WSe_2 field effect transistors with enhanced ambipolar characteristics. *Appl. Phys. Lett.* **103**, 103501 (2013).

27. Chu, C.-H. *et al.* End-Bonded Metal Contacts on WSe_2 Field-Effect Transistors. *ACS Nano* **13**, 8146–8154 (2019).

28. Fang, H. *et al.* High-Performance Single Layered WSe_2 p-FETs with Chemically Doped Contacts. *Nano Lett.* **12**, 3788–3792 (2012).

29. Ross, J. S. *et al.* Electrically tunable excitonic light-emitting diodes based on monolayer WSe_2 p–n junctions. *Nat. Nanotechnol.* **9**, 268–272 (2014).

30. Al Balushi, Z. Y. *et al.* Two-dimensional gallium nitride realized via graphene encapsulation. *Nat. Mater.* **15**, 1166–1171 (2016).

31. Wang, Q., Wu, P., Cao, G. & Huang, M. First-principles study of the structural and electronic properties of MoS_2–WS_2 and MoS_2–$MoTe_2$ monolayer heterostructures. *J. Phys. Appl. Phys.* **46**, 505308 (2013).

32. Choi, W. *et al.* Recent development of two-dimensional transition metal dichalcogenides and their applications. *Mater. Today* **20**, 116–130 (2017).

33. Dickinson, R. G. & Pauling, L. THE CRYSTAL STRUCTURE OF MOLYBDENITE. *J. Am. Chem. Soc.* **45**, 1466–1471 (1923).

34. Zheng, Y. J. *et al.* Point Defects and Localized Excitons in 2D WSe_2. *ACS Nano* **13**, 6050–6059 (2019).

35. Sarma, P. V., Tiwary, C. S., Radhakrishnan, S., Ajayan, P. M. & Shaijumon, M. M. Oxygen incorporated WS_2 nanoclusters with superior electrocatalytic properties for hydrogen evolution reaction. *Nanoscale* **10**, 9516–9524 (2018).

36. Bignardi, L. *et al.* Growth and Structure of Singly-Oriented Single-Layer Tungsten Disulfide on Au(111). *Phys. Rev. Mater.* **3**, 014003 (2019).

37. Yue, R. *et al.* Nucleation and growth of WSe_2 : enabling large grain transition metal dichalcogenides. *2D Mater.* **4**, 045019 (2017).

38. Castro Neto, A. H., Guinea, F., Peres, N. M. R., Novoselov, K. S. & Geim, A. K. The electronic properties of graphene. *Rev. Mod. Phys.* **81**, 109–162 (2009).

39. Andrei, E. Y., Li, G. & Du, X. Electronic properties of graphene: a perspective from scanning tunneling microscopy and magnetotransport. *Rep. Prog. Phys.* **75**, 056501 (2012).

40. Zhao, J. *et al.* Rise of silicene: A competitive 2D material. *Prog. Mater. Sci.* **83**, 24–151 (2016).

41. Rzeszotarski, B., Mreńca-Kolasińska, A. & Szafran, B. Electron interferometry and quantum spin Hall phase in silicene. *Phys. Rev. B* **99**, 165426 (2019).

42. Seyed-Talebi, S. M., Kazeminezhad, I. & Beheshtian, J. Theoretical prediction of silicene as a new candidate for the anode of lithium-ion batteries. *Phys. Chem. Chem. Phys.* **17**, 29689–29696 (2015).

43. Borisenko, V. E. *Semiconducting Silicides*. (Springer Berlin Heidelberg, 2000).

44. Yamazaki, T. *et al.* Mechanisms of Cr segregation to C11b/C40 lamellar interface in $(Mo,Nb)Si_2$ duplex silicide: A phase-field study to bridge experimental and first-principles investigations. *Intermetallics* **54**, 232–241 (2014).

45. Nonomura, T. *et al.* Thermoelectric properties of group VI metal silicide semiconductors. *Phys. Procedia* **11**, 110–113 (2011).

46. Simov, K. R., Nolph, C. A. & Reinke, P. Guided Self-Assembly of Mn Wires on the Si(100)(2 × 1) Surface. *J. Phys. Chem. C* **116**, 1670–1678 (2012).

47. Volders, C., Monazami, E., Ramalingam, G. & Reinke, P. Alternative Route to Silicene Synthesis via Surface Reconstruction on h-$MoSi_2$ Crystallites. *Nano Lett.* **17**, 299–307 (2017).

48. Philip Hofmann. Surface Physics. in (Philip Hofmann, 2016).

49. Basnet, G. Fabrication of Tungsten Tips Suitable for Scanning Probe Microscopy by Electrochemical Etching Methods. 63.

50. David Necas & Petr Klapetek. *Gwyddion: an open source software for SPM data analysis*.

51. Horcas, I. *et al.* WSXM: A software for scanning probe microscopy and a tool for nanotechnology. *Rev. Sci. Instrum.* **78**, 013705 (2007).

52. Hipps, K. W. *Handbook of Applied Solid State Spectroscopy*. (2005).

53. Limot, L., Maroutian, T., Johansson, P. & Berndt, R. Surface-State Stark Shift in a Scanning Tunneling Microscope. *Phys. Rev. Lett.* **91**, 196801 (2003).

54. Image Metrology. *SPIP*.

55. S. Hüfner. *Photoelectron Spectroscopy- Principles and Applications*. (Springer).

56. W. E. Spicer. Photoemissive, Photoconductive, and Optical Absorption Studies of Alkali Antimony Compounds. *Phys Rev* **112**, (1958).

57. S. Hofmann. *Auger- and X-Ray Photoelectron Spectroscopy in Materials Science*. (Springer).

58. S Doniach & M Sunjic. Many-electron singularity in X-ray photoemission and X-ray line spectra from metals. *J. Phys. C Solid State Phys.* **3**, (1970).

59. J. Libra. *KolXPD: Spectroscopy Data Measurement and Processing*. (2011).

60. Andrew Weber. Photoemission Spectroscopy Studies of New Topological Insulator Materials. (University of Missouri-Kansas City, 2015).

61. Liu, T. *et al.* Crested two-dimensional transistors. *Nat. Nanotechnol.* **14**, 223–226 (2019).

62. Yin, Z. *et al.* Single-Layer MoS_2 Phototransistors. *ACS Nano* **6**, 74–80 (2012).

63. Choudhury, T. H., Zhang, X., Balushi, Z. Y. A., Chubarov, M. & Redwing, J. M. Epitaxial Growth of 2D Layered Transition Metal Dichalcogenides. 36.

64. Chhowalla, M. *et al.* The chemistry of two-dimensional layered transition metal dichalcogenide nanosheets. *Nat. Chem.* **5**, 263–275 (2013).

65. Barrera, D. *et al.* Solution synthesis of few-layer 2H MX_2 (M = Mo, W; X = S, Se). *J. Mater. Chem. C* **5**, 2859–2864 (2017).

66. Li, H., Wu, J., Yin, Z. & Zhang, H. Preparation and Applications of Mechanically Exfoliated Single-Layer and Multilayer MoS_2 and WSe_2 Nanosheets. *Acc. Chem. Res.* **47**, 1067–1075 (2014).

67. Kim, J. H. *et al.* Centimeter-scale Green Integration of Layer-by-Layer 2D TMD vdW Heterostructures on Arbitrary Substrates by Water-Assisted Layer Transfer. *Sci. Rep.* **9**, 1641 (2019).

68. Tongay, S. *et al.* Tuning Interlayer Coupling in Large-Area Heterostructures with CVD-Grown MoS_2 and WS_2 Monolayers. *Nano Lett.* **14**, 3185–3190 (2014).

69. Iannaccone, G., Bonaccorso, F., Colombo, L. & Fiori, G. Quantum engineering of transistors based on 2D materials heterostructures. *Nat. Nanotechnol.* **13**, 183–191 (2018).

70. Zhang, Z. *et al.* Ultrafast Growth of Large Single Crystals of Monolayer WS_2 and WSe_2. *Natl. Sci. Rev.* (2020).

71. Electrical characterization of back-gated bi-layer MoS_2 field-effect transistors and the effect of ambient on their performances. *Appl. Phys. Lett.* **100**, 123104 (2012).

72. Kim, J. H. *et al.* Work function variation of MoS_2 atomic layers grown with chemical vapor deposition: The effects of thickness and the adsorption of water/oxygen molecules. *Appl. Phys. Lett.* **106**, 251606 (2015).

73. Mirabelli, G. *et al.* Effects of Annealing Temperature and Ambient on Metal/$PtSe_2$ Contact Alloy Formation. *ACS Omega* **4**, 17487–17493 (2019).

74. Donarelli, M., Bisti, F., Perrozzi, F. & Ottaviano, L. Tunable sulfur desorption in exfoliated MoS_2 by means of thermal annealing in ultra-high vacuum. *Chem. Phys. Lett.* **588**, 198–202 (2013).

75. Zhu, C. (Rose), Gao, D., Ding, J., Chao, D. & Wang, J. TMD-based highly efficient electrocatalysts developed by combined computational and experimental approaches. *Chem. Soc. Rev.* **47**, 4332–4356 (2018).

76. J. H. Scofield. Hartree-Slater Subshell Photoionization Cross-sections at 1254 and 1487 eV. *J. Electron Spectrosc. Relat. Phenom.* **8**, 129–137 (1976).

77. D. A. Shirley. High-Resolution X-Ray Photoemission Spectrum of the Valence Bands of Gold. *Phys. Rev. B* **5**, (1972).

78. Fleisch, T. H. & Mains, G. J. An XPS study of the UV reduction and photochromism of MoO_3 and WO_3. *J. Chem. Phys.* **76**, 780–786 (1982).

79. Gassman, P. G., Macomber, D. W. & Willging, S. M. Isolation and characterization of reactive intermediates and active catalysts in homogeneous catalysis. *J. Am. Chem. Soc.* **107**, 2380–2388 (1985).

80. Morgan, D. J. Core-level spectra of powdered tungsten disulfide, WS_2. *Surf. Sci. Spectra* **25**, 014002 (2018).

81. Ng, K. T. & Hercules, D. M. Studies of nickel-tungsten-alumina catalysts by x-ray photoelectron spectroscopy. *J. Phys. Chem.* **80**, 2094–2102 (1976).

82. Biener, M. M., Biener, J. & Friend, C. M. Novel synthesis of two-dimensional TiS_2 nanocrystallites on Au(111). *J. Chem. Phys.* **122**, 034706 (2005).

83. Murray, J. L. The Au-Ti (Gold-Titanium) system. *Bull. Alloy Phase Diagr.* **4**, 278–283 (1983).

84. Bzowski, A. & Sham, T. K. Electronic structure of Au–Ti intermetallics. *J. Vac. Sci. Technol. Vac. Surf. Films* **11**, 2153–2157 (1993).

85. Reinke, P., Francz, G., Oelhafen, P. & Ullmann, J. Structural changes in diamond and amorphous carbon induced by low-energy ion irradiation. *Phys. Rev. B* **54**, 7067–7073 (1996).

86. Reinke, P. & Oelhafen, P. Thermally induced structural changes in amorphous carbon films observed with ultraviolet photoelectron spectroscopy. *J. Appl. Phys.* **81**, 2396–2399 (1997).

87. Kazansky, L. P. & Launay, J. P. X-ray photoelectron study of mixed valence metatungstate anions. *Chem. Phys. Lett.* **51**, 242–245 (1977).

88. McGuire, G. E., Schweitzer, G. K. & Carlson, T. A. Core electron binding energies in some Group IIIA, VB, and VIB compounds. *Inorg. Chem.* **12**, 2450–2453 (1973).

89. Hashimoto, S. & Tanaka, A. Alteration of Ti 2p XPS spectrum for titanium oxide by low-energy Ar ion bombardment. *Surf. Interface Anal.* **34**, 262–265 (2002).

90. Shelton, C. T. *et al.* Chemically Homogeneous Complex Oxide Thin Films Via Improved Substrate Metallization. *Adv. Funct. Mater.* **22**, 2295–2302 (2012).

91. Ihlefeld, J. F. *et al.* Solution Chemistry, Substrate, and Processing Effects on Chemical Homogeneity in Lead Zirconate Titanate Thin Films. *J. Am. Ceram. Soc.* **98**, 2028–2038 (2015).

92. Park, J. H *et al.* Scanning Tunneling Microscopy and Spectroscopy of Air Exposure Effects on Molecular Beam Epitaxy Grown WSe_2 Monolayers and Bilayers. *ACS Nano* **10**, 4258–4267 (2016).

93. Fuhrer, M. S. & Hone, J. Measurement of mobility in dual-gated MoS_2 transistors. *Nat. Nanotechnol.* **8**, 146 (2013).

94. Ponomarev, E., Gutierrez-Lezama, I., Ubrig, N. & Morpurgo, A. F. Ambipolar Light-Emitting Transistors on Chemical Vapor Deposited Monolayer MoS_2. *Nano Lett.* **15**, 8289--8294 (2015).

95. Radisavljevic, B., Radenovic, A., Brivio, J., Giacometti, i V. & Kis, A. Single-layer MoS_2 transistors. *Nat. Nanotechnol.* **6**, 147 (2011).

96. Wu, D. *et al.* High mobility top gated field-effect transistors and integrated circuits based on chemical vapor deposition-derived monolayer MoS_2. *Mater. Express* **6**, 198--204 (2016).

97. Briggs, N. *et al.* A roadmap for electronic grade 2D materials. *2D Mater.* **6**, 022001 (2019).

98. Wang, S., Wang, X. & Warner, J. H. All Chemical Vapor Deposition Growth of MoS_2 :h-BN Vertical van der Waals Heterostructures. *ACS Nano* **9**, 5246--5254 (2015).

99. Cho, B. *et al.* Bifunctional sensing characteristics of chemical vapor deposition synthesized atomic-layered MoS_2. *ACS Appl. Mater. Interfaces* **7**, 2952--2959 (2015).

100. Liu, X., Balla, I., Bergeron, H. & Hersam, M. C. Point Defects and Grain Boundaries in Rotationally Commensurate MoS_2 on Epitaxial Graphene. *J. Phys. Chem. C* **120**, 20798--20805 (2016).

101. Zhang, Y. *et al.* Dendritic, transferable, strictly monolayer MoS_2 flakes synthesized on $SrTiO_3$ single crystals for efficient electrocatalytic applications. *ACS Nano* **8**, 8617--8624 (2014).

102. Zhu, Y. *et al.* Strongly enhanced photoluminescence in nanostructured monolayer MoS_2 by chemical vapor deposition. *Nanotechnology* **27**, (2016).

103. Wang, S., Pacios, M., Bhaskaran, H. & Warner, J. H. Substrate control for large area continuous films of monolayer MoS_2 by atmospheric pressure chemical vapor deposition. *Nanotechnology* **27**, 085604 (2016).

104. Wang, S. *et al.* Shape Evolution of Monolayer MoS_2 Crystals Grown by Chemical Vapor Deposition. *Chem. Mater.* **26**, 6371--6379 (2014).

105. Ling, X. *et al.* Role of the Seeding Promoter in MoS_2 Growth by Chemical Vapor Deposition. *Nano Lett.* **14**, 464--472 (2014).

106. Hussain, S. *et al.* Controlled synthesis and optical properties of polycrystalline molybdenum disulfide atomic layers grown by chemical vapor deposition. *J. Alloys Compd.* **653**, 369--378 (2015).

107. Kosku Perkgoz, N. CVD Growth and Characterization of 2D Transition Metal Dichalcogenides, MoS_2 and WS_2. *Anadolu Univ. J Sci. Technol. - Appl. Sci. Eng.* **1**, 18 (2017).

108. Wu, D. *et al.* E’’ Raman Mode in Thermal Strain-Fractured CVD-MoS_2. *Crystals* **6**, 151 (2016).

109. Xu, T. *et al.* High-response NO_2 resistive gas sensor based on bilayer MoS_2 grown by a new two-step chemical vapor deposition method. *J. Alloys Compd.* **725**, 253--259 (2017).

110. Jeon, I. *et al.* Multilayered MoS_2 nanoflakes bound to carbon nanotubes as electron acceptors in bulk heterojunction inverted organic solar cells. *Org. Electron. Phys. Mater. Appl.* **17**, 275--280 (2015).

111. Mahyavanshi, R. D. *et al.* Synthesis of MoS_2 ribbons and their branched structures by chemical vapor deposition in sulfur-enriched environment. *Appl. Surf. Sci.* **409**, 396--402 (2017).

112. Jiang, Z. *et al.* Ultrathin quartz plate-based multilayer MoS_2 for passively mode-locked fiber lasers (invited). *Opt. Commun.* **406**, 44--49 (2018).

113. Cho, B. *et al.* Charge-transfer-based gas sensing using atomic-layer MoS_2. *Sci. Rep.* **5**, 8052 (2015).

114. Kim, H., Dumcenco, D. & Fr, M. Free-standing electronic character of monolayer MoS_2 in van der Waals epitaxy. *Phys. Rev. B* **94**, 081401(R) (2016).

115. Lee, Y.-H. *et al.* Synthesis of Large-Area MoS_2 Atomic Layers with Chemical Vapor Deposition. *Adv. Mater.* **24**, 2320--2325 (2012).

116. Liu, H. *et al.* Role of the carrier gas flow rate in monolayer MoS_2 growth by modified chemical vapor deposition. *Nano Res.* **10**, 643--651 (2017).

117. Sharma, D. K. *et al.* Pressure-dependent large area synthesis and electronic structure of MoS_2. *Mater. Res. Bull.* **97**, 265--271 (2018).

118. Zhan, Y., Liu, Z., Najmaei, S., Ajayan, P. M. & Lou, J. Large-Area Vapor-Phase Growth and Characterization of MoS_2 Atomic Layers on a SiO_2 Substrate. *Small* **8**, 966--971 (2012).

119. Zhou, D. *et al.* Unveiling the Growth Mechanism of MoS_2 with Chemical Vapor Deposition: From Two-Dimensional Planar Nucleation to Self-Seeding Nucleation. *Cryst. Growth Des.* **18**, 1012--1019 (2018).

120. Ji, Q. *et al.* Epitaxial monolayer MoS_2 on mica with novel photoluminescence. *Nano Lett.* **13**, 3870--3877 (2013).

121. Shi, J. *et al.* Controllable growth and transfer of monolayer MoS_2 on Au foils and its potential application in hydrogen evolution reaction. *ACS Nano* **8**, 10196--10204 (2014).

122. Behura, S., Nguyen, P., Che, S., Debbarma, R. & Berry, V. Large-Area, Transfer-Free, Oxide-Assisted Synthesis of Hexagonal Boron Nitride Films and Their Heterostructures with MoS_2 and WS_2. *J. Am. Chem. Soc.* **137**, 13060--13065 (2015).

123. Ji, Q. *et al.* Unravelling orientation distribution and merging behavior of monolayer MoS_2 domains on sapphire. *Nano Lett.* **15**, 198--205 (2015).

124. Chen, W. *et al.* Oxygen-Assisted Chemical Vapor Deposition Growth of Large Single-Crystal and High-Quality Monolayer MoS_2. *J. Am. Chem. Soc.* **137**, 15632--15635 (2015).

125. Shi, J. *et al.* Substrate facet effect on the growth of monolayer MoS_2 on Au foils. *ACS Nano* **9**, 4017--4025 (2015).

126. Chakraborty, B., Matte, H. R., Sood, A. & Rao, C. Layer-dependent resonant Raman scattering of a few layer MoS_2. *J. Raman Spectrosc.* **44**, 92–96 (2013).

127. Wang, Y., Cong, C., Qiu, C. & Yu, T. Raman Spectroscopy Study of Lattice Vibration and Crystallographic Orientation of Monolayer MoS_2 under Uniaxial Strain. *Small* **9**, 2857–2861 (2013).

128. Park, W. *et al.* Photoelectron Spectroscopic Imaging and Device Applications of Large-Area Patternable Single-Layer MoS_2 Synthesized by Chemical Vapor Deposition. *ACS Nano* **8**, 4961--4968 (2014).

129. Bogaert, K., Liu, S., Chesin, J., Titow, D. & Gradec, S. Diffusion-Mediated Synthesis of MoS_2/WS_2 Lateral Heterostructures. *Nano Lett.* **16**, 5129--5134 (2016).

130. Fu, L. *et al.* Direct Growth of MoS_2/h-BN Heterostructures via a Sulfide-Resistant Alloy. *ACS Nano* **10**, 2063--2070 (2016).

131. Lin, Y.-C. *et al.* Direct Synthesis of van der Waals Solids. *ACS Nano* **8**, 3715–3723 (2014).

132. Cattelan, M. *et al.* New Strategy for the Growth of Complex Heterostructures Based on Different 2D Materials. *Chem. Mater.* **27**, 4105–4113 (2015).

133. Zhang, D. *et al.* Highly efficient microwave absorption properties and broadened absorption bandwidth of MoS_2-iron oxide hybrids and MoS_2-based reduced graphene oxide hybrids with Hetero-structures. *Appl. Surf. Sci.* **462**, 872–882 (2018).

134. Novoselov, K. S., Andreeva, D. V., Ren, W. & Shan, G. Graphene and other two-dimensional materials. *Front. Phys.* **14**, 13301 (2019).

135. Deshpande, A., Bao, W., Zhao, Z., Lau, C. N. & LeRoy, B. J. Imaging charge density fluctuations in graphene using Coulomb blockade spectroscopy. *Phys Rev B* **83**, 155409 (2011).

136. Zhang, Y., Brar, V. W., Girit, C., Zettl, A. & Crommie, M. F. Origin of spatial charge inhomogeneity in graphene. *Nat. Phys.* 722.

137. Li, G. *et al.* Observation of Van Hove singularities in twisted graphene layers. *Nat. Phys.* 109.

138. Carr, S. *et al.* Twistronics: Manipulating the electronic properties of two-dimensional layered structures through their twist angle. *Phys Rev B* **95**, 075420 (2017).

139. Govind Rajan, A., Warner, J. H., Blankschtein, D. & Strano, M. S. Generalized Mechanistic Model for the Chemical Vapor Deposition of 2D Transition Metal Dichalcogenide Monolayers. *ACS Nano* **10**, 4330–4344 (2016).

140. Kranthi Kumar, V., Dhar, S., Choudhury, T. H., Shivashankar, S. A. & Raghavan, S. A predictive approach to CVD of crystalline layers of TMDs: the case of MoS_2. *Nanoscale* **7**, 7802–7810 (2015).

141. Xuan, Y. *et al.* Multi-scale modeling of gas-phase reactions in metal-organic chemical vapor deposition growth of WSe_2. *J. Cryst. Growth* **527**, 125247 (2019).

142. Mostavi, M., Salekin, S. & Huang, Y. Deep-2'-O-Me: Predicting 2'-O-methylation sites by Convolutional Neural Networks. *Conf Proc IEEE Eng Med Biol Soc*, 2394–2397 (2018).

143. Lookman, T., Balachandran, P. V., Xue, D. & Yuan, R. Active learning in materials science with emphasis on adaptive sampling using uncertainties for targeted design. *Npj Comput. Mater.* **5**, 21 (2019).

144. Hanakata, P. Z., Cubuk, E. D., Campbell, D. K. & Park, H. S. Accelerated Search and Design of Stretchable Graphene Kirigami Using Machine Learning. *Phys Rev Lett* **121**, 255304 (2018).

145. Mostavi, M., Chiu, Y.-C., Huang, Y. & Chen, Y. Convolutional neural network models for cancer type prediction based on gene expression. *ArXiv E-Prints* (2019).

146. Holleis, L., Shivaram, B. S. & Balachandran, P. V. Machine learning guided design of single-molecule magnets for magnetocaloric applications. *Appl. Phys. Lett.* **114**, 222404 (2019).

147. Butler, K. T., Davies, D. W., Cartwright, H., Isayev, O. & Walsh, A. Machine learning for molecular and materials science. *Nature* **559**, 547--555 (2018).

148. Schmidt, J., Marques, M. R. G., Botti, S. & Marques, M. A. L. Recent advances and applications of machine learning in solid-state materials science. *Npj Comput. Mater.* **5**, 83 (2019).

149. Tawfik, S. A. *et al.* Efficient Prediction of Structural and Electronic Properties of Hybrid 2D Materials Using Complementary DFT and Machine Learning Approaches. *Adv. Theory Simul.* **2**, 1800128 (2019).

150. Frey, N. C. *et al.* Prediction of Synthesis of 2D Metal Carbides and Nitrides (MXenes) and Their Precursors with Positive and Unlabeled Machine Learning. *ACS Nano* **13**, 3031--3041 (2019).

151. Wissmann, P. J. & Grover, M. A. Optimization of a Chemical Vapor Deposition Process Using Sequential Experimental Design. *Ind. Eng. Chem. Res.* **49**, 5694–5701 (2010).

152. Young, S. R. *et al.* Data mining for better material synthesis: The case of pulsed laser deposition of complex oxides. *J. Appl. Phys.* **123**, 115303 (2018).

153. Tang, B. *et al.* Machine learning-guided synthesis of advanced inorganic materials. *ArXiv E-Prints* (2019).

154. Wakabayashi, Y. K. *et al.* Machine-learning-assisted thin-film growth: Bayesian optimization in molecular beam epitaxy of SrRuO$_3$ thin films. *ArXiv E-Prints* (2019).

155. Lauritsen, J. V. *et al.* Chemistry of one-dimensional metallic edge states in MoS_2 nanoclusters. *Nanotechnology* **14**, 385--389 (2003).

156. Tshitoyan, V. *et al.* Unsupervised word embeddings capture latent knowledge from materials science literature. *Nature* **571**, 95--98 (2019).

157. Krzywinski, M. & Altman, N. Visualizing samples with box plots. *Nat. Methods* **11**, 119 (2014).

158. Rickman, J. M. Data analytics and parallel-coordinate materials property charts. *Npj Comput. Mater.* **4**, 5 (2018).

159. Kruskal, J. B. Multidimensional scaling by optimizing goodness of fit to a nonmetric hypothesis. *Psychometrika* **29**, 1--27 (1964).

160. Benesty, J., Chen, J., Huang, Y. & Cohen, I. Pearson Correlation Coefficient. in *Noise Reduction in Speech Processing* 1--4 (Springer Berlin Heidelberg, 2009).

161. Breiman, L. Random Forests. *Mach. Learn.* **45**, 5--32 (2001).

162. Liaw, A. & Wiener, M. Classification and Regression by randomForest. *R News* **2**, 18–22 (2002).

163. R Core Team. R: A Language and Environment for Statistical Computing. (2012).

164. MacKinnon, D. P., Lockwood, C. M. & Williams, J. Confidence Limits for the Indirect Effect: Distribution of the Product and Resampling Methods. *Multivar. Behav. Res.* **39**, 99--128 (2004).

165. Blumer, A., Ehrenfeucht, A., Haussler, D. & Warmuth, M. K. Occam's Razor. *Inf. Process. Lett.* **24**, 377--380 (1987).

166. Kursa, M. B. & Rudnicki, W. R. Feature Selection with the Boruta Package. *J. Stat. Softw.* **36**, 1--13 (2010).

167. Najmaei, S. *et al.* Vapour phase growth and grain boundary structure of molybdenum disulphide atomic layers. *Nat. Mater.* **12**, 754--759 (2013).

168. Tahir, M. & Schwingenschlögl, U. Magnetocapacitance of an electrically tunable silicene device. *Appl. Phys. Lett.* **101**, 132412 (2012).

169. Lian, C. & Meng, S. Dirac cone pairs in silicene induced by interface Si-Ag hybridization: A first-principles effective band study. *Phys. Rev. B* **95**, 245409 (2017).

170. Szafran, B., Mreńca-Kolasińska, A., Rzeszotarski, B. & Żebrowski, D. Electrical control of a confined electron spin in a silicene quantum dot. *Phys. Rev. B* **97**, 165303 (2018).

171. Fleurence, A. *et al.* Experimental Evidence for Epitaxial Silicene on Diboride Thin Films. *Phys. Rev. Lett.* **108**, 245501 (2012).

172. Mahatha, S. K. *et al.* Absence of Dirac cones in monolayer silicene and multilayer Si films on Ag(111). *J. Electron Spectrosc. Relat. Phenom.* **219**, 2–8 (2017).

173. Kukucska, G., Zólyomi, V. & Koltai, J. Characterization of epitaxial silicene with Raman spectroscopy. *Phys. Rev. B* **98**, 075437 (2018).

174. Nicholls, D., Fatima, Çakır, D. & Oncel, N. Silicene-Like Domains on $IrSi_3$ Crystallites. *J. Phys. Chem. C* **123**, 7225–7229 (2019).

175. Meng, L. *et al.* Buckled Silicene Formation on Ir(111). *Nano Lett.* **13**, 685–690 (2013).

176. Peters, J. L. *et al.* Mono- and Multilayer Silicene-Type Honeycomb Lattices by Oriented Attachment of PbSe Nanocrystals: Synthesis, Structural Characterization, and Analysis of the Disorder. *Chem. Mater.* **30**, 4831–4837 (2018).

177. Scalise, E., Iordanidou, K., Afanas'ev, V. V., Stesmans, A. & Houssa, M. Silicene on non-metallic substrates: Recent theoretical and experimental advances. *Nano Res.* **11**, 1169–1182 (2018).

178. Lee, G. *et al.* Structure of the Ba-Induced Si (111) - (3 × 2) Reconstruction. *Phys. Rev. Lett.* **87**, 056104 (2001).

179. Song, S. K., Kim, T.-H. & Yeom, H. W. Atomic structures of self-assembled epitaxially grown $GdSi_2$ nanowires on Si(001) by STM. *Sci. Rep.* **9**, 1364 (2019).

180. C. K. Gupta. *Extractive Metallurgy of Molybdenum*. (Routledge, 2017).

181. Hiraoka, R. *et al.* Transport characteristics of a silicene nanoribbon on Ag(110). *Beilstein J. Nanotechnol.* **8**, 1699–1704 (2017).

182. Wolkow, R. A. Direct observation of an increase in buckled dimers on Si(001) at low temperature. *Phys. Rev. Lett.* **68**, 2636–2639 (1992).

183. Hasegawa, Y. *et al.* Adsorption of Li (K) on the Si(001)-(2×1) surface: Scanning-tunneling-microscopy study. *Phys. Rev. B* **41**, 9688–9691 (1990).

184. Roge, T. P. *et al.* Surface reconstruction of $ErSi_{1.7}$ (0001) investigated by scanning tunneling microscopy. *Phys. Rev. B* **51**, 10998–11001 (1995).

185. Lin, W. T. & Chen, L. J. Localized epitaxial growth of hexagonal and tetragonal $MoSi_2$ on (111) Si. *Appl. Phys. Lett.* **46**, 1061–1063 (1985).

186. Ohishi, Y. *et al.* Synthesis of silicon and molybdenum–silicide nanocrystal composite films having low thermal conductivity. *Thin Solid Films* **534**, 238–241 (2013).

187. Ding, T. *et al.* Crystalline structures and misfit strain inside Er silicide nanocrystals self-assembled on Si(001) substrates. *Nanotechnology* **22**, 245707 (2011).

188. Liu, Z.-L. *et al.* Various atomic structures of monolayer silicene fabricated on Ag(111). *New J. Phys.* **16**, 075006 (2014).

189. W. H. Blades, N. J. Frady, P. M. Litwin, S. J. McDonnell & P. Reinke. Thermally Induced Defects on WSe_2. *J Phys Chem C* **124**, 15337–15346 (2020).